IN-02
83777
P 126

NASA Contractor Report 189586

HEAT TRANSFER CHARACTERISTICS OF HYPERSONIC WAVERIDERS WITH AN EMPHASIS ON THE LEADING EDGE EFFECTS

Denis O. Vanmol and John D. Anderson, Jr.

UNIVERSITY OF MARYLAND
College Park, Maryland

Grant NAG1-1192
March 1992

National Aeronautics and Space Administration

Langley Research Center
Hampton, Virginia 23665-5225

Abstract

Title of Thesis: Heat Transfer Characteristics of Hypersonic Waveriders with an Emphasis on the Leading Edge Effects

Name of Degree Candidate: Denis O. Vanmol

Degree and Year: Master of Science, 1991

Thesis Directed by: Dr. John D. Anderson, Jr.
Professor
Department of Aerospace Engineering

The heat transfer characteristics in surface radiative equilibrium and the aerodynamic performance of blunted hypersonic waveriders are studied along two constant dynamic pressure trajectories for four different Mach numbers.

In terms of performance, the inviscid leading edge drag was found to be a small (4 to 8%) but non-negligible fraction of the inviscid drag of the vehicle. Although the viscous drag at the leading edge can be neglected, the presence of the leading edge will influence the transition pattern of the upper and lower surfaces and therefore affect the viscous drag of the entire vehicle.

Finally, for an application similar to the NASP, the present study demonstrates that the waverider remains a valuable concept at high Mach number if a state-of-the-art active cooling device is used along the leading edge. At low Mach number (≤ 5), the study shows that surface radiative cooling might be sufficient. In all cases, radiative cooling is sufficient for the upper and lower surfaces of the vehicle if ceramic composites is used as thermal protection.

Acknowledgments

My deepest gratitude goes out to my advisor, Dr. John D. Anderson for his continuing support throughout this project. I have deeply appreciated his kindness, his modesty and enjoyed his classes as wonderful fairy tales about science. I would also like to thank Dr. Lewis for his advice and accepting me in his student group for fruitful discussions. I also thank Dr. Jones for providing me interesting paper about transition.

My fellow students made the long hours in the computer room more enjoyable . Thanks to all of them for their support and their friendship. A special thank goes out to Naru for his patience solving my computer problems, Mary Kae for her advice on waverider, Yvette for teaching me "Publisher", Charles for correcting my grammar and Ashish for improving my English .....

I would also like to thank Dr. John F. Wendt, director at the "Von Karman Institute for Fluid Dynamics" for introducing me to Dr. Anderson and helping me to get accepted for this Masters program.

Finally, I would like to apologize to my wife and my daughter for all the time I spend with the computer instead of taking care of them.

Table of Contents

List of Tables

List of Figures

List of Symbols

English Symbols

a_i''	Axial force per unit span
C	Degree centigrade
$C(\zeta)$	Carving function
c_{a_i}''	Axial force coefficient per unit span
C_{max}	Maximum cross flow velocity
Cp	Pressure coefficient
Cp_a	Pressure coefficient at the attachment line
Cpt	Total pressure coefficient
Cx	Center of Radius R_x
C_D	Drag coefficient
C_L	Lift coefficient
d	Trip wire diameter
πd^2	Collision cross section
d_i''	Drag force per unit span
D	Cylinder diameter
h_{aw}	Adiabatic wall enthalpy
h_w	Wall enthalpy
H_0	Total enthalpy
H_{11}	Streamwise shape factor
k	Boltzmann constant
K	Degree Kelvin
Kn	Knudsen number

L	Lift force; waverider length
L/D	Lift over drag ratio
M	Mach number
MW/m^2	megawatts per square meter
n	Number density
p	Pressure
q	Dynamic pressure
$\dot{q}_w$	Heat transfer at the wall
R	Nose or leading edge radius
R_{gas}	Universal gas constant for air
Re_s	Reynolds number based on distance
R	Critical Reynolds number along the attachment line
s	Distance along the streamline
S_{plan}	Planform surface
T	Temperature
V	Velocity
V_{eff}	Volume efficiency
x	x-coordinate in Cartesian system
X	Critical cross flow Reynolds number
y	y-coordinate in Cartesian system
z	z-coordinate in Cartesian system
$Z_{0.01Cmax}$	Point where C_{max} has dropped to 0.1% of its value

Greek Symbols

α	Angle of incidence
γ	Ratio of specific heats
Γ	Intermittency function
δ	Relative angle of the body to the free stream
ϵ	Emissivity; disturbance propagation angle
ζ	Ratio of L(y)/L
η	Boundary layer characteristic length
θ	Streamline local inclination
λ	Mean free path
Λ	Sweep angle
μ	Dynamic viscosity
ν	Cinematic viscosity
ρ	Density
σ	Stefan-Boltzmann constant
τ	Polar angle

Subscripts

axi	Axisymmetric
convect	Convective
cyl	Cylinder
e	At the edge of the boundary layer
eq	In radiative equilibrium
fp	Flat plate
le	Leading edge
n	Normal to the cylinder
r	At recovery conditions
rad	Radiative
w	At the wall
02	Behind a normal shock
∞	Freestream quantity
*	At reference temperature

Chapter 1 INTRODUCTION

In 1989, a panel of experts in hypersonic technology published a report[1] defining the most critical technologies of hypersonic flight for an application such as the NASP. They judged these to be :

- the supersonic combustion ramjet engine
- the technology of integrating such engine with the airframe
- the structural concepts and high temperature low density materials required to achieve the desired weight fractions
- guidance and control of such large, flexible, complex vehicle

The present research, focused on the heat transfer evaluation of an hypersonic waverider aiming at the same mission as the NASP, is directly related to the third technological key through the definition of the thermal protection of the vehicle.

Previous studies at University of Maryland[2,3,4] have already demonstrated that viscous-optimized waveriders can be designed with lift-to-drag ratios higher than other conventional hypersonic configurations. Moreover, the waverider generates a relatively uniform flow on the lower surface making this concept very suitable from the engine integration point of view[5]. In another study[6] conducted at University of Maryland, results indicate that the point-design waveriders do not suffer any marked off-design problems; they indeed behave much like delta wings in such a cases.

For all these reasons, the waverider concept is moving from an academic concept to a very practical one for consideration as hypersonic cruiser, hypersonic accelerator or aero-assisted vehicle for space mission.

The present work is part of the continuing study of waveriders in the Hypersonic group at the University of Maryland. This study takes another logical step and

examines the problem of aerodynamic heating for this class of vehicles with an emphasis on the leading edge.

Section 1 Purpose of study

The purpose of this study is to demonstrate that the waverider concept remains a valuable option when the problem of aerodynamic heating is taken into account. This problem is probably more critical at the leading edge of a waverider than for any other vehicle.

The leading edge of the waverider being in theory infinitely sharp, it will lead to an infinite value of the temperature. There is thus an absolute need for blunting the leading edge in order to decrease the temperature. But, due to the small waverider thickness near the leading edge, the accommodation of a finite radius also means that the planform shape will have to be modified. In this case, if the planform shape is too strongly affected, the flow on the lower surface will loose its original nature and the performance of the waverider will be degraded. The name of the game is thus to implement, according to a given waverider geometry, a radius distribution all along the leading edge which is such that we will not exceed the maximum temperature allowed for a given material.

When dealing with a finite value of the radius along the leading edge, another major phenomena has to be taken into account : the transition along the attachment line of the leading edge. This phenomenon, is relevant not only along the attachment line in the spanwise direction , but it also has an impact on the transition pattern in the streamwise direction.

Finally, we will demonstrate that the waverider remains a valuable concept if a state of the art active cooling device is used at the leading edge.

In order to achieve this work, a computer code originally written by McLaughlin[4] was extensively modified. The heat transfer characteristics for surface radiative

equilibrium, as well as the aerodynamic performance of waveriders with blunted leading edges, are studied along two constant dynamic pressure trajectories for four different Mach numbers.

Chapter 2 WAVERIDER CONSTRUCTION

The computer code originally written by McLaughlin was modified to implement the leading edge radius distribution and the heat transfer evaluation on the vehicle. Since this study does not require the modification of the procedure used to generate viscous optimized waveriders, we will extensively refer, for this part, to the original work of McLaughlin[4].

To generate a waverider, two basic functions must be performed. First, the flowfield around a generating body (cone here) is calculated. Second, when the generating flowfield is known, the stream function must be evaluated in order to define the flow streamlines. Once these are known, it is possible to carve any number of different waveriders from a single generating flowfield.

Section 1 Generating flowfield solutions

Calorically perfect case

The conical flowfield solution for the calorically perfect gas is generated using a standard Taylor-Maccoll formulation[7]. An ordinary differential equation is solved numerically for a specific cone angle using an inverse approach where the shock angle is guessed and the cone angle that supports the shock is calculated.

For a given shock angle, we can calculate the conditions immediately behind the shock. These conditions are used as initial values and the Taylor-Maccoll equation is integrated using a fourth order Runge-Kutta method from the shock to the body. Once the proper solution is achieved, all the flow properties such as pressure, temperature, velocity can be defined.

Chemical equilibrium case

The same inverse approach is used to generate the chemically reacting conical flowfield[8]. In this case a set of three coupled differential equations combined with equilibrium high-temperature properties of air[9] is integrated using the same fourth order Runge-Kutta method. This system of equations is a chemical equilibrium analogous to the calorically perfect Taylor-Maccoll equation for conical flow at zero angle of attack.

Section 2 Generation of waverider geometry

The waverider geometry can be entirely defined when its planform shape, coincident with the shock, is known. From each point defining the planform shape , a streamline can be traced through the conical generating flowfield and the resulting stream surface becomes the lower surface of the waverider. From the same points, freestream streamlines can be created and will determine the upper surface (fig.1).

Note that since the upper surface of the waverider is a freestream stream surface, the flowfield depicted above this surface, and the generating cone, do not exist when the waverider is actually in flight. The entire flowfield above the upper surface is strictly used in the design of the vehicle, and only the flowfield below the waveriders lower surface actually exists at flight conditions.

Due to the waverider symmetry, only half of the planform shape needs to be defined. Each planform shape is defined by the projection, on the generating conical shock, of a curve passing through five points in the x-y plane (fig.2).

By symmetry, one point is forced to lie on the y-axis. Another one is forced to lie on the conical shock. These five points represent in fact eight degrees of freedom (10 coordinates — 2 constraints) which will be used by the optimization procedure[10]

to determine the best geometry associated with a given figure of merit (maximum L/D, maximum volume, ...).

Section 3 Definition of the leading edge geometry

Up to here, the generated waverider has still an infinitely sharp leading edge. Since the waverider geometry of the upper and lower surfaces are now known we can define a process to accommodate some bluntness to the leading edge. Let's consider a side cross section of our waverider (fig.3) at a given spanwise (Y=constant) station. The flow is coming from left to right. Moving in the Z direction from the original leading edge point to the trailing edge, we can define a radius R at any Z station in function of the local waverider thickness and the local relative angle of attack (δ) of the lower surface. The waverider length, in a Y=constant plane is defined as L(Y) and represents the distance from the original leading edge point to the trailing edge. In the symmetry plane, L(Y) equals the imposed waverider length and L(Y)=0 at the wing tip. Thus, L(Y) varies in between these two limits according to the vehicle planform shape.

The planform shape of a half waverider being defined by 51 points, we are now able to associate to each of these points a finite radius if we specify a certain amount of carving. The carving distance is measured from the original leading edge point to the point where the waverider thickness is evaluated. This distance, C*L(Y), can be expressed in terms of a carving coefficient C held constant or varying with L(Y). The most satisfying results were obtained with a carving coefficient varying with the ratio L(Y)/L. The function used is of the type :

$$C(\zeta) = \frac{a}{\zeta^m + b} \quad , with \quad \zeta = \frac{L(Y)}{L} \tag{1}$$

where a, b, m are positive coefficients adjusted to obtain a reasonable variation of $C(\zeta)$. For all the cases presented later, m was set to 0.9 and the value of a, b were calculated in such a way that C(0)=50% and C(1)=2%. This increasing carving coefficient, from the centerline to the wing tip, combined with decreasing values of L(Y) produces a slowly decreasing carving distance which preserves relatively well the planform shape (fig.4). A typical radius distribution is presented in figure 5 and shows a slowly decaying radius distribution except near the wing tip where it decreases rapidly. Since L(Y) and the waverider thickness are equal to zero at the wing tip, the radius at that particular point is arbitrarily set to the value of the previous one. Since the radius distribution is not guaranteed to be a monotonically decreasing function we will enforce it. This is done by simply imposing that the value of R(Y) is always greater or equal than the value of $R(Y+\Delta Y)$. Therefore, the carving distance previously defined can be seen for all cases as the maximum modification performed on the planform shape.

Once the radius distribution is defined, we can also calculate the sweep angle distribution along the planform shape (fig.6). Note that when the sweep angle distribution is calculated on the original planform shape, the differences between the two distributions are marginal. The sweep angle at the nose is set to zero and the sweep angle of the last point (wing tip) is set to the value of the previous point.

Section 4 Definition of the nose geometry

As we have defined our leading edge up to now, the nose would be represented by the intersection of two swept cylinders. This configuration, obviously not realistic from a heat transfer point of view, was modified by assuming that an arc of circle (radius R_x, center C_x) joined the stagnation point and the second point of the planform. This assumption leads us to consider the nose region as a 3D stagnation point defined by the two radii R_x and R_y (fig.7).

Therefore, we will always assume that the nose region will be situated between the two first points of the planform shape. The leading edge region starts at the second point and extends up to the wing tip.

Chapter 3 AERODYNAMIC ANALYSIS OF A WAVERIDER

The aerodynamic analysis of a waverider requires both an inviscid and viscous analysis on the vehicle.

For the inviscid part, the analysis is relatively straightforward since it only requires the integration of the pressure forces. The inviscid aerodynamic analysis of a waverider configuration involves the calculation of both the lift and drag forces due to the pressure on the surfaces of the body. Since this part has already been extensively explained[4] for the upper and lower surface, we will only consider here the calculation of lift and drag due to the leading edge.

For the viscous part, the analysis is more complicated since it is necessary to obtain :

- the transition front delimiting the laminar and the turbulent regions
- the radiative equilibrium wall temperature associated to each point of the waverider surface
- the shear stresses calculated at the corresponding wall temperature
- the integration of the shear stresses on the complete vehicle

Section 1 Leading edge inviscid lift and drag

Half of the waverider planform is formed by 51 points where we already have defined a radius and a sweep angle (fig.8). But, to calculate the leading edge drag, the pressure distribution needs to be determined too. Since we are dealing with a hypersonic vehicle and a stagnation region, we know that the modified Newtonian theory does a good job of predicting the pressure distribution around blunt bodies. Moreover, it was also demonstrated that this pressure distribution is not affected

by the sweep angle and the flow nature. We can therefore state that the pressure distribution around the leading edge at a point i will vary as:

$$Cp(\tau) = Cp_a(\Lambda_i)\cos^2(\tau) \tag{2}$$

where according to the modified Newtonian theory:

$$Cp_a(\Lambda_i) = Cp_t\ \cos^2(\Lambda_i) \tag{3}$$

with

$$Cp_t = \frac{p_{02} - p_\infty}{q_\infty} \tag{4}$$

Therefore, at any station i, we will have :

$$Cp(\tau) = Cp_t\ \cos^2(\Lambda_i)\ \cos^2(\tau) \tag{5}$$

The axial coefficient c''_{a_i} can be calculated from the integration of the pressure distribution in the reference axis x", z as shown in figure 8 and 9.

$$c''_{a_i} = \frac{1}{c}\int_{LE}^{TE}(Cp_u - Cp_l)\,dz \tag{6}$$

$$c''_{a_i} = \frac{1}{R_i(1+\cos\delta_i)}\left(\int_{LE}^{TE} Cp_u\ dz\ - \int_{LE}^{TE} Cp_l\ dz\right) \tag{7}$$

$$c''_{a_i} = \frac{1}{(1+\cos\delta_i)}\left(\int_0^{\frac{\pi}{2}} Cp(\tau)\ \cos\tau\, d\tau\ \ + \int_0^{\frac{\pi}{2}-\delta_i} Cp(\tau)\ \cos\tau\, d\tau\right) \tag{8}$$

Since

$$Cp(\tau) = Cp_t\ \cos^2(\Lambda_i)\ \cos^2(\tau) \tag{9}$$

we can replace it in the above equation and integrate over the boundaries.

$$c''_{a_i} = \frac{1}{3} \frac{Cp_t \cos^2 \Lambda_i}{(1+\cos\delta_i)} \left(2 + \cos\delta_i(\sin^2\delta_i + 2)\right) R_i \tag{10}$$

By definition,

$$c''_{a_i} = \frac{a''_i}{q_\infty c} = \frac{a''_i}{q_\infty R_i(1+\cos\delta_i)} \tag{11}$$

Therefore,

$$\frac{a''_i}{q_\infty} = \frac{1}{3} Cp_t \cos^2\Lambda_i \left(2 + \cos\delta_i(\sin^2\delta_i + 2)\right) \tag{12}$$

Since a''_i represents the axial force per unit span perpendicular to the planform shape at point i, only the component parallel to the x axis will participate to the drag of the vehicle. Defining

$$\frac{d''_i}{q_\infty} = \frac{a''_i}{q_\infty} \cos\Lambda_i \tag{13}$$

where d''_i is the drag per unit span in the x direction. Assuming now that this quantity will vary linearly from d''_i to d''_{i+1} between s_i and s_{i+1} we can calculate the drag due to this segment of the leading edge.

$$\frac{D_i}{q_\infty} = \frac{d''_i + d''_{i+1}}{2q_\infty}(s_{i+1} - s_i) \tag{14}$$

Summing on all the segments, we obtain the total drag

$$\frac{D}{q_\infty} = \sum_{i=1}^{imax-1} \frac{D_i}{q_\infty} \tag{15}$$

Finally, the leading edge drag coefficient for both sides is obtained as

$$C_{D_{LE}} = 2\frac{D}{q_\infty}\frac{1}{S_{Planform}} \tag{16}$$

$$C_{D_{LE}} = \frac{Cp_t}{3}\frac{1}{S_{Planform}}\sum_{i=1}^{imax-1}[(R_i\cos^3\Lambda_i(2+\cos\delta_i(\sin^2\delta_i+2))+ \\ R_{i+1}\cos^3\Lambda_{i+1}(2+\cos\delta_{i+1}(\sin^2\delta_{i+1}+2)))(s_{i+1}-s_i)] \quad (17)$$

Due to the non symmetry of the leading edge design, this configuration will produce a small amount of negative lift. Applying the same assumption as above, this quantity can be expressed as :

$$C_{L_{LE}} = -\frac{Cp_t}{3}\frac{1}{S_{Planform}}\sum_{i=1}^{imax-1}[(R_i\cos^2\Lambda_i\sin^3\delta_i+ \\ R_{i+1}\cos^2\Lambda_{i+1}\sin^3\delta_{i+1})(s_{i+1}-s_i)] \quad (18)$$

In this simplified analysis, the calculation of the lift and the drag due to the leading edge has neglected the presence of the anhedral angle which is usually small on waveriders. This angle, when combined with the axial force a_i'' would eventually produce a small amount of positive lift.

Section 2 The prediction of transition

Transition at the attachment line of the leading edge

Let's consider a simple cylinder of very large span placed in a uniform flow such that the flow is normal to the spanwise generators. In this situation, the boundary layer which forms on the body will be two-dimensional and begin at the stagnation line. In this case, we would always expect to find a region of laminar flow near the stagnation line because the Reynolds number based upon local velocity tends to zero as the stagnation line is approach. If the cylinder is now slightly swept at an angle Λ (fig.10), the flow outside the boundary layer becomes three dimensional. Therefore, the application of sweep produces an additional velocity component tangent to the cylinder and we must determine what effect sweep will have on the transition behavior of this flow.

If we now assume that the Reynolds number is infinitely large, the boundary layer on the cylinder surface has zero thickness. In this case we can consider that a

particular stream surface will correspond to the swept cylinder surface. This stream surface will encounter first the line AA and then divides with one branch following the upper surface and the other following the lower branch of the body. The line AA is called the "attachment line". In the 2D case, the attachment line AA is also the locus of two-dimensional stagnation points. In the case of a finite Reynolds number, the attachment line is taken to be the projection of the dividing stream surface onto the surface of the body (fig.11). In order to characterize the transition along the leading edge, Poll[11] defines $\bar{R}$ as a characteristic Reynolds number which can be used as a similarity parameter for the attachment line boundary layer even when the flow is transitional or turbulent. $\bar{R}$ is defined as follow :

$$\bar{R} = \frac{V_e \eta}{\nu_e} \tag{19}$$

and

$$\eta = \left(\frac{\nu_e}{(du_e/dx)_{x=0}} \right)^{1/2} \tag{20}$$

is a boundary layer characteristic length.

A large bulk of Wind-tunnel data and flight test experiments demonstrated that in the presence of large boundary layer tripping devices such as streamwise end-plates, boundary layer fences, isolated three-dimensional roughness elements or two-dimensional trip wires, transition at the attachment line begins when $\bar{R}$ exceeds approximately 250.

When the surface on which the attachment line boundary layers form is smooth and there are no sources of upstream disturbances, the transition will be the result of the amplification of small fluctuations always present in the freestream. In such a case, the laminar flow will selectively amplify certain disturbances characterized by their frequency and wave number.

Therefore, wave packets will appear in the boundary. As the wave packets are convected along the leading edge, the disturbance amplitudes increase and eventually

break down to form turbulent spots. The occurrence of turbulent spots, or bursts marks the onset of transition. This process is similar to that which is observed in two-dimensional flows with low freestream disturbances. For small tripping devices or smooth surfaces, it was found that transition was delayed until much higher values of $\bar{R}$ were reached ($\bar{R} \geq 570$).

In order to examine more closely the effect of surface roughness or tripping devices, Poll extended the swept cylinder experiments to investigate the response of the laminar attachment line boundary layer to the presence of trip wires of various diameters. The results of this exercise are summarized in figure 12 which shows the value of $\bar{R}$ necessary for the observation of the onset of transition at a certain distance s from a trip wire with a diameter d.

These results indicate that the transition behavior of the infinite swept attachment line may be separated into four distinct regimes :

First regime : $d/\eta \leq 0.8$

For very small values of d, the results are indistinguishable from the free transition results. The values of $\bar{R}$ for transition onset are high and the turbulence is the result of an instability of the laminar flow to the small disturbances present in the freestream. This region is bounded by a critical value of d/η and for values of d/η greater than this limiting level, the transition location is determined by disturbances introduced by the wire. The behavior is qualitatively similar to that observed in the flat plate boundary layer where the concept of a maximum tolerable roughness height is well established. However, roughness height comparisons have indicated that the attachment line is much less sensitive to a trip wire.

Second regime : $0.8 \leq d/\eta \leq 1.6$

When the trip wire is sized such that transition occurs between an $\bar{R}$ of 400 and 600, it is found that bursts of turbulence still occur first at large spanwise

distances downstream of the trip. However, the laminar perturbation which precedes the turbulent burst is no longer a packet of Tollmien-Schlichting waves but discreet disturbances traveling along the attachment line. Disturbances emanating from the trip wire dominate the transition process and the value of $\bar{R}$ for transition exhibits a strong dependence upon d/η.

Third regime : $1.6 \leq d/\eta \leq 2.0$

If the trip diameter is increased still further, the turbulent bursts originate at the trip wire and then propagate indefinitely along the span. The onset of transition is observed at all spanwise stations at the same value of $\bar{R}$.

Fourth regime : $d/\eta > 2.0$

In this case, the large trip wires or any gross disturbance like a wing-fuselage junction produce a similar response in the boundary layer. If the boundary layer is subjected to gross disturbances from an isolated source, transition begins simultaneously at all those attachment line stations which are more than 2000η downstream from the disturbance source as $\bar{R}$ exceeds 250.

When the trip size is such that transition begins at an $\bar{R}$ of less than 250, the turbulent bursts still originate near the trip wire but decay and ultimately disappear as they convect along the attachment line if $\bar{R}$ stays below 250 at all those attachment line stations. Therefore, an $\bar{R}$ of 250 represents a lower limit for the indefinite propagation of turbulence along a swept attachment line when the boundary layer is subjected to a very large disturbance. This regime is the one of most direct practical interest for the following reasons:

- when wing/fuselage or tail/fuselage or nacelle/fuselage junctions will be present on the vehicle, they will act as a gross disturbance and we will have to consider that the transition along the attachment line will take place in this regime.

- if such a wing/fuselage junction is not present as in the case of the waverider, this regime will also be representative of the roughness state (d) of the leading edge on a conventional vehicle as we will see it later on.

The variation of $\bar{R}$ with d/η and s/η for complete turbulence is extracted from reference 12 and given in figure 13. By using the Emmons probability theory for transition, a model of the attachment line transition process was developed by Poll[13]. He concluded that, in the case of gross contamination, the intermittency at an infinite swept attachment line depends upon the parameters $\bar{R}$, η and s in such a way that :

$$\Gamma = 1 - EXP\left[-\left(\frac{\bar{R}-245}{233}\right)\left(\frac{s}{\bar{R}\eta}+10\right)\right] \quad with \ \frac{s}{\bar{R}\eta} \geq 8 \ and \ \bar{R} \geq 245 \qquad (21)$$

Therefore, while under certain circumstances the onset of transition may be independent of spanwise position s, the completion of transition is always dependent upon s.

Since the waverider presents no discontinuity in its planform shape, its attachment line along the leading edge is not subject to boundary layer contamination due to a wing fuselage junction. It was thus decided to consider in the frame of this study two test cases :

- a so called "smooth" leading edge where d is such that d/η is always less than 0.4 (first regime).
- a so called "rough" leading edge where d is such that d/η is always higher than 2.4 (fourth regime).

Since the transition for the smooth leading edge cannot be described by the intermittency function Γ, it was decided for both cases to use the values of $\bar{R}$ and s/η as given in figure 12 and 13 for the onset and the completion of turbulence.

The effect of compressibility

Most of the results described up to here were conducted by Poll at subsonic speed. He later extended his work[13] to include the effect of compressibility on the transition at the attachment line. In his study, he only considered test cases in which transition was clearly the result of gross upstream contamination (fourth regime). He found that all the available data could be correlated by a single value of the attachment line similarity parameter $\bar{R}$, provided that the temperature dependent properties were evaluated at some reference temperature T_* (fig.14). The compressible version of $\bar{R}$ was defined as $\bar{R}_*$ in the following way :

$$\bar{R}_* = \bar{R} \sqrt{\left(\frac{\nu_e}{\nu_*}\right)} \tag{22}$$

where

$$T_* = T_e + 0.10(T_w - T_e) + 0.60(T_r - T_e) \tag{23}$$

Later on, experiments conducted at Mach = 3.5 in the Pilot Low-Disturbance Wind-tunnel at NASA Langley[14] demonstrated that Poll's criteria was valid not only in the fourth regime but also for the three others when compressibility effects were taken into account.

The results show that end plates or large trips near the upstream end of the cylinder cause turbulent flow along the entire attachment line of the models over the freestream Reynolds number range tested (consistent with Poll's fourth regime). When all end disturbance sources are removed, transition occurs on the attachment line independently of freestream noise levels and in agreement with the first regime. Finally, with the addition of small roughness elements on the cylinder attachment line, transition occurs at lower values of the Reynolds number, depending on both

the roughness height and the Wind-tunnel noise level (characteristic of the second and third regime).

The evaluation of R_*

With

$$\bar{R} = \frac{V_e \eta}{\nu_e} \tag{24}$$

and

$$\eta = \left(\frac{\nu_e}{(du_e/dx)_{x=0}} \right)^{1/2} \tag{25}$$

we have

$$\bar{R} = \frac{V_e}{\sqrt{\nu_e (du_e/dx)_{x=0}}} \tag{26}$$

thus

$$\bar{R}_* = \bar{R} \sqrt{\frac{\nu_e}{\nu_*}} = \frac{V_e}{\sqrt{\nu_* (du_e/dx)_{x=0}}} \tag{27}$$

Introducing the Reynolds number based on the freestream conditions and the local diameter D of the leading edge, we have :

$$\bar{R}_* = \sqrt{\frac{\nu_\infty}{\nu_*}} \frac{V_e}{V_\infty} \frac{1}{\sqrt{\frac{D}{V_\infty}(du_e/dx)_{x=0}}} \sqrt{R_{\infty,D}} \tag{28}$$

Defining now the freestream velocity in terms of its normal and tangential components to the leading edge we write :

$$\cos \Lambda = \frac{u_{\infty,n}}{V_\infty} \quad or \quad V_\infty = \frac{u_{\infty,n}}{\cos \Lambda} \tag{29}$$

Since $v_\infty = v_2 = V_e = V_\infty \sin \Lambda$ we also have

$$\frac{V_e}{V_\infty} = \sin \Lambda \tag{30}$$

Replacing equations (29) and (30) in (28) we obtain :

$$\bar{R}_* = \sqrt{\frac{\nu_\infty}{\nu_*}} \sin \Lambda \frac{1}{\sqrt{\cos \Lambda \frac{D}{u_{\infty,n}}(du_e/dx)_{x=0}}} \sqrt{R_{\infty,D}} \tag{31}$$

We still need to define the pressure gradient in terms of known quantities. We know that in the stagnation region we can write[8]

$$\left(\frac{du_e}{dx}\right)_{x=0} = \left(\frac{2}{D}\sqrt{\frac{2(p_e - p_\infty)}{\rho_e}}\right)_{x=0} \tag{32}$$

Therefore,

$$\frac{D}{u_{\infty,n}}\left(\frac{du_e}{dx}\right)_{x=0} = \left(\frac{2}{u_{\infty,n}}\sqrt{2\frac{p_e}{\rho_e}\left(1 - \frac{p_\infty}{p_e}\right)}\right)_{x=0} \tag{33}$$

$$\frac{D}{u_{\infty,n}}\left(\frac{du_e}{dx}\right)_{x=0} = \left(\frac{2}{u_{\infty,n}}\sqrt{2R_{gas}T_e\left(1 - \frac{p_\infty}{p_e}\right)}\right)_{x=0} \tag{34}$$

Since

$$M_{\infty,n} = \frac{u_{\infty,n}}{\sqrt{\gamma R_{gas} T_\infty}} \tag{35}$$

we can replace it in the previous equation to obtain :

$$\frac{D}{u_{\infty,n}}\left(\frac{du_e}{dx}\right)_{x=0} = \left(\frac{2}{M_{\infty,n}}\sqrt{\frac{2}{\gamma}\frac{T_e}{T_\infty}\left(1 - \frac{p_\infty}{p_e}\right)}\right)_{x=0} \tag{36}$$

$$\left(\cos\Lambda\frac{D}{u_{\infty,n}}\left(\frac{du_e}{dx}\right)_{x=0}\right)^{1/2} = \left(\frac{2}{M_\infty}\right)^{1/2}\left(\frac{2}{\gamma}\frac{T_e}{T_\infty}\left(1 - \frac{p_\infty}{p_e}\right)\right)^{1/4}_{x=0} \tag{37}$$

According to the modified Newtonian theory, we can write

$$p_e - p_\infty = (p_{02} - p_\infty)\cos^2\Lambda \tag{38}$$

where

$$\frac{p_{02}}{p_\infty} = f(M_\infty, \gamma) \tag{39}$$

is given by the Rayleigh Pitot tube formula. We still need to evaluate the temperature ratio :

$$\frac{T_e}{T_\infty} = \frac{T_e}{T_2}\frac{T_2}{T_\infty} \quad and \quad \frac{T_e}{T_2} = \left(\frac{p_e}{p_\infty}\frac{p_\infty}{p_2}\right)^{\frac{\gamma-1}{\gamma}} \tag{40}$$

$$\frac{p_\infty}{p_2} = \frac{p_1}{p_2} = f_1(M_\infty\cos\Lambda, \gamma) \quad \text{(normal shock relation)} \tag{41}$$

$$\frac{T_2}{T_\infty} = \frac{T_2}{T_1} = f_{II}(M_\infty \cos\Lambda, \gamma) \qquad \text{(normal shock relation)} \tag{42}$$

A last step needs to be completed in order to evaluate the kinematic viscosity ratio :

$$\sqrt{\frac{\nu_\infty}{\nu_*}} = \sqrt{\frac{\mu_\infty}{\mu_*}\frac{\rho_*}{\rho_\infty}} \tag{43}$$

Using Sutherland's law of gas viscosity, we can calculate the ratio μ_∞/μ_* as

$$\frac{\mu_\infty}{\mu_*} = \left(\frac{T_\infty}{T_*}\right)^{3/2} \frac{T_* + S}{T_\infty + S} \quad with \quad S = 110 \quad K \tag{44}$$

In order to calculate ρ_*/ρ_∞ we will assume a constant pressure through the boundary layer. Therefore, the density ratio can be expressed in terms of the temperature and pressure ratios.

$$\frac{\rho_*}{\rho_\infty} = \frac{p_*}{p_\infty}\frac{T_\infty}{T_*} = \frac{p_e}{p_\infty}\frac{T_\infty}{T_*} \tag{45}$$

Since we know how to evaluate the pressure ratio, the only quantity which remains to be evaluated is the reference temperature. According to Poll[13], we have :

$$T_* = T_e + 0.10(T_w - T_e) + 0.70(T_r - T_e) \tag{46}$$

with the definition of the recovery factor

$$r = \frac{T_r - T_e}{T_0 - T_e} \quad and \quad T_0 = T_\infty\left(1 + \frac{\gamma - 1}{2}M_\infty^2\right) \tag{47}$$

We have now identified all the variables to evaluate $\bar{R}_*$.

Finally, we can rewrite $\bar{R}_*$ in the following way :

$$\bar{R}_* = \sqrt{R_{\infty,D}}\frac{\sqrt{M_\infty}\sqrt{\frac{\nu_\infty}{\nu_*}}\sin\Lambda}{\left(\frac{8}{\gamma}\frac{T_e}{T_\infty}\left(1 - \frac{p_\infty}{p_e}\right)\right)^{1/4}} \tag{48}$$

It appears immediately that increasing the diameter or the unit Reynolds number will be unfavorable for the transition at the attachment line, since $\bar{R}_*$ will increase.

An increase in sweep angle is also unfavorable since both p_e/p_∞ *and* T_e/T_∞ will decrease and thus increase the value of $\bar{R}_*$.

The effect of the wall temperature can also be analyzed through the viscosity ratio. When the wall temperature is increased, the reference temperature will increase and both the density ratio and the dynamic viscosity will decrease. Increasing the wall temperature along the attachment line will have a favorable effect.

The evaluation of η

As defined by Poll, we have :

$$\eta = \left(\frac{\nu_e}{(du_e/dx)_{x=0}} \right)^{1/2} \tag{49}$$

Making use of the previous derivation of $(du_e/dx)_{x=0}$ we have

$$\eta = \left(\frac{D\mu_e \sqrt{R_{gas} T_e}}{p_e \sqrt{8\left(1 - \frac{p_\infty}{p_e}\right)}} \right)^{1/2} \tag{50}$$

where

$$\frac{\mu_e}{\mu_{ref}} = \left(\frac{T_e}{T_{ref}} \right)^{3/2} \frac{T_{ref} + S}{T_e + S} \tag{51}$$

with S=110 K, T_{ref}=273.1 K and μ_{ref}=0.1716 10^{-4}kg/(m s).

Transition due to cross flow instability

Let's assume that transition along the attachment line has not taken place and the flow is still laminar. In the region close to the attachment line, the streamlines at the edge of the boundary layer are highly curved (fig.11). Along any of these streamlines there is a favorable pressure gradient and we should expect that the flow will be stable to small disturbances. However, it turns out that this is not the case. Poll[12] explains that by simply sweeping the cylinder shown in figure 11, it is possible to destabilize the boundary layer since the sweep leads directly to the formation of

velocity profiles presenting inflection points (fig.15 and fig.16). To properly determine the onset of transition due to cross-flow instability, the most reliable criteria seems to be the characteristic local Reynolds number X.

X is based on the cross-flow velocity profile shown in figure 16 and corresponding to the case $\epsilon = \theta - \frac{\pi}{2}$. X is defined as :

$$X = \frac{C_{max} Z_{0.01 C_{max}}}{\nu} \tag{52}$$

Where C_{max} is the maximum cross-flow velocity component in the profile corresponding to $\epsilon = \theta - \frac{\pi}{2}$ and $Z_{0.01 C_{max}}$ is the point where this velocity has dropped to 1% of its maximum value. An excellent correlation seems to exist between the critical value of X and the streamwise shape factor H_{11} as shown in figure 17 (excluding situations where the streamwise flow is unstable to small disturbances). Unfortunately, this kind of transition criteria requires a detailed boundary layer calculation in the leading edge region that the waverider code does not provide. Therefore, it was decided to take into account the destabilizing effect due to sweep by simpler means. In 1985, Bowcutt[2] curve fitted experimental data obtained on blunt flat plate with a swept leading edge in such a way that the transition Reynolds number in the streamwise direction for a swept leading edge $(Re_{xt})_\Lambda$ could be related to the unswept value $(Re_{xt})_{\Lambda=0}$ by a function of the sweep angle only (fig.18). Since $(Re_{xt})_{\Lambda=0}$ will be determined as explained later on and the sweep angle distribution is known, we are able to calculate $(Re_{xt})_\Lambda$ for each streamline. Of course this procedure will be applied only for the streamlines where it was found that the flow was still laminar at the attachment line. When the flow was found to be turbulent at the attachment line, this criteria does not apply since the flow will remain turbulent on the streamline from the leading edge to the trailing edge of the vehicle.

The possibility of relaminarization

The reversion of a turbulent boundary layer to the laminar state in a region

of strong favorable pressure gradient is a well established phenomenon in two-dimensional and axi-symmetric flows.

In a simplified analysis, Poll[11] demonstrates that the conventional relaminarization parameter reaches its peak value very close to the attachment line. Therefore, turbulence resulting from either attachment line contamination or cross-flow instability is unlikely to be relaminarized in the strong favorable pressure gradients which exists in the streamwise direction near the leading edge of a swept wing.

Although relaminarization is not likely to occur in the streamwise direction, we will underline here that in the spanwise direction (along the attachment line) relaminarization might occur since the attachment line cannot support bursts of turbulence when $\bar{R}_*$ drops below 245 (cf. section 2 topic 1).

Transition in the streamwise direction

In the previous work of Bowcutt, Corda and McLaughlin a correlation based on transition Reynolds number of a large bulk of measurements for sharp cones (fig.19) was used. This correlation, when compared to a larger set of experiments (fig.20) grouping flight measurements and quiet wind tunnel experiments, shows a good agreement with the wind tunnel data correlations presented in figure 20.

Therefore, due to the well known adverse effect of wind tunnel radiated noise on the transition Reynolds number, it was decided to try another correlation based on ballistic tests performed on sharp cones by Sheetz[15]. These data can be correlated in such a way that the transition Reynolds number could be expressed as a function of the edge Mach number :

$$Re_{xt} = 6400(Me)^{3.66} \tag{53}$$

This relation, also presented on figure 19, shows in the range $6 \leq Me \leq 16$ a better agreement with flight data and the e^N method than Bowcutt's curve fit.

Both correlations do a very poor job of predicting transition when the edge Mach number drops below 5. As stated by Malik[16], at low hypersonic speed ($M_\infty \leq 7$) the first Tollmien-Schlichting mode dominates for adiabatic wall conditions. For cold walls, the role of the second mode becomes more important due to the destabilizing effect of cooling. We will see later on that when radiative equilibrium is obtained at low hypersonic Mach number ($M_\infty = 5$), we can always consider that $T_w/T_0 \approx 0.8$ is a good estimate. Therefore, for $M\infty \leq 7$ and $T_w/T_0 \approx 0.8$, we will consider a constant transition Reynolds number of 15 million.

At higher Mach number $10 \leq M_\infty \leq 20$, T_w/T_0 of the order of 0.1 or less is a good estimate for radiative equilibrium wall temperature. For these conditions, we know that the second mode is dominant and Sheetz's transition criteria does a relatively good job for $M_e \geq 6$.

In fact, for $6 \leq M_e \leq 16$, Sheetz's and Bowcutt's criteria can be seen as the upper and lower band bracketing almost all the flight data.

Section 3 The heat transfer evaluation

The heat transfer evaluation on the complete vehicle will be separated in three distinctive regions : the nose region, the attachment line along the leading edge, and the upper and lower surfaces. The heat transfer rates in the two first regions will be obtained through analytical correlations developed by Tauber[17]. These relations apply in the flight regime where boundary layer theory is valid and the flowfield is in equilibrium. The peak hypersonic aerodynamic heating experienced by missiles or manned vehicles always occurs in the continuum flow regime. However, for small nose radius or wing leading edge radii, these regions of the vehicle can experience low density flow phenomena which alter the heating. One parameter that characterizes low-density flows is the Knudsen number, Kn, which is the ratio of molecular mean free path to a characteristic length. The increase in stagnation point heat transfer

coefficient with Knudsen number was calculated by Moss and is shown in figure 21. We see in this figure that there is a good agreement between the direct Monte-Carlo simulation, the viscous shock layer solution with no velocity slip and the viscous shock layer solution with velocity slip for Kn less than 0.05. Beyond that point, the viscous shock layer solution ceases to be valid and overpredicts the heat transfer calculated by the DMSC. Since the correlations developed by Tauber will assume continuum flow, we need to ensure that the Kn number will always be less than 0.05. If a characteristic length R_{min}, equal to the minimum leading edge radius is assumed, then :

$$Kn = \frac{\lambda_\infty}{R_{min}} = 0.05 \quad or \quad R_{min} = 20\lambda_\infty \tag{54}$$

Considering the definition of the mean free path,

$$\lambda_\infty = \frac{1}{\sqrt{2}\pi d^2 n_\infty} \quad with \quad n_\infty = \frac{p_\infty}{kT_\infty} \tag{55}$$

where d = 3.789 10^{-10} m for pure N_2 and k = 1.38054 10^{-23} J/K.

R_{min} can be rewritten as :

$$R_{min} = \frac{20}{\sqrt{2}\pi d^2}\frac{kT_\infty}{p_\infty} \tag{56}$$

R_{min} represents the smallest radius that we can consider at a given altitude in order to avoid low density effects. Therefore, we will always make sure that the smallest radius on the leading edge is greater than this minimum value. When this condition is not met, the entire waverider will be rejected by the optimization procedure.

The heat transfer rates on the upper and lower surfaces will be evaluated assuming a 2D flowfield along the streamlines through the reference temperature method and the Reynolds analogy.

Finally, we will consider that the surface of the vehicle is a fully catalytic wall where no boundary layer mass addition is present. Assuming a fully catalytic wall is

a conservative approach and makes the heat transfer rates independent of the choice of heat shielding material.

Convective heat transfer evaluation in the nose region

Tauber[17] demonstrated that the heat transfer rate at the stagnation point of an axisymmetric body can be expressed as :

$$(\dot{q}_w)_{axi} = (1.90\ 10^{-4})\ V_\infty^3 \left(1 - \frac{h_w}{H_0}\right)\left(\frac{\rho_\infty}{R_y}\right)^{1/2} \quad (Watt/m^2) \tag{57}$$

- R_y in meters
- ρ in kg/m^3
- V in m/s

This relation is derived from a similar solution of the boundary layer equations where air is assumed to be a binary mixture of "air atoms' and "air molecules" in thermodynamic equilibrium. The equations are then numerically integrated using the composition and thermodynamic properties of air in chemical equilibrium and a unit Lewis number.

The resulting correlation, almost identical to the Marvin and Deiwert correlation, is compared with experimental data in figure 22. Up to a speed of 14 km/s all four correlations lie within the data spread, which is about ± 25%.

By using the relation given by Hamilton[18], we can obtain the 3D stagnation heat transfer from the axisymmetric value.

$$(\dot{q}_w)_{3D} = \sqrt{\frac{1+K}{2}}\ (\dot{q}_w)_{axi} \tag{58}$$

$$K = \frac{R_y}{R_x} \quad for\ \ R_y \leq R_x \tag{59}$$

$$K = \frac{R_x}{R_y} \quad for \;\; R_x \leq R_y \tag{60}$$

Note that K ranges always between 0 and 1. For K=1 we have an axisymmetric nose and for K=0 we have a cylinder. R_x has to be seen in our case as the radius joining the stagnation point and the second point of the planform (fig.7).

The wall enthalpy was calculated assuming a calorically perfect gas at the wall.

$$h_w = c_p \; T_w \tag{61}$$

Since we are considering a fully catalytic wall, a high pressure region and wall temperature not exceeding 1900 K for any realistic configuration, we see that the assumption of a calorically perfect gas at the wall is reasonable. Only the effect of vibrational excitation is neglected in that case.

When the stagnation heat transfer at the nose is known, the heat transfer at the second point of the planform is calculated according to the value of K.

- For $0 \leq K \leq 0.5$, the heat transfer distribution between the stagnation point and the second point will be close to the heat transfer distribution existing on an unswept cylinder of radius R_x. For this range of K, we can write[8]

$$\frac{(\dot{q}_w)_{i=2}}{(\dot{q}_w)_{stag}} = 0.7(\cos \Lambda_{i=2})^{3/2} + 0.3 \tag{62}$$

  where $\Lambda_{i=2}$ represents the sweep angle at the second point.

- If $0.5 \leq K \leq 1.0$, the heat transfer distribution will be closer to the heat transfer distribution of an axisymmetric body and we can use[8] :

$$\frac{(\dot{q}_w)_{i=2}}{(\dot{q}_w)_{stag}} = \cos \Lambda_{i=2} \tag{63}$$

Convective heat transfer evaluation at the leading edge

The heat transfer along a cylindrical leading edge of a finite length wing can be approximately calculated using the expression developed by Rubesin and given in reference 17.

$$(\dot{q}_w)_{le} = \left((\dot{q}_w)^2_{cyl} + \sin^2\Lambda\ (\dot{q}_w)^2_{fp}\right)^{1/2} \cos\alpha \tag{64}$$

Since we will only deal with a waverider at zero angle of attack and the attachment line of the leading edge, we can set α to zero. But we must realize that this equation, for highly swept leading edges, is limited to small angles of attack since the stagnation line moves from the cylindrical leading edge onto the lower surface of the wing as the angle of attack increases.

The heat transfer rate for the infinite swept cylinder is calculated with[17]:

$$(\dot{q}_w)_{cyl} = (1.29\ 10^{-4})\ V_\infty^3 \left(1 - \frac{h_w}{h_{aw}}\right)\left(\frac{\rho_\infty}{R_y}\right)^{1/2} * \cos\Lambda\left(1-0.18\sin^2\Lambda\right) \quad (Watt/m^2) \tag{65}$$

$$h_{aw} = h_\infty + \frac{V_\infty^2}{2}\left(1-0.18\sin^2\Lambda\right) \tag{66}$$

For the inclined laminar flat plate we have[17]:

$$(\dot{q}_w)_{fp} = (2.42\ 10^{-5})\ V_\infty^{3.2}\left(1 - \frac{h_w}{h_{aw}}\right)\left(\frac{\rho_\infty \cos\delta}{s}\right)^{1/2} \sin\delta \quad (Watt/m^2) \tag{67}$$

$$with \quad \delta = \frac{\pi}{2} - \Lambda \tag{68}$$

$$and \quad h_{aw} = h_\infty + \frac{V_\infty^2}{2}\left(1-0.15\sin^2\Lambda\right) \tag{69}$$

As in the case of the axisymmetric stagnation point correlations, these two relations are derived from exact similar solutions and have assumed the same air properties.

To make sure that the heat transfer predicted at the second point of the planform by the swept cylinder correlation is equal to the one predicted by the stagnation point correlation, an artificial origin is created for the laminar flat plate correlation. Therefore, no discontinuity in the heat transfer at the second point of the planform shape will exist. Note also that this manipulation is somewhat conservative from the heat transfer point of view since it will slightly raise the laminar flat plate contribution of the downstream points.

When transition along the leading edge is detected, the evaluation of the flat plate contribution has to be done through a turbulent correlation. This correlation, developed by Tauber[17] is obtained by using :

- the Reynolds analogy,

$$St = \frac{C_f}{2\ Pr^{2/3}} \tag{70}$$

- the Blasius incompressible, turbulent, skin-friction equation for Reynolds number less than 10 million,

$$\frac{C_f}{2} = \frac{0.0296}{(Re_*)^{0.2}} \tag{71}$$

- the Schultz-Grunov equation for Reynolds number above 10 million,

$$\frac{C_f}{2} = \frac{0.185}{(log_{10} Re_*)^{2.584}} \tag{72}$$

The '*' denotes that the quantity is evaluated at the conditions corresponding to the reference enthalpy h_*.

$$h_* = 0.18 h_{aw} + 0.32 h_e + 0.5 h_w \tag{73}$$

Using the thermodynamic and transport properties of air in chemical equilibrium, Tauber calculated the heat transfer rate at altitudes from 3 to 60 km and speed from 1 to 11 km/s. His correlation which is accurate to ± 15%, may be expressed as follows :

- for $1500 \leq V_\infty \leq 3960$ m/s

$$(\dot{q}_w)_{fp} = (3.72\ 10^{-4})\ V_\infty^{3.37}\left(0.9 - \frac{hw}{h_{aw}}\right)\frac{(\rho_\infty \sin^2\delta \cos^{2.22}\delta)^{0.8}}{(s - s_{onset})^{0.2}(T_w/555)^{0.25}} \quad (Watt/m^2) \tag{74}$$

- and for $V_\infty \geq 3960$ m/s.

$$(\dot{q}_w)_{fp} = (2.45\ 10^{5})\ V_\infty^{3.7}\left(0.9 - \frac{h_w}{h_{aw}}\right)\frac{(\rho_\infty \sin^2\delta \cos^{2.62}\delta)^{0.8}}{(s - s_{onset})^{0.2}} \quad (Watt/m^2) \tag{75}$$

$$with \quad \delta = \frac{\pi}{2} - \Lambda \tag{76}$$

$$and \quad h_{aw} = h_\infty + \frac{V_\infty^2}{2}\left(1 - 0.11 \sin^2\Lambda\right) \tag{77}$$

When transitional heat transfer values have to be evaluated, we will assume that the flat plate contribution will vary linearly with the distance s between the laminar value at the onset of transition and the turbulent value at the end of transition.

When the flow undergoes reverse transition or relaminarization, the same hypothesis is made but the heat transfer rate will vary from a turbulent value at the beginning of relaminarization to a fully laminar value at the end of relaminarization. In order to

calculate $(\dot{q}_w)_{fp}$ after relaminarization, a new origin has to be defined for the laminar correlation. This is done by imposing that the flat plate heat transfer contribution at the beginning of relaminarization be the same for the laminar and the turbulent correlation. Since the relaminarization length is predicted by our transition criteria, we are able to evaluate the laminar heat transfer value at the end of relaminarization and all the other downstream points.

Convective heat transfer evaluation on the waverider surface

In order to evaluate the viscous forces on the waverider, both Corda[3] and McLaughlin[4] have used the so called reference temperature method to predict the skin friction coefficient of laminar and turbulent flows. The equations used in their work are :

- For laminar flow

$$c_{f_{lam}} = 0.664(Re_s)^{-\frac{1}{2}}\left(\frac{T^*}{T_\infty}\right)^{(\omega-1)/2} \tag{78}$$

with

$$Re_s = \frac{\rho_e V_e s}{\mu_e} \tag{79}$$

T_* is defined by

$$\left(\frac{T_*}{T_\infty}\right) = 1 + 0.032M_e^2 + 0.58\left(\frac{T_w}{T_\infty} - 1\right) \tag{80}$$

and ω=0.75 which is the exponent of an assumed exponential variation of the viscosity, μ, where μ is defined as

$$\left(\frac{\mu_*}{\mu_\infty}\right) = \left(\frac{T_*}{T_\infty}\right)^{\omega} \tag{81}$$

- For turbulent flow

$$c_{f_{turb}} = \frac{0.0592}{(Re_{s*})^{0.2}} \tag{82}$$

where

$$Re_{s*} = \frac{\rho_* V_\infty s}{\mu_*} \tag{83}$$

The present study will also use the reference temperature method. The Stanton numbers are calculated through the Reynolds analogy. The Stanton number is defined as follows :

$$St = \frac{(\dot{q}_w)}{\rho_e V_e (h_{aw} - h_w)} \tag{84}$$

If a calorically perfect gas is assumed, equation 84 can be written as :

$$St = \frac{(\dot{q}_w)}{\rho_e V_e c_p \, (T_{aw} - T_w)} \tag{85}$$

Making use of the definition of the recovery factor, we obtain the laminar or the turbulent heat transfer rate through :

$$(\dot{q}_w) = r \rho_e V_e St \; c_p \, (T_0 - Tw) \tag{86}$$

where $r = \sqrt{Pr}$ for laminar flow and $r = Pr^{1/3}$ for turbulent flow.

Section 4 Evaluation of the equilibrium radiative heat transfer

We have seen in the previous chapter how to calculate the heat transfer brought by convection to the surface of a hypersonic vehicle. In steady or quasi-steady flight, part or the entire convective heat transfer brought by the fluid will be radiated by the vehicle surface. Therefore, heat transfer due to radiation constitutes an important natural cooling phenomenon that must be taken into account.

The radiative heat transfer emitted by a surface which has a wall temperature T_w is expressed as :

$$(\dot{q}_w)_{rad} = \epsilon \, \sigma \, (T_w^4 - T_\infty^4) \tag{87}$$

with

- ϵ = surface emissivity
- σ = Stefan-Boltzmann constant

For a given wall temperature of the surface the heat transfer balance at the wall is :

$$(\dot{q}_w(T_w))_{balance} = (\dot{q}_w(T_w))_{convect} - (\dot{q}_w(T_w))_{rad} \tag{88}$$

To maintain this given wall temperature, the heat transfer balance has to be absorbed either by an active cooling device or by the vehicle structure. Therefore, the heat transfer balance represents the amount of cooling necessary at a given point of the vehicle to maintain an imposed wall temperature.

If the vehicle structure doesn't provide any heat sink ($(\dot{q}_w)_{balance} = 0$), the wall temperature will reach a value which is such that the heat transfer losses by radiation balance the heat transfer due to convection. This temperature is called the radiative equilibrium wall temperature and is calculated using the following relation :

$$\left(\dot{q}_w(T_{w_{eq}})\right)_{balance} = \left(\dot{q}_w(T_{w_{eq}})\right)_{convect} - \left(\dot{q}_w(T_{w_{eq}})\right)_{rad} = 0 \tag{89}$$

In order to find this radiative equilibrium wall temperature, a zero finding algorithm due to Brent[19] was used since the convective and radiative heat transfer are both non-linear functions of the wall temperature. In other terms, it is necessary to iterate at each point of the waverider surface to obtain the radiative equilibrium wall temperature and the corresponding convective heat transfer.

The waverider code was set up in such a way that the maximum wall temperature at the leading edge and on the upper and lower surface could be independently specified by the user. The surface emissivity was in all cases arbitrary set to a value of 0.8.

When the radiative equilibrium temperature exceeds the maximum wall temperature allowed by the thermal protection system, the wall temperature is set to this maximum value and the convective heat transfer is recalculated using that value.

Therefore, the user can rapidly evaluate the amount of cooling necessary to maintain its maximum wall temperature by substracting the radiative heat transfer. The location and the extend of the surfaces which have to be cooled can easily be visualized by temperature contours on the waverider surface.

Section 5 Viscous forces integration

The procedure to integrate the viscous shear stresses is identical to what was used and described in detail in reference 4. However, differences in the transition front will appear since Bowcutt[2], Corda[3] and McLaughlin[4] have considered a simpler transition model than the one used in this study. In particular, they have assumed a constant and identical wall temperature on the upper and lower surface to calculate the shear stress distribution. In this study, the shear stress at each point of the waverider surface is evaluated at the corresponding radiative equilibrium wall temperature or the maximum wall temperature. The code will therefore provide a more accurate evaluation of the viscous forces. This will be particularly true at high Mach number where the difference between the temperature of the upper and lower surfaces will tend to increase.

Section 6 Definition of a thermal protection system

Leading edge

Three different types of generic leading edge concepts are listed below for an application such as the NASP.

- radiative or "passive" concept : the cooling relies simply on radiative cooling. It is a reliable and fail-safe solution which doesn't require coolant or pumps and controls.
- heat-pipes or "semi-passive" concept : the cooling relies on radiative cooling and heat pipes which transport heat to a cooler region of the wing where it is dissipated radiatively.
- heat-pipes and active cooling or "semi-active" concept : the semi-active concept uses heat-pipes with active cooling. The active cooling is used during the ascent and cruise portion of the flight. During the descent, since the heat transfer will be much lower, active cooling is not necessary and the concept is used in a semi-passive way. Since this concept requires some form of controls, it has to be considered as less reliable than the two first solutions. Nevertheless, it might be the only solution able to support high heating rates with no damages.

It should be also noted that pure active cooling, such as channel flow impingement or transpiration, could be used but offers even less reliability and requires heavier control systems. Therefore, these systems have to be disregarded for the leading edge.

It has thus been decided that the most suitable system for our waverider should be the semi-active concept. In reference 20, a carbon-carbon / refractory metal heat-pipe wing leading edge is studied in the context of the NASP.

This concept is designed to be redundant and fail-safe and to operate at temperature as high as 1900 K. This concept uses internal radiative cooling to supplement external radiative cooling during the ascent portion of the trajectory.

The design, shown in figure 23, features a carbon-carbon primary structure with refractory metal chordwise and spanwise. The heat-pipes are made of tungsten with lithium used as the working fluid. The heat-pipes are completely embedded within the carbon-carbon structure. The spanwise heat-pipes are much smaller in size than

the chordwise heat-pipes and are located only in the stagnation region.

Although carbon-carbon retains strength up to 3000 K, the maximum reuse temperature is limited to approximately to 1900 K by the coating required for anti-oxydation at elevated temperature. Note that, due to its properties, the carbon-carbon also offers some ablative protection in the event of a heat-pipe failure. The maximum temperature as a function of the stagnation heat transfer is presented in figure 24 for 3 cases : no heat-pipes, no internal cooling, and heat-pipes with internal cooling. For the first case, temperatures were approximated by the radiation equilibrium temperatures. Only the third case is able to maintain the maximum temperature below the temperature limit over the predicted heat transfer range for the ascent trajectory. As shown in the figures, the thermal limitations of the system are a maximum temperature limit of 1900 K and a maximum heat transfer rate of the order of 10.3 MW/m^2 (900 $Btu/ft^2\ s$). Due to its relative complexity, a minimum value of the leading edge radius must be imposed and was set according to the study[20] to 1.27 cm (0.5 inch).

Waverider surface

As in the case of the leading edge, different choices can be made according to the maximum temperature, the density, the reliability, etc., of the thermal protection system. Basically, the choice reduces to the three following categories of material[1]:

- carbon-carbon composites ($1650 \leq T_{max} \leq 2200\ C$)
    - advantages :
        - low specific gravity.
        - high modulus.
        - low thermal conductivity.
        - strength increases with temperature.

        - excellent thermal and mechanical shock resistance and toughness.
    - disadvantages :
        - oxidation is a problem but rates are not catastrophic in oxidizing atmosphere.
        - due to corrosion, coating is required for long life performance and the maximum temperature falls to 1650 C due to the coating.

- ceramic composites ($1400 \leq T_{max} \leq 1600\ C$)
    - advantages :
        - excellent oxidation resistance.
        - specific gravity, specific strength and specific modulus values are excellent.
    - disadvantages :
        - thermal stresses and thermal and mechanical shocks are more severe than with the carbon-carbon composites.

- superalloys of titanium ($T_{max} \leq 1100\ C$)

Chapter 4 Results and discussion

Section 1 Choice of flight trajectories

In order to determine test cases of interest corresponding to an application similar to the NASP, it was decided to choose two constant dynamic pressure trajectories. Values of 0.2 and 1.0 atm were chosen. The low value corresponds to what is believed by the airframe community to be the maximum admissible from a structural point of view. The high value corresponds to what is desired by the engine community to obtain the best performance of the scramjet. For both dynamic pressure trajectories, the waverider performances are analyzed at four different Mach numbers (5, 10, 15, 20). The flight conditions corresponding to each dynamic pressure and each Mach number are given in Table 1. Pressure and density were extracted from reference 21, in order to match the desired dynamic pressure as close as possible. The velocity ranges from 1500 m/s to 6800 m/s and the unit Reynolds number varies from 0.35 to 9.35 million per meter. The low dynamic pressure flight path is situated between 30 and 50 km of altitude and the high dynamic pressure trajectory is situated between 20 and 40 km. The two flight path are showed on a Mach-Altitude map on figure 25 which also features the "official " NASP trajectory.

Section 2 Choice of other parameters

The choice of an altitude and a Mach number does not represent the entire set of parameters which have to be chosen to run a test case. Another set of important parameters have to be defined in the input data file and we will review them one by one.

- The objective function for the optimization : a choice can be made between L/D, Cd, Volume or Volume efficiency. In this study, we will only consider waveriders maximized for L/D or Volume.

- The cone angle : associated with a given Mach number for the calorically perfect gas or with given freestream conditions in the case of a gas in chemical and thermodynamical equilibrium, fixes the streamlines of the generating conical flowfield. The choice of the cone angle has an impact on the optimized objective function. It was demonstrated [2,3] that for each flight condition there exists a certain value of the cone angle leading to the best optimum for the optimized objective function. Nevertheless, in the present study, the notion of best optimum was disregarded and an arbitrary well chosen value of 7.5 degree was considered in all cases.
- Type of gas : the program can be run with a generating flowfield corresponding to a calorically perfect gas or a gas in chemical and thermodynamic equilibrium. Since it has already been demonstrated[4] that the difference between the two cases is small for low altitude and Mach number smaller than 25, this study has considered a calorically perfect gas for the generating flowfield in all cases.
- Length of the vehicle : all test cases have considered a 60 meter long waverider.
- Geometric constraints : were placed on the vehicle maximum box size (0.4) and minimum slenderness ratio (0.075).
- Transition at the attachment line of the vehicle : the transition criteria at the attachment line depends on the surface roughness of the leading edge. For all the test cases we have considered a "rough" leading edge. This choice will be justified later on.
- Maximum wall temperature : according to chapter 3 section 6, a maximum wall temperature of 1900 K was chosen for the leading edge and the waverider body although they might be covered by different materials.
- Cooling and minimum radius : for the two test cases at Mach = 5, cooling is not necessary if carbon-carbon is used to protect the leading edge. Therefore, cooling was not included for in these two cases and the minimum radius of the

leading edge was set to 1 mm. For all the other test cases, cooling is required to maintain a maximum wall temperature of 1900 K. According to the geometry of the active cooling device, the minimum radius was set to 10 mm. Although the choice of cooling can be made in the input data file, the constraint on the minimum value of the radius has to be changed in the code itself.

The following options have to be modified in the code :

- Waverider's carving : the amount of carving is set in the program according to equation (1). For all cases, the parameters used to define the carving function were set to the values given in chapter 2 section 3.
- Transition in the streamwise direction : for $M_\infty \leq 7$ the critical Reynolds number was set to 15 million. For $M_\infty > 7$ the critical Reynolds number was calculated according to Sheetz's criteria. The user may choose to go back to Bowcutt's criteria if necessary.
- Surface emissivity : the surface emissivity of the waverider was assumed to be constant with temperature and set to a value of 0.8 for all surfaces.

The complete definition of each test case is summarized in Table 2 and 3.

Section 3 Discussion of the results

Waverider geometry

The waverider geometries are presented in figure 26 for the low dynamic pressure and in figure 27 for the high dynamic pressure. Due to the high values of the Reynolds number, both Mach 5 waveriders are similar to the caret wing which represents the optimum inviscid waverider. For a constant dynamic pressure trajectory, as the Mach number increases the Reynolds number decreases. Therefore, at higher Mach number, the geometry is less likely to resemble a caret wing. Note also, that the geometries

for Mach greater than 5 do not change very much; there is a reasonable amount of Mach number independence at high Mach number.

The principal dimensions are given in Table 4. As expected, for increasing Mach number and constant cone angle, the shock angle as well as the span will decrease. It is interesting to note that on both trajectories, the base height increases with Mach number. The effect of Mach number on the span and the base height results in an increase in volume efficiency with Mach number along a constant dynamic pressure trajectory. For Mach number less or equal than 10, the effect of altitude on the geometry is nonexistent : the two shapes are almost identical. For Mach greater or equal to 15, the effect of altitude on the geometry is small and acting only on the span of the vehicle.

Leading edge results

For a given geometry and a given carving law we can define a radius and a sweep angle distribution along the leading edge. These quantities, when combined with the freestream properties give us the ability to calculate the transition criteria $\bar{R}_*$ and the boundary layer characteristic length η. These four quantities are presented on figures 28a, 28b, 28c, 28d for the Mach 5, low dynamic pressure case. Figure 28e represents a flag function of the flow nature along the leading edge. When the flag is set to zero, the flow is laminar or has relaminarized. When the flag is set to 1, the flow is in a transitional or relaminarizing state. Finally, when the flag equals 2, the flow is fully turbulent. According to the values of $\bar{R}_*$ and η in this case, we see that the flow is purely laminar all along the attachment line of the leading edge. The next picture (fig.28f) describes the variation of the pressure gradient along the leading edge. This pressure gradient is calculated according to the modified Newtonian theory. Finally, figures 28g and 28h show the convective heat transfer (in megawatts/m^2) and the radiative equilibrium wall temperature distribution (in K)

along the leading edge. Figure 29 illustrates the same features for the high dynamic pressure case. As expected, due to a factor 5.6 increase in unit Reynolds number, $\bar{R}_*$ increases by a factor 2.4. The increase in unit Reynolds number produces the opposite effect on η which drops by more than a factor 2. As a result, we see that for almost identical radius and sweep distribution, the low dynamic pressure case presents a fully laminar leading edge and the high dynamic pressure case a fully turbulent one. This major difference leads to an increase of the radiative equilibrium wall temperature which is of the order of 50 K. Since we have chosen a leading edge made of carbon-carbon with a maximum temperature of 1900 K, the choice for a non active cooling option was justified for both cases. Looking to the values of η we can also justify the choice of a "rough" leading edge surface. For the low dynamic pressure, η is of the order of 0.15 mm and for the high dynamic pressure η is even smaller (0.06mm). We have previously defined our rough leading edge by the ratio $d/\eta > 2.4$. Therefore, at low/high dynamic pressure any obstacle larger than 0.36/0.14 mm along the attachment line would represent for the flow a major disturbance. These values justify a posteriori the choice of a "rough" leading edge.

If we now increase the Mach number to 10 (fig.30 and 31), the combination of larger radius along the leading edge and smaller unit Reynolds number produce $\bar{R}_*$ values which are slightly lower than for the Mach 5 case. In this case, we find the same situation at Mach 10 and at Mach 5. The flow is laminar/turbulent at low/high dynamic pressure. Due to the increase in the velocity, the heat transfer has substantially increased in both cases. At low dynamic pressure, the wall temperature now ranges from 1400 K to 1900 K. Due to the turbulent nature of the flow, at high dynamic pressure, the wall temperature rises a little bit and varies between 1600 K and 1900 K. Note that in both cases, active cooling becomes necessary but can be limited in a small region near the nose. The critical roughness size is now of the

order of 0.96/0.43 mm for the low/high dynamic case. The assumption of a rough leading edge is still reasonable at Mach 10.

At Mach 15 (fig.32 and 33), only the low dynamic case presents a fully laminar attachment line. At this point, the high dynamic pressure case requires active cooling all along the leading edge. The low dynamic pressure requires active cooling only in a small region near the nose. The average value of η continues to rise for both cases when compared to the Mach 5 and 10 cases. Here, with a critical roughness height of 1.6/0.8 mm for low/high dynamic pressure our assumption might not be totally valid anymore. Note that, at Mach 15 and 20, this is of no consequence at all. Assuming a smooth leading edge will only raise the critical value of $\bar{R}_*$ needed to provoke transition. The rough leading edge option has therefore to be seen as a worst case scenario.

Finally, at Mach 20, both leading edges are fully laminar and require active cooling all along the leading edge. At high dynamic pressure, the convective heat transfer is maximum at the nose and of the order of 9.5 MW/m^2. The radiative heat transfer at 1900 K is of the order of 0.6 MW/m^2. Therefore, the active cooling system should be able to absorb 8.9 MW/m^2. This value, for the chosen active cooling device, is well within the maximum heat transfer of 10.3 MW/m^2 admitted by the system. For the rest of the leading edge, the convective heat transfer is much lower and ranges between 1.0 and 2.0 MW/m^2.

Transition front and heat transfer characteristics on the waverider surfaces.

Once the flow nature is known along the attachment line, we have in fact our "initial flow properties" at the first point of each upper and lower streamlines. When the flow is turbulent along the attachment line we know that it will stay in that condition all along the streamline up to the trailing edge of the vehicle. When the

flow is laminar at the leading edge, it might undergo transition along the streamlines according to the value of the local Reynolds number.

The transition front on the upper and lower surface of the vehicle are given for our eight cases in figures 36 to 43. On each figure, the black surfaces are indicative of laminar region. When the flow is turbulent, the details of the grid are apparent. Due to their different way of construction, the upper and lower surfaces are different. The upper surface is always represented by a matrix of 51x51 points (some overlapping on the planform curve). On the other hand, the lower surface is represented by 51xK points, where K may be any number between 2 and 100. The value of K, which represents in fact the number of stations in the flow direction, varies according to the choice made by the optimization algorithm on the five initial points (see chapter 2 section 2 or reference 4 for more details). The lines oriented in the flow direction on the upper surface or with a small angle on the lower surface are the streamlines of the flow on both surfaces.

At Mach 5, and low dynamic pressure (fig.36) we know that the flow is laminar all along the leading edge. Meanwhile, the unit Reynolds number is so high that almost the entire surfaces are wetted by turbulent flow. At high dynamic pressure (fig.37), the flow is fully turbulent at the leading edge and as a consequence both surfaces are wetted by turbulent flow.

At Mach 10 and low dynamic pressure (fig.38) we can see that the laminar flow region is more important and representative of the combined favorable effect of decreasing the unit Reynolds number and increasing the Mach number. At high dynamic pressure (fig.39), the flow is still turbulent along the leading edge. In consequence, both surfaces are still wetted by turbulent flow except near the nose.

At Mach 15 and 20 (fig.40 to 43), the leading edges are laminar in all cases. Therefore, at a given Mach number we can compare the effect on the transition front

due to a change in unit Reynolds number. Or, at a given dynamic pressure, we can visualize again the combined favorable effect of decreasing the unit Reynolds number and increasing the Mach number. Note that at high dynamic pressure (fig.41 and 43), most of the lower surface is still wetted by turbulent flow. It is interesting to note that for the high dynamic pressure trajectory, most of the flow on the lower surface is turbulent from Mach 5 to Mach 20 (fig.37, 39, 41, 43). Now that the flow nature has been determined along each of the upper and lower streamlines we can evaluate the laminar and turbulent heat transfer characteristics along these lines. Since the high dynamic pressure trajectory always presents higher heat transfer we will focus on that particular one.

For each Mach number, the convective heat transfer on the upper and lower surface is presented along different streamlines (fig.44 to 47). The main purpose of these graphs is to give to the reader an order of magnitude of the convective heat transfer involved at each Mach number. Note also that the curves are numbered from 1 to 51. The curve number 1 is the centerline streamline and the curve number 51, represented by one point, is the wing tip. By joining the first point of each curve, we obtain the heat transfer distribution along the attachment line of the leading edge presented earlier. By choosing a given streamline, we can follow the evolution of the heat transfer as the flow travels from the leading edge to the trailing edge. The Mach 15 case is rather interesting (fig.46) since it illustrates fairly well on the upper surface the effect of sweep angle on the critical Reynolds number as explained in chapter 3, section 2, topic 2. Since the heat transfer is always higher on the lower surface, the next set of figures (48 to 51) presents the wall temperature distribution only on the lower surface. To allow more details, the span has been artificially expanded here. The main purpose of these graphs is to determine what kind of thermal protection is needed and if eventually active cooling would be required in certain zones.

Obviously, at Mach 5 (fig.48), most of the surface is at a wall temperature of 800–900 K.

At Mach 10 (fig.49), the range is of the order of 1100–1400 K.

At Mach 15 (fig.50), small region situated near the leading edge have a temperature higher than 1800 K but none of them actually reached 1900 K. For this case, the temperature on the surface ranges from 1400 to 1700 K.

At Mach 20 (fig.51), the situation is somewhat different. A thin region of laminar flow exists near the leading edge and the temperature drops in this region. But transition takes rapidly place after that region and the temperature rises above 1800 K.

The thermal protection proposed in chapter 3 section 6 seems to be sufficient to protect the lower waverider surface. Moreover, even in the most severe conditions, active cooling was not found to be necessary if a carbon-carbon protection can be expanded somewhat downstream of the leading edge.

Finally, a last set of figures (52 to 55) presents the convective heat transfer and the wall temperature distribution along the trailing edge of the upper and lower surface of the vehicle. The main purpose here is to illustrate the difference in wall temperature on the upper and lower surfaces as well as the large temperature gradient from one streamline to the other. These large temperature gradients will result in heat transfer by conduction through the structure that will have to be managed by an appropriate disposition of heat sinks in the structure.

Waverider performance

The conventional viscous-optimized waveriders with a sharp leading edge, produce high L/D values. Question : Does the finite leading edge bluntness greatly affect the lift-to-drag ratio ?

Looking at Table 6, we see that the leading edge pressure drag remains a small fraction of the inviscid drag. Note that for the 8 cases presented, the leading edge drag represents 4 to 8% of the inviscid drag. Therefore, we can conclude that for the given carving law defined in chapter 2 section 3, the leading edge drag will represent a small but non-negligible fraction of the inviscid drag of the waverider. Note that Navier-Stokes calculations performed on blunted waveriders[6] have shown similar results in terms of the leading edge drag. Since the waverider considered presents similar geometry at a given Mach number, very small differences are observed in the inviscid drag and in the inviscid value of L/D. On the other hand, due to their differences in Reynolds number the viscous drag at a given Mach number is more affected. Although the high dynamic pressure is five times larger than the lower dynamic pressure, the unit Reynolds number based on the freestream conditions is more than five time larger at high dynamic pressure. Since the skin friction is inversely proportional to some function of the local Reynolds number, the viscous drag will be smaller at high dynamic pressure. At low dynamic pressure, the viscous drag decreases with increasing Mach number due to a progressive laminarisation of the vehicle surface. At high dynamic pressure, the viscous drag seems to be constant with Mach number. In fact, at Mach 5 and 10, the leading edge is fully turbulent and in both cases the waverider is wetted by turbulent flow. At Mach 15 and 20, the leading edge is laminar but the local Reynolds number is still so high that most of the waverider surface is wetted by turbulent flow.

Comparing the pressure drag and the viscous drag, we see that the pressure drag is always higher than the viscous drag. Bowcutt[2] and Corda[3] demonstrated that the highest L/D value is always obtained when the pressure drag and the viscous drag are approximately equal. This suggests that higher L/D values could be obtained for smaller cone angle in the 8 cases treated here. Nevertheless, when compared

to the best optimum in L/D obtained by Bowcutt[2] and Corda[3] (fig.56) we see that the present values are generally lower except for Mach 5, high dynamic pressure where the L/D obtained here is slightly higher than the new L/D "barrier" defined by Bowcutt[2]. At low dynamic pressure, where the entire leading edge was laminar from Mach 5 to Mach 20, the variation of L/D with Mach number (Table 6) presents a local minimum at Mach 15 similar to the results of Bowcutt[2] and Corda[3] (fig.56). At high dynamic pressure, this local minimum is not observed but the Reynolds numbers are not comparable.

Waverider optimized for volume

All the previous test cases discussed up to here have been optimized in order to maximize L/D. They all present the same type of triangular planform shape with an almost constant sweep angle from the second to the last point of the leading edge. If another objective function is chosen for the optimization algorithm, for instance waverider volume, the code comes out with a totally different planform shape. The test case at Mach 20 and high dynamic pressure was run with volume as the objective function. The leading edge results and the planform shape are given in figure 57 and 58. As we see, a major difference appears in the sweep angle distribution. The sweep angle is no longer nearly constant but gradually increases along the leading edge. This has a major impact on the variation of $\bar{R}_*$. As a consequence, transition is now predicted near the nose and relaminarization is occurring later when $\bar{R}_*$ drops below 250 (see chapter 3, section 2, topic1). Since turbulent flow is present along a large part of the leading edge, a relatively large portion of the upper surface will now be wetted by turbulent flow as opposed to the waverider optimized for L/D for the same flight condition which has a fully laminar upper surface. Even more surprising, for the same kind of planform shape, at low dynamic pressure the flow will be turbulent along the leading edge for the Mach 5 and Mach 10 cases. Therefore,

due simply to a change of planform shape, our previous observation about the nature of the flow for the L/D optimized waverider is totally reversed. In the case of the waveriders optimized for volume, only two test cases (Mach 15 and 20, low dynamic pressure) would present a fully laminar leading edge. This major difference will have an negative impact on the performance of the volume optimized waveriders. When compared to the maximum L/D (Table 7), the volume optimized waveriders , show a moderate decrease in L/D ranging from 8 to 15%. On the other hand, they show an increase in volume of the order of 60 to 350%. From the heat transfer point of view, the volume optimized cases present a higher average heat transfer rate due to smaller sweep angle and the turbulent nature of the flow (compare fig.35 and 37).

Finally, due to the continuous increase of sweep angle along the leading edge, a favorable pressure gradient exists along the leading edge. As a consequence, the assumption of an infinite swept cylinder with no pressure gradient along the attachment line might not be even true locally anymore. What is the impact of a favorable pressure gradient on the stability of a 3D boundary layer at hypersonic speed ? The problem was partially studied by Zurigat and al.[22]. They concluded that the effect of pressure gradients on stabilizing three-dimensional first-mode waves is much larger than its effect on stabilizing two-dimensional first mode waves. But we know that at hypersonic speed, the second-mode waves are dominant. They also demonstrated that the effectiveness of the pressure gradient on the natural laminar flow control of 2D second-mode waves decreases at hypersonic speed but nothing is said about the effects of pressure gradients on a 3D second-mode waves. This problem is apparently not well understood[23] and our question will remain without answer for the present time. By lack of any useful information on favorable pressure gradient and a better model for our swept leading edge we will continue to locally assume an infinitely swept cylinder with no pressure gradient.

Chapter 5 Conclusions and recommendations

The results of the present study lead to a number of important conclusions regarding the transition process along the attachment line of the leading edge and the heat transfer characteristc of a hypersonic waverider.

Section 1 Conclusions

A summary of the major results discussed in the previous chapter are itemized below :

- Geometry :
  - It is possible on a 60 meter waverider to successfully carve a radius distribution along the leading edge without strongly affecting the planform shape. The radii obtained are sufficient to implement an active cooling device.
- Transition at the attachment line of the leading edge :
  - for the L/D optimized waveriders, the flow was found to be laminar in all cases except at $M_\infty \leq 10$ at high dynamic pressure.
  - for the volume optimized waveriders, the flow was found to be turbulent in all cases except at $M_\infty \geq 15$ at low dynamic pressure.
- Cooling requirements and thermal protection system :
  - for a maximum wall temperature of 1900 K and a minimum radius of 1 mm, active cooling is not required at Mach 5 for the altitudes considered.
  - for a maximum wall temperature of 1900 K and a minimum radius of 10 mm, active cooling will be required for $M_\infty \geq 10$
  - In the worst conditions (Mach 20, high dynamic pressure), the active cooling device proposed for the leading edge was always working within its cooling capabilities.

- In the worst conditions (Mach 20, high dynamic pressure) and for a cone angle of 7.5 degree , a ceramic composites thermal protection system is sufficient for the lower surface and no active cooling should be necessary.

  For a larger cone angle this might not be true.

- Performance :
  - The inviscid drag due to the leading edge was found to be a small but non-negligible (4 to 8%) fraction of the inviscid drag.
  - Although the viscous drag at the leading edge can be neglected, the presence of the leading edge will greatly influence the transition front of the upper and lower surface and therefore affect the viscous drag of the entire vehicle.
  - When optimized for L/D, the performance obtained in this study are within the two L/D barriers defined by Bowcutt for similar flight conditions.
  - When optimized for volume, the geometry and the transition pattern are radically different than the waverider optimized for L/D. The decrease in L/D ranges from 8 to 15 % for an increase of 60 to 350 % in volume.

Section 2 Recommendations for further study

This study has always assumed that the flow was in a calorically perfect state at the wall. For a maximum wall temperature of 1900 K and a fully catalytic wall, this assumption is perfectly valid in a region of high pressure. In the low pressure regions this assumption is questionable since we know that low pressure will enhance dissociation. Therefore, it might be interesting to consider a study where pressure and temperature at the wall would be used to determine the amount of dissociated oxygen present on the vehicle surface.

In another category, if we look to the geometry of the waverider optimized for L/D or maximized for volume both have to be considered as unrealistic. The first

ones for an evident lack of volume and the second ones for a bad distribution of this volume. The optimization algorithm creates high volume by keeping the base thickness almost constant and by increasing the span as much as it can. This results in a very flat waverider with large span. These configurations are probably useless because the structure needed to support this large span would be very heavy. An easy way to produce useful volume is to calculate the moment of inertia of a cross section from the symmetry plane. The moment of inertia of a cross section could be calculated at different stations along the waverider and averaged. The averaged moment of inertia has the dimension of m^3 and can be used to non dimensionalize the volume. If the following objective function is chosen :

$$\frac{L}{D} * \left(\frac{Volume}{M_{Inertia}} \right)^n \tag{90}$$

we should obtain vehicles with good values of L/D and a optimum distribution of this volume. L/D or the volume distribution could eventually be stressed according to the value of n.

Finally, the present study does not show any results for a 10 meter waverider. For a vehicle of that size and the carving law defined by equation (1), it is not possible to implement everywhere along the leading edge the minimum radius of 10 mm required by the active cooling device. By increasing the generating cone angle, a larger deflection of the streamlines can be obtained as well as larger values of the radii. But, due to the increased deflection of the streamlines, the performance of these kind of vehicles drops considerably and the wall temperature on the lower surface is much higher than the maximum temperature allowed by the thermal protection. Therefore, vehicles of that size will require another type of active cooling at the leading edge allowing smaller values of the leading edge radii and higher cooling performance.

Appendix A Tables

Test cases	M_∞	Q_∞ (atm)	Altitude (km)	$Rey_\infty * 10^{-6}$ (1/m)	V_∞(m/s)
1	5	0.196	30.4	1.625	1529
2	10	0.199	40.4	0.738	3243
3	15	0.203	46.8	0.458	5047
4	20	0.206	51.5	0.347	6744
5	5	0.998	19.8	9.383	1475
6	10	0.990	28.8	4.375	3024
7	15	0.998	34.4	2.691	4699
8	20	1.007	38.6	1.914	6423

Table 1 Flight conditions

Test cases	M_∞	Q_∞ (atm)	Cone $\triangleleft$	L(m)	γ	Rough	Cooling	Max T (K)	Max Box	Min Slr
1	5	0.2	7.5	60	1.4	Yes	No	1900	0.4	.075
2	10	0.2	7.5	60	1.4	Yes	Yes	1900	0.4	.075
3	15	0.2	7.5	60	1.4	Yes	Yes	1900	0.4	.075
4	20	0.2	7.5	60	1.4	Yes	Yes	1900	0.4	.075
5	5	1.0	7.5	60	1.4	Yes	No	1900	0.4	.075
6	10	1.0	7.5	60	1.4	Yes	Yes	1900	0.4	.075
7	15	1.0	7.5	60	1.4	Yes	Yes	1900	0.4	.075
8	20	1.0	7.5	60	1.4	Yes	Yes	1900	0.4	.075

Table 2 Input data files options

Test cases	Surface emissivity	Minimum Radius	Rey_{Crit}	C(0)	C(1)	m
1	0.8	1 mm	15.10^6	2%	50%	0.9
2	0.8	1 0 mm	Sheetz	2%	50%	0.9
3	0.8	1 0 mm	Sheetz	2%	50%	0.9
4	0.8	1 0 mm	Sheetz	2%	50%	0.9
5	0.8	1 mm	15.10^6	2%	50%	0.9
6	0.8	1 0 mm	Sheetz	2%	50%	0.9
7	0.8	1 0 mm	Sheetz	2%	50%	0.9
8	0.8	1 0 mm	Sheetz	2%	50%	0.9

Table 3 Code options

Test cases	Shock $\triangleleft$	Base/L	Box	Volume (m^3)	Veff
1	13.7	0.077	0.34	1669	0.105
2	9.9	0.106	0.22	1845	0.170
3	9.0	0.116	0.19	1685	0.193
4	8.7	0.119	0.19	1850	0.200
5	13.7	0.075	0.35	1685	0.103
6	9.9	0.105	0.23	1931	0.169
7	9.0	0.117	0.15	1389	0.207
8	8.7	0.120	0.13	1093	0.228

Table 4 Waverider dimensions, L/D optimized

Test cases	$\bar{R}_*$ max	η max (mm)	$\dot{q}_w$ max (kW/m^2)	T_w max (K)	(%) of turbulent flow	(%) of cooling
1	272	0.159	73.1	1127.1	0.0	0.0
2	223	0.451	842.9	1900.0	0.0	0.1
3	154	0.701	2314.1	1900.0	0.0	3.3
4	118	0.873	5067.4	1900.0	0.0	100.0
5	623	0.067	84.1	1167.3	92.0	0.0
6	538	0.185	1500.2	1900.0	91.0	0.6
7	304	0.290	5233.8	1900.0	0.0	100.0
8	250	0.436	9545.7	1900.0	0.0	100.0

Table 5 Leading edge results, L/D optimized

Test cases	Cd_{le} $*10^3$	Cd_p $*10^3$	L/D invisc	Cd_{visc} $*10^3$	$Cd_{tot.}$ $*10^3$	L/D
1	0.19	2.6	13.5	2.1	4.7	7.4
2	0.24	4.0	8.7	2.0	6.0	5.8
3	0.27	4.5	7.8	1.6	6.1	5.7
4	0.23	4.6	7.5	1.4	6.0	5.8
5	0.20	2.5	13.7	1.4	3.9	8.7
6	0.26	4.0	8.7	1.4	5.4	6.4
7	0.19	4.5	7.9	1.4	5.9	6.0
8	0.25	4.6	7.6	1.4	5.9	5.9

Table 6 Waverider performances, L/D optimized

Tests cases	L/D optimised	Volume (m^3)	L/D	Volume optimised (m^3)	ΔL/D (%)	ΔVol (%)
5	8.7	1685	8.0	2763	-8.0	64.0
6	6.4	1932	5.7	4341	-10.9	124.8
7	6.0	1388	5.1	5271	-15.0	279.8
8	5.9	1093	5.0	5089	-15.3	356.6

Table 7 Comparison of waverider optimized for L/D and optimized for Volume

Appendix B Figures

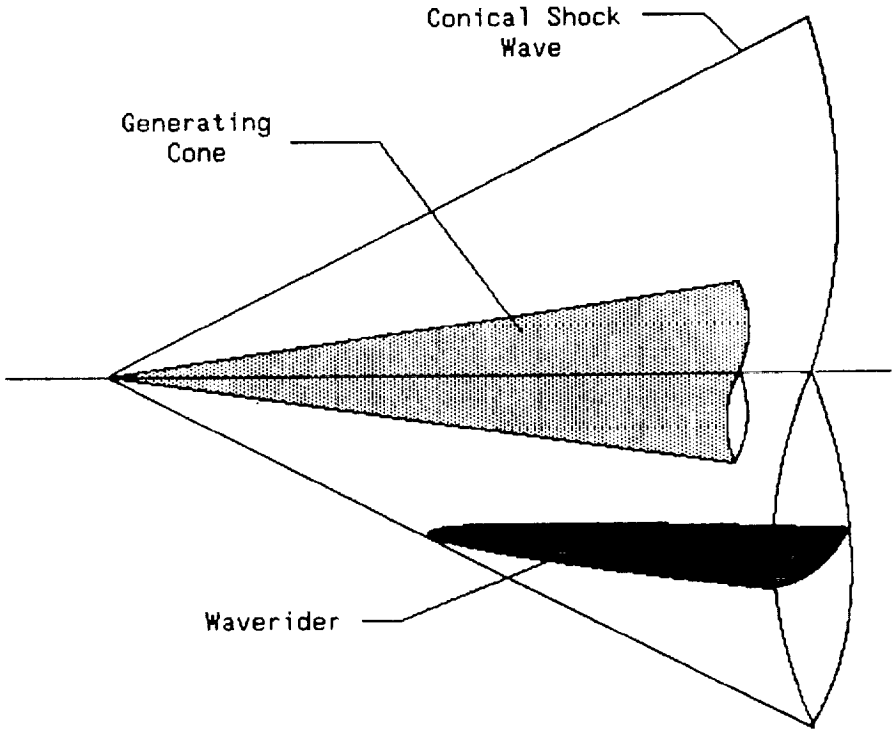

Figure 1 Conically derived waverider (from reference 4)

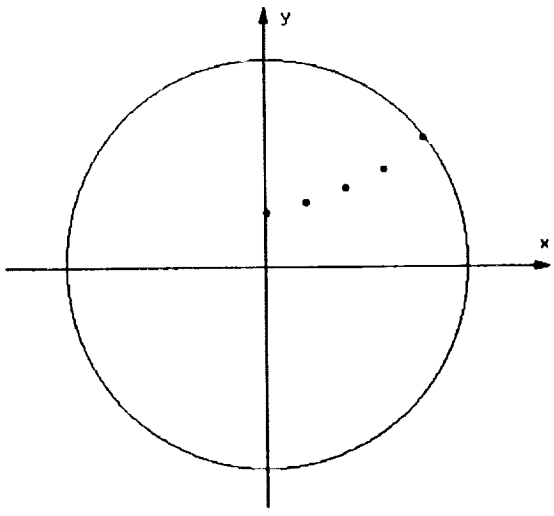

Figure 2 Illustration of five original leading edge points for a typical case (from reference 4)

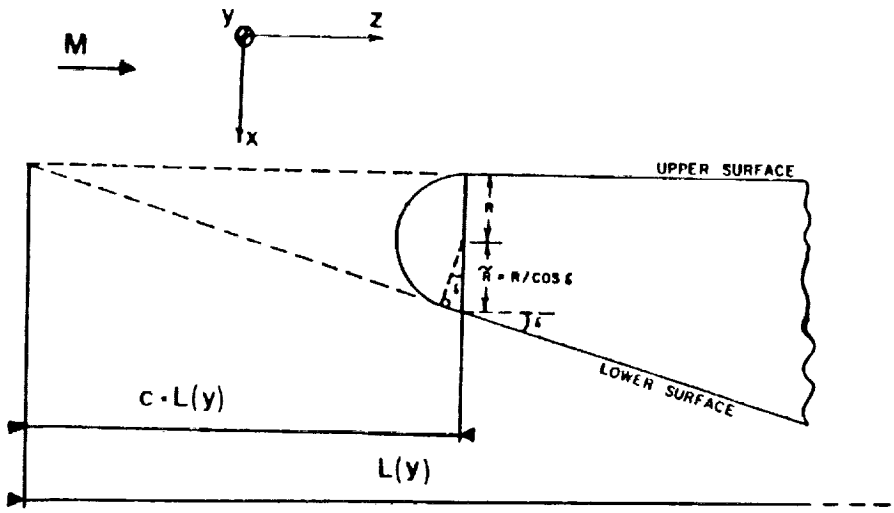

Figure 3 Leading edge carving to accommodate bluntness

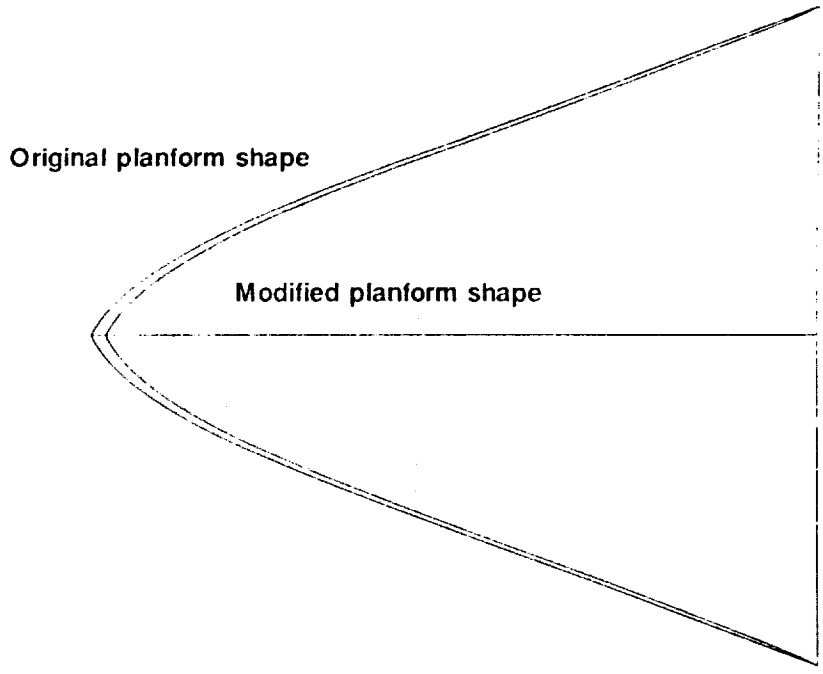

Figure 4 Comparison of the original and the modified planform after carving

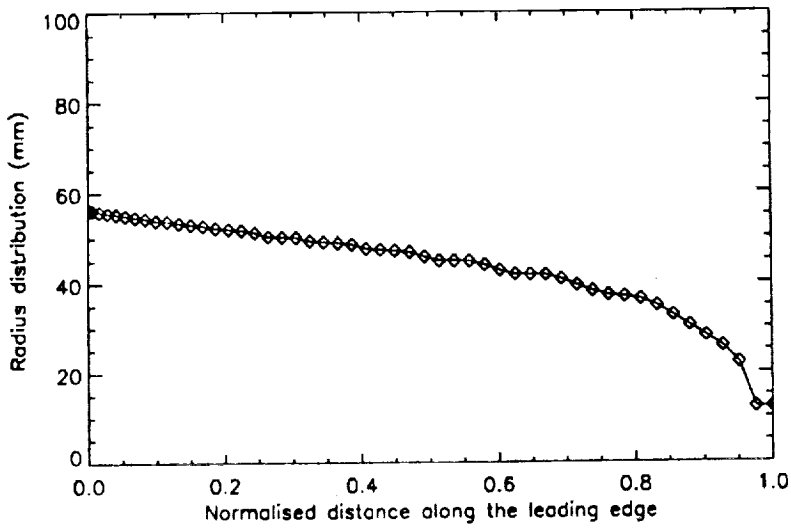

Figure 5 Typical radius distribution along the leading edge

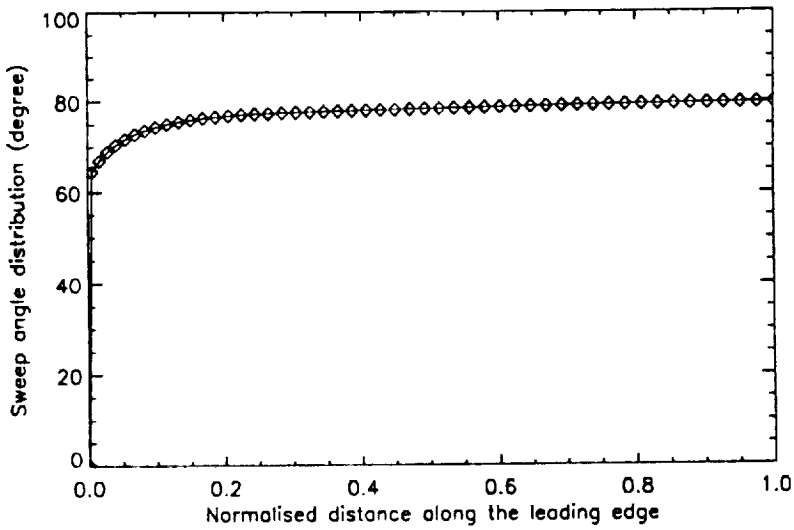

Figure 6 Typical sweep angle distribution along the leading edge

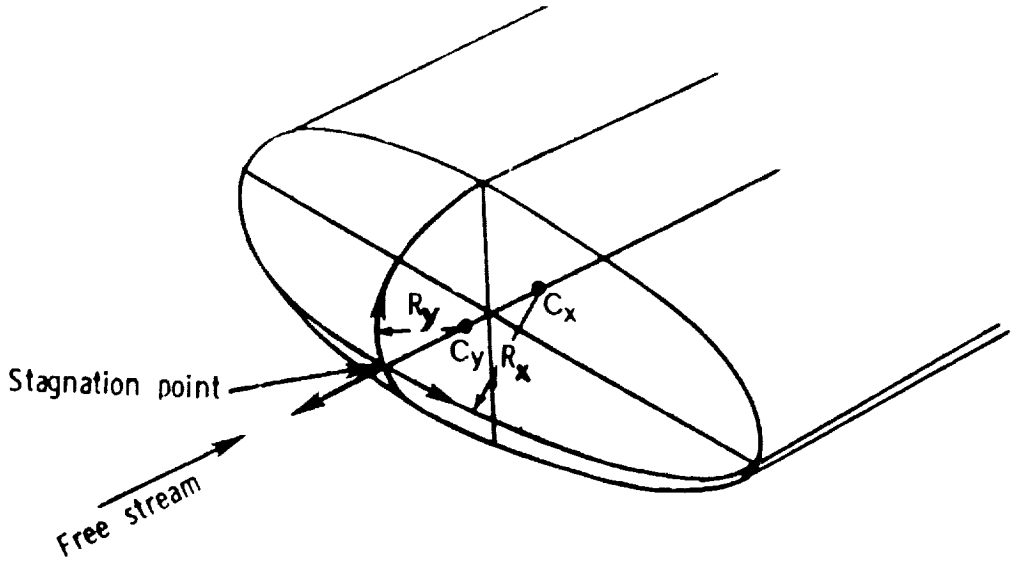

Figure 7 3D stagnation point region (from reference 18)

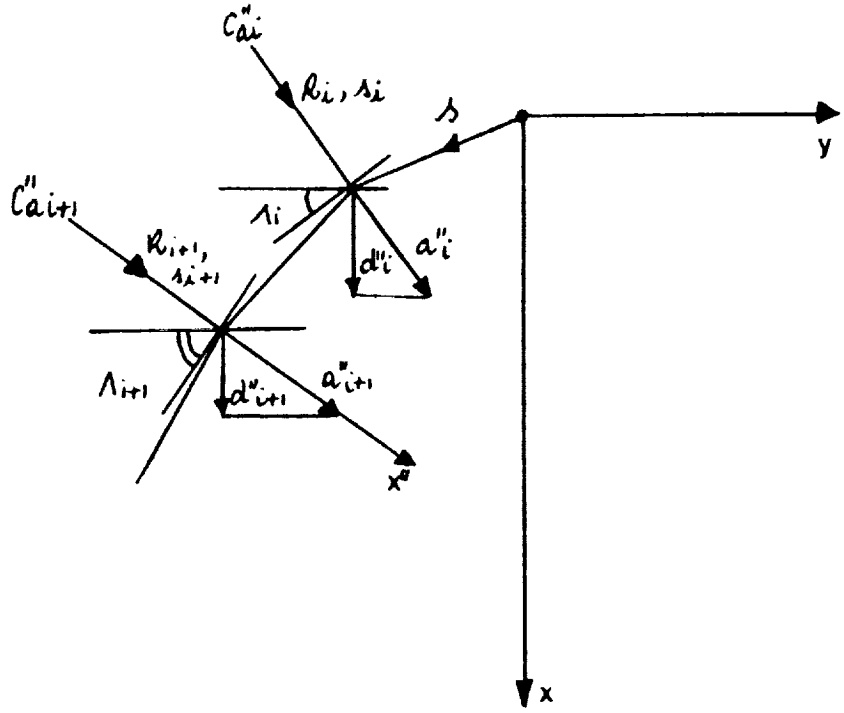

Figure 8 Leading edge force diagram and geometry

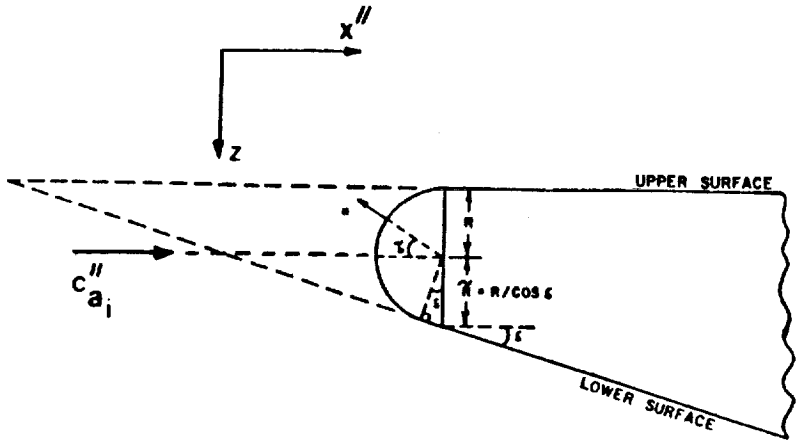

Figure 9 Normal cross section to the leading edge used for pressure integration

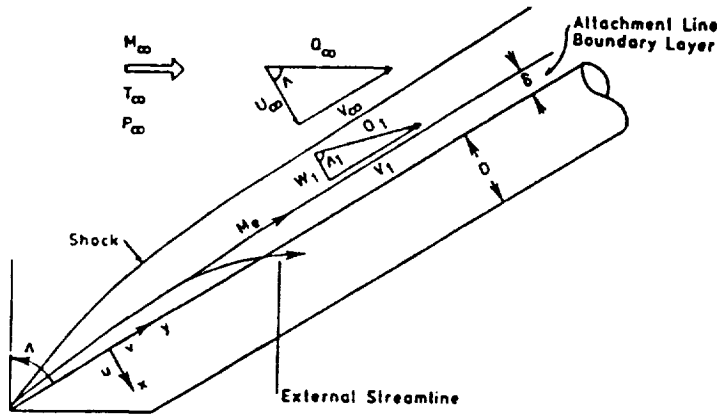

Figure 10 The infinite swept cylinder

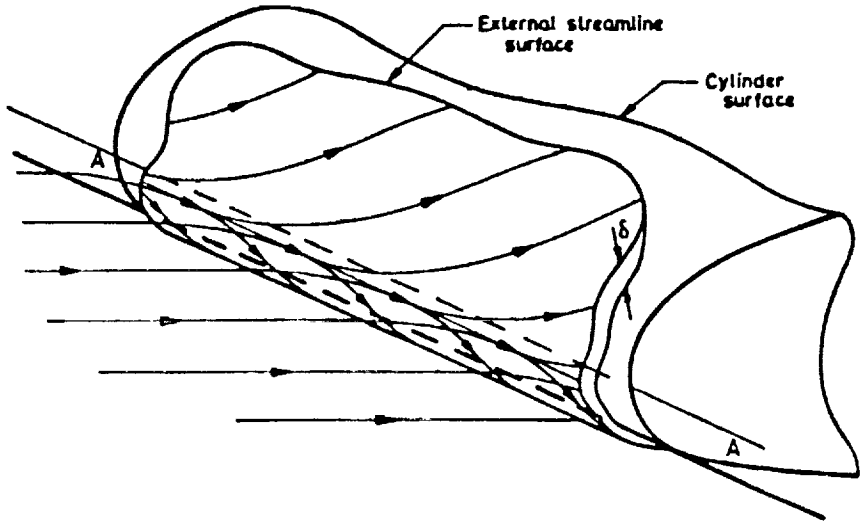

Figure 11 Flow near the leading edge of a swept cylinder (from reference 11)

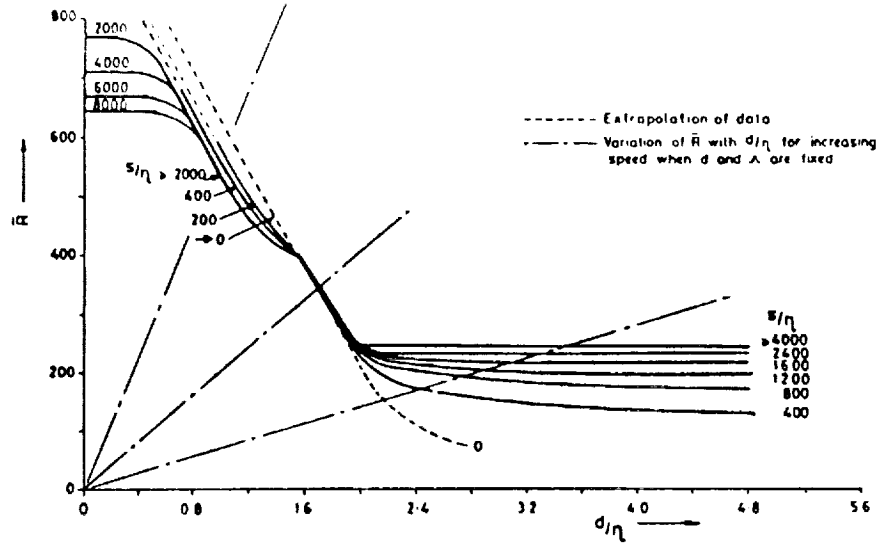

Figure 12 The variation of $\bar{R}_*$ *with* d/η *and* s/η for the appearance of first bursts of turbulence (from reference 12)

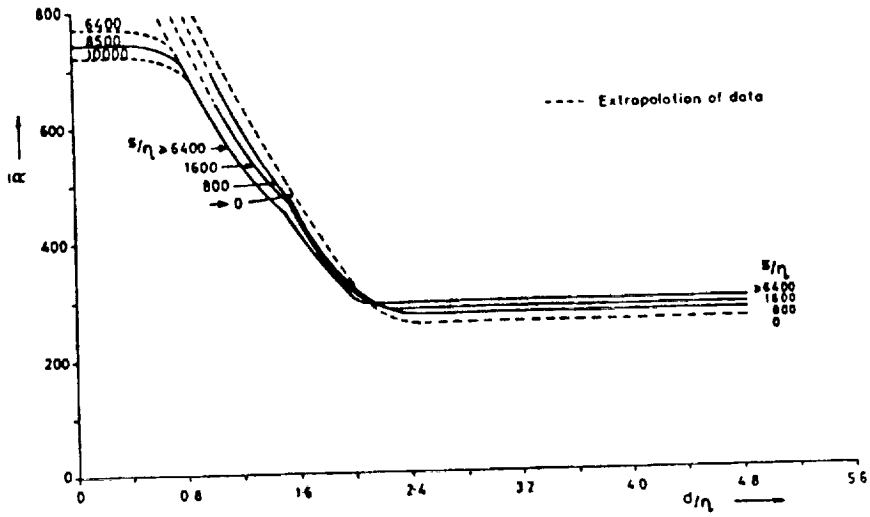

Figure 13 The variation of $\bar{R}_*$ *with* d/η *and* s/η for the completion of turbulence (from reference 12)

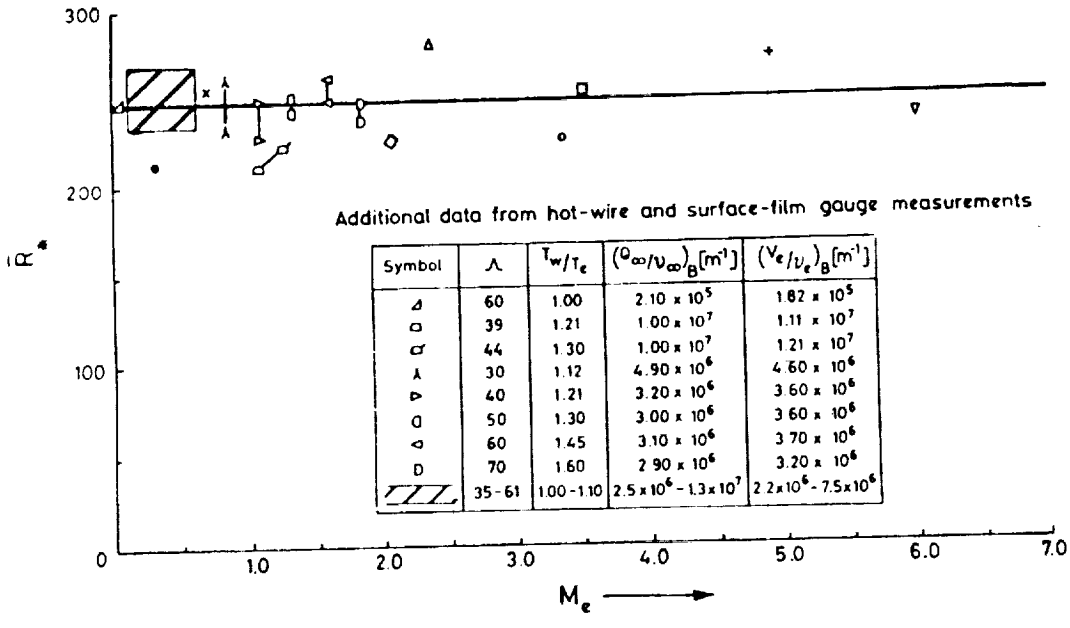

Figure 14 The variation of $\bar{R}_*$ at the onset of transition with edge Mach number and wall temperature (from reference 13)

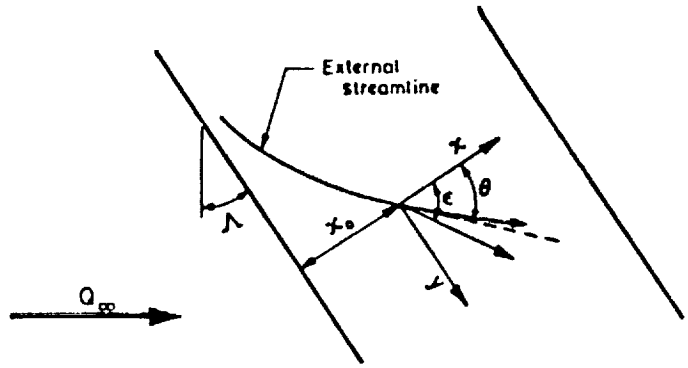

Figure 15 Co-ordinate system to investigate the instability of a three dimensional boundary layer (from reference 11)

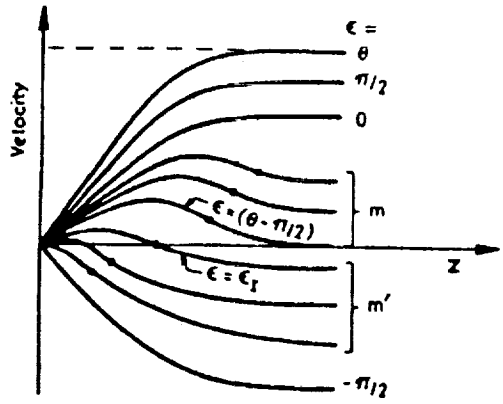

Figure 16 Variation of the velocity profile with the disturbance propagation angle (from reference 11)

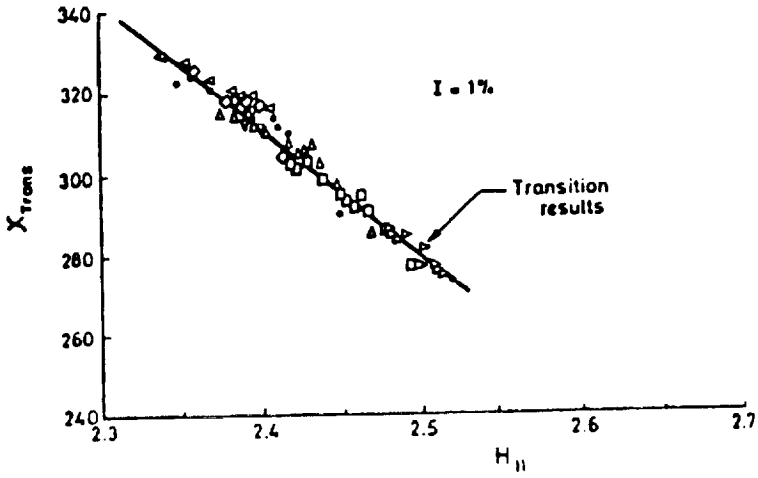

Figure 17 Variation of the cross-flow Reynolds number at transition onset with streamwise shape factor (from reference 11)

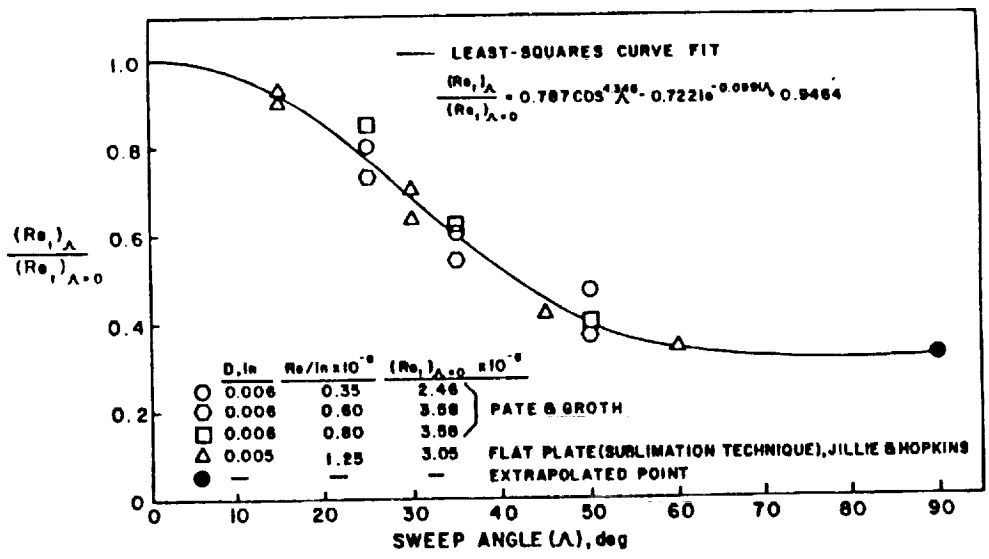

Figure 18 Effect of sweep angle on the normalized transition Reynolds number (from reference 2)

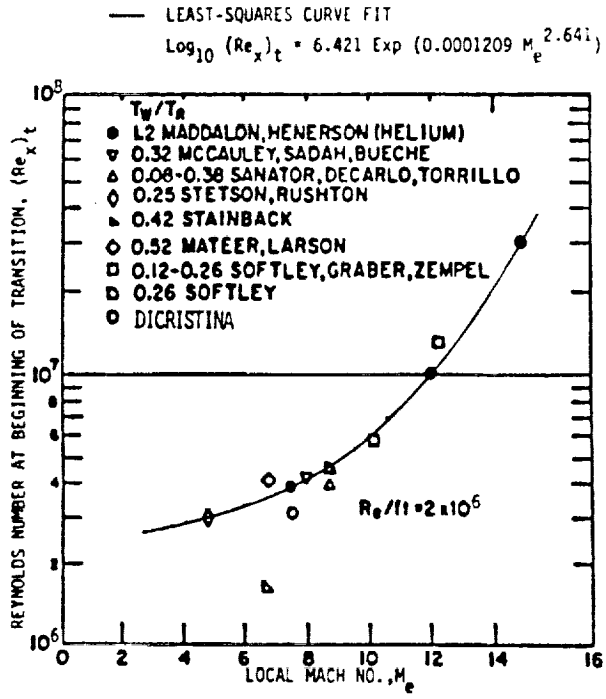

Figure 19 Correlation of transition Reynolds number with Mach number (from reference 2)

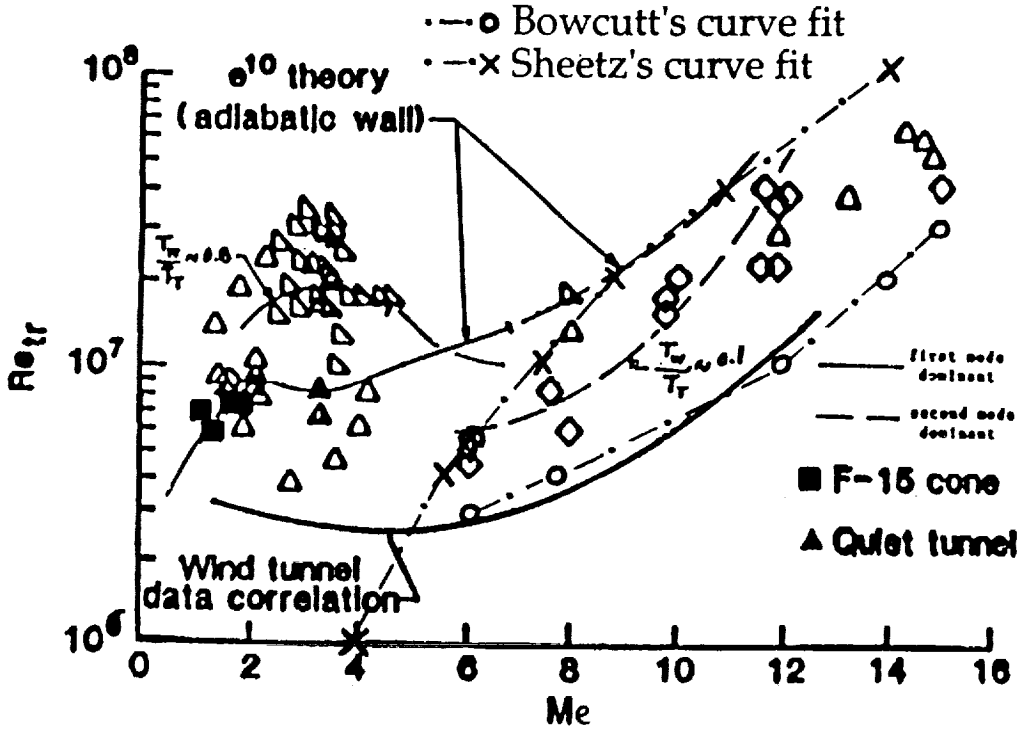

Figure 20 Comparison of predicted and observed transition Reynolds numbers on sharp cones (from reference 16)

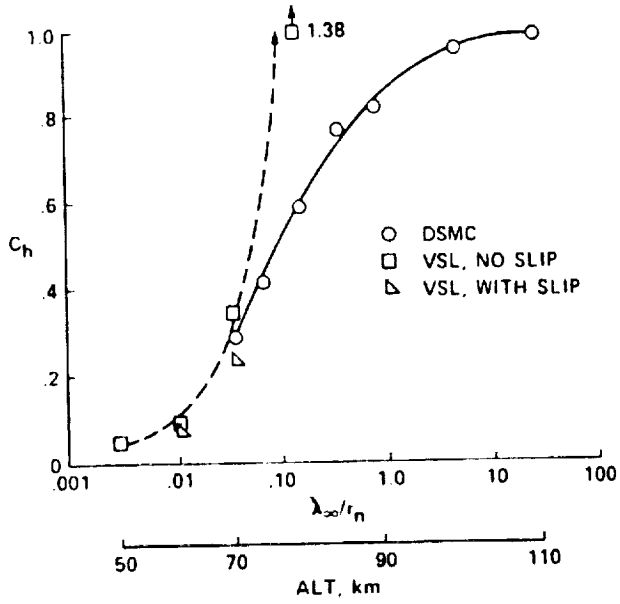

Figure 21 Stagnation point heat transfer coefficient versus Knudsen number. $V_\infty = 7.5\ km/s$, $R_n = 1\ inch$ (from reference 17)

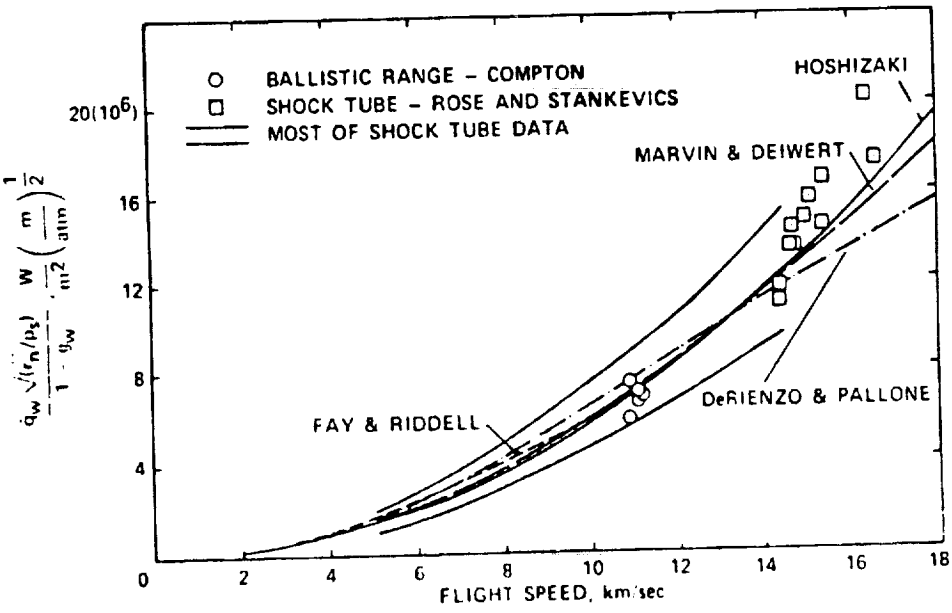

Figure 22 Stagnation point convective heating comparisons (from reference 17)

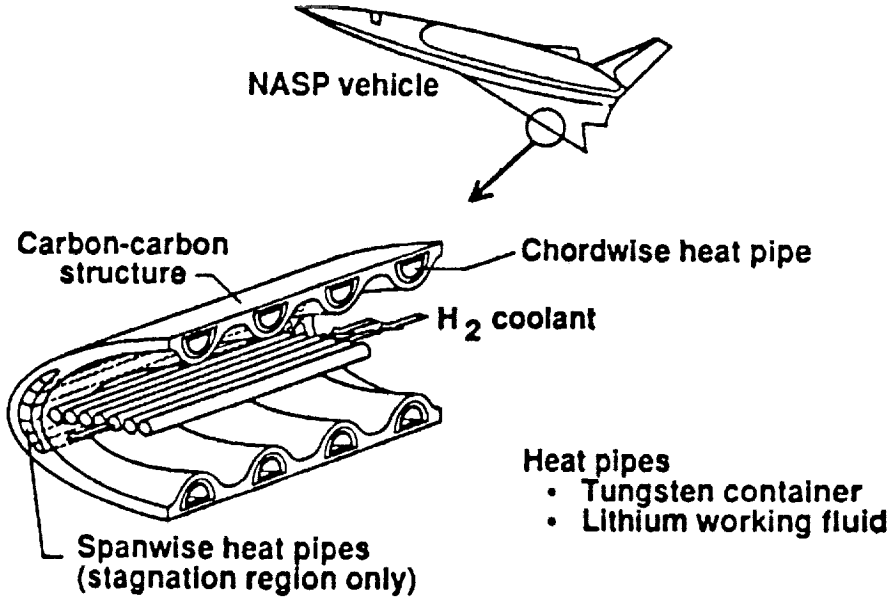

Figure 23 Carbon-carbon / refractory metal heat-pipe concept for a wing leading edge (from reference 20)

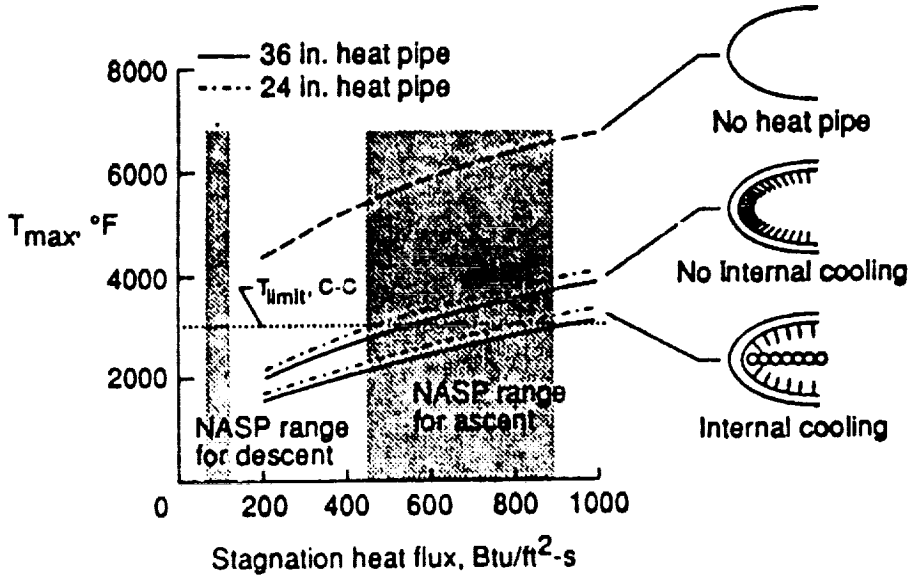

Figure 24 Performance of leading edge cooling device (from reference 20)

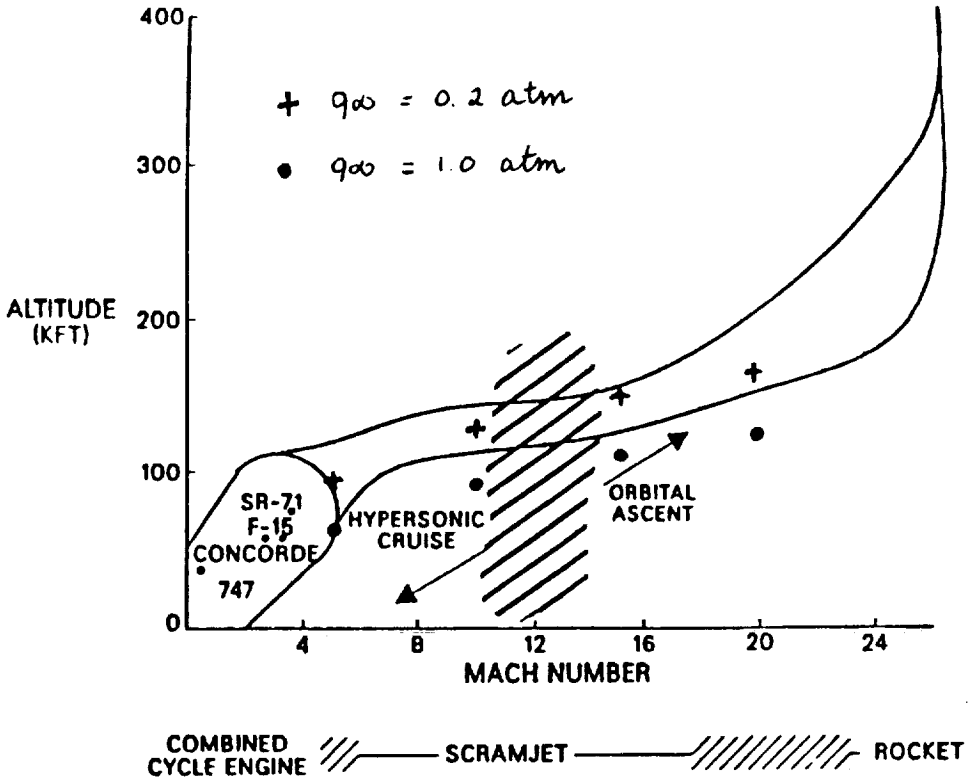

Figure 25 Constant dynamic pressure trajectories

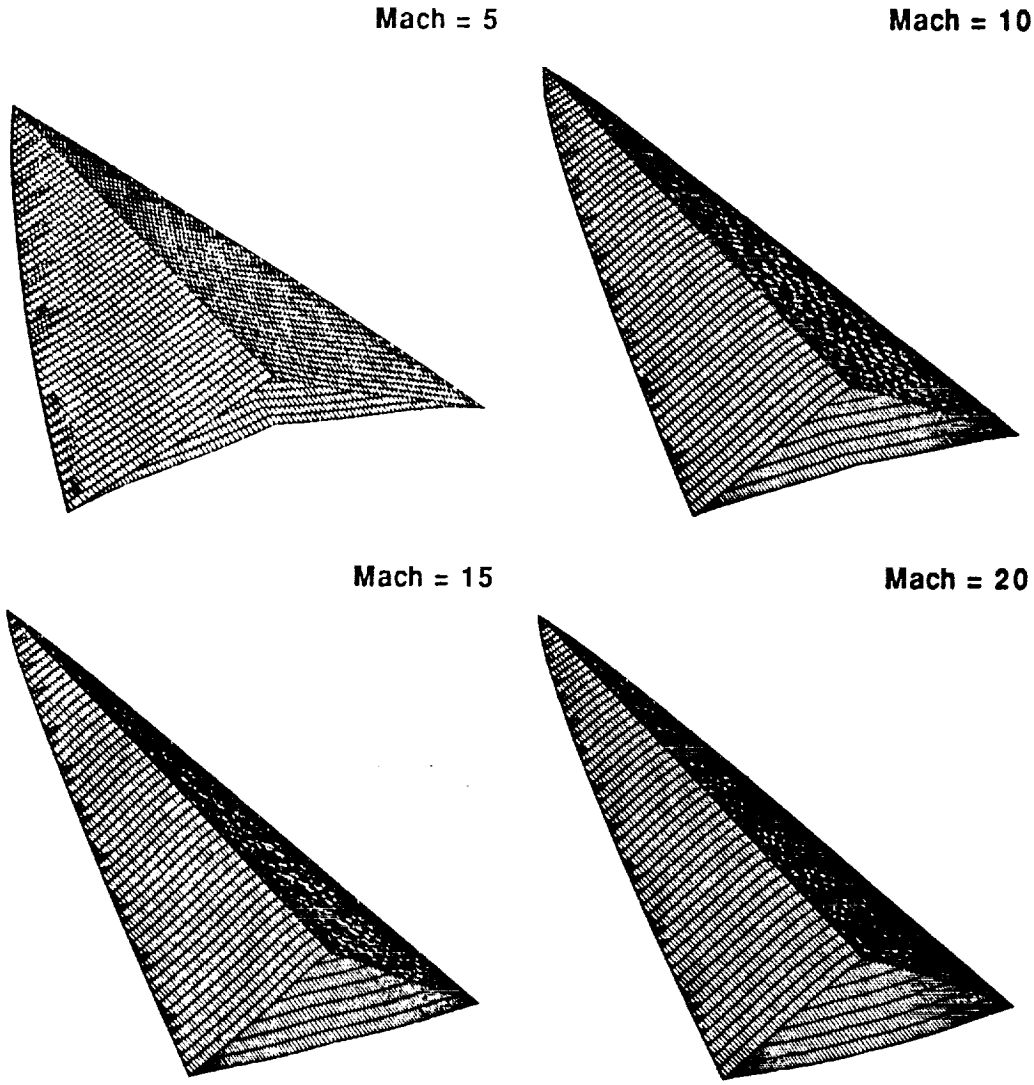

Figure 26 Waveriders optimized for L/D, $Q_\infty = 0.2$ *atm*.

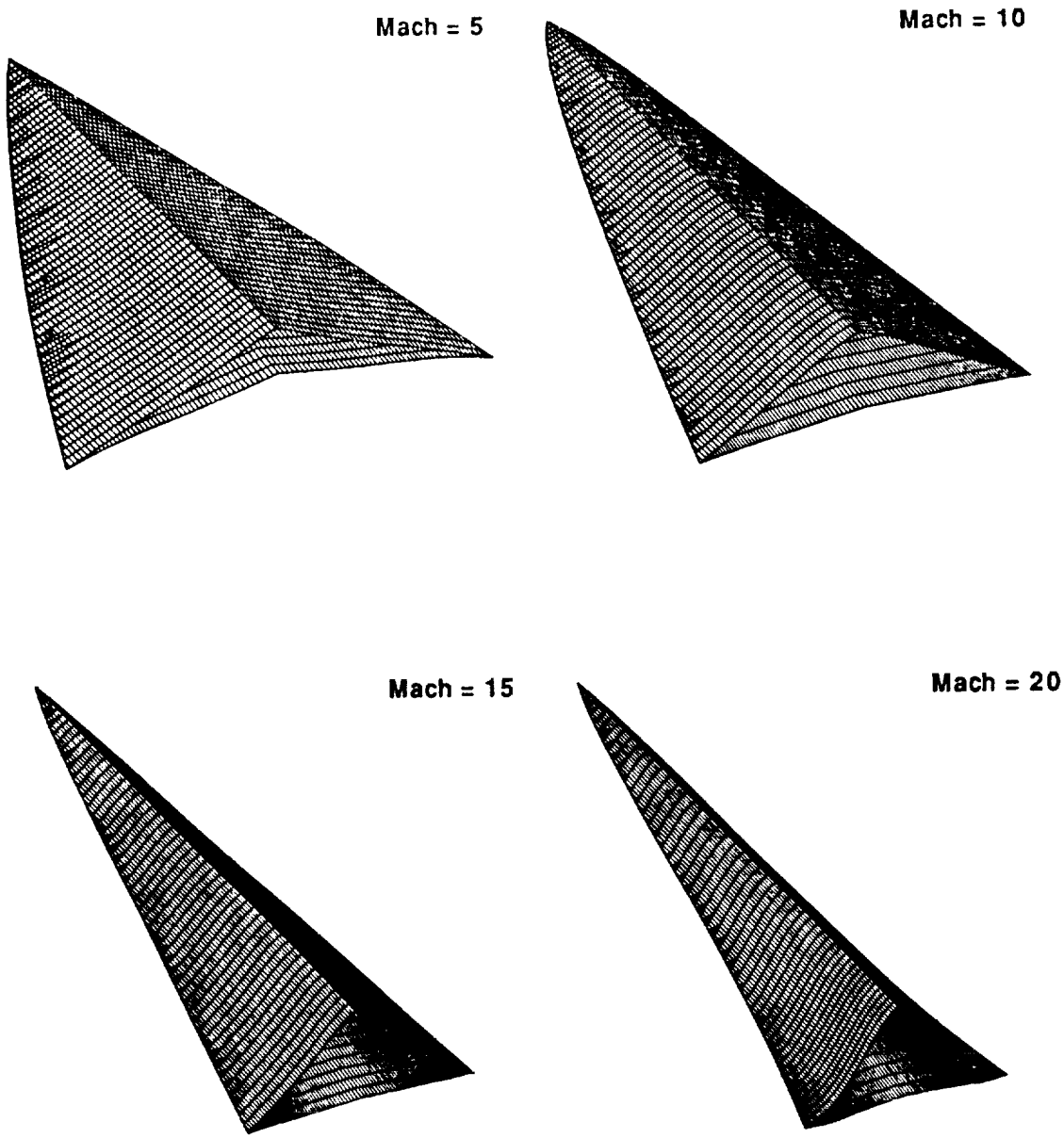

Figure 27 Waveriders optimized for L/D, $Q_\infty = 1.0\ atm$.

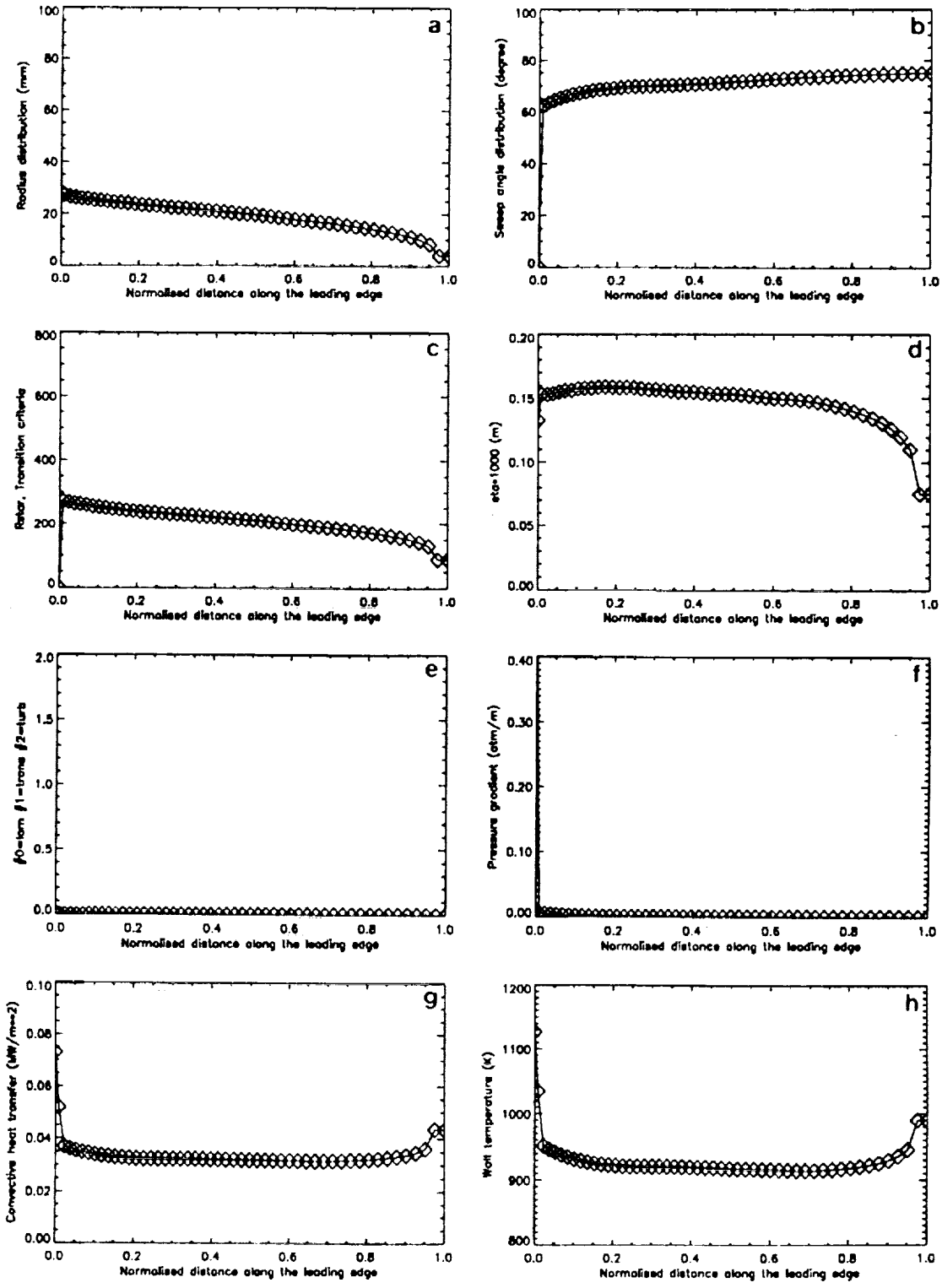

Figure 28 Leading edge results, L/D optimized, $M_\infty = 5$, $Q_\infty = 0.2$ atm.

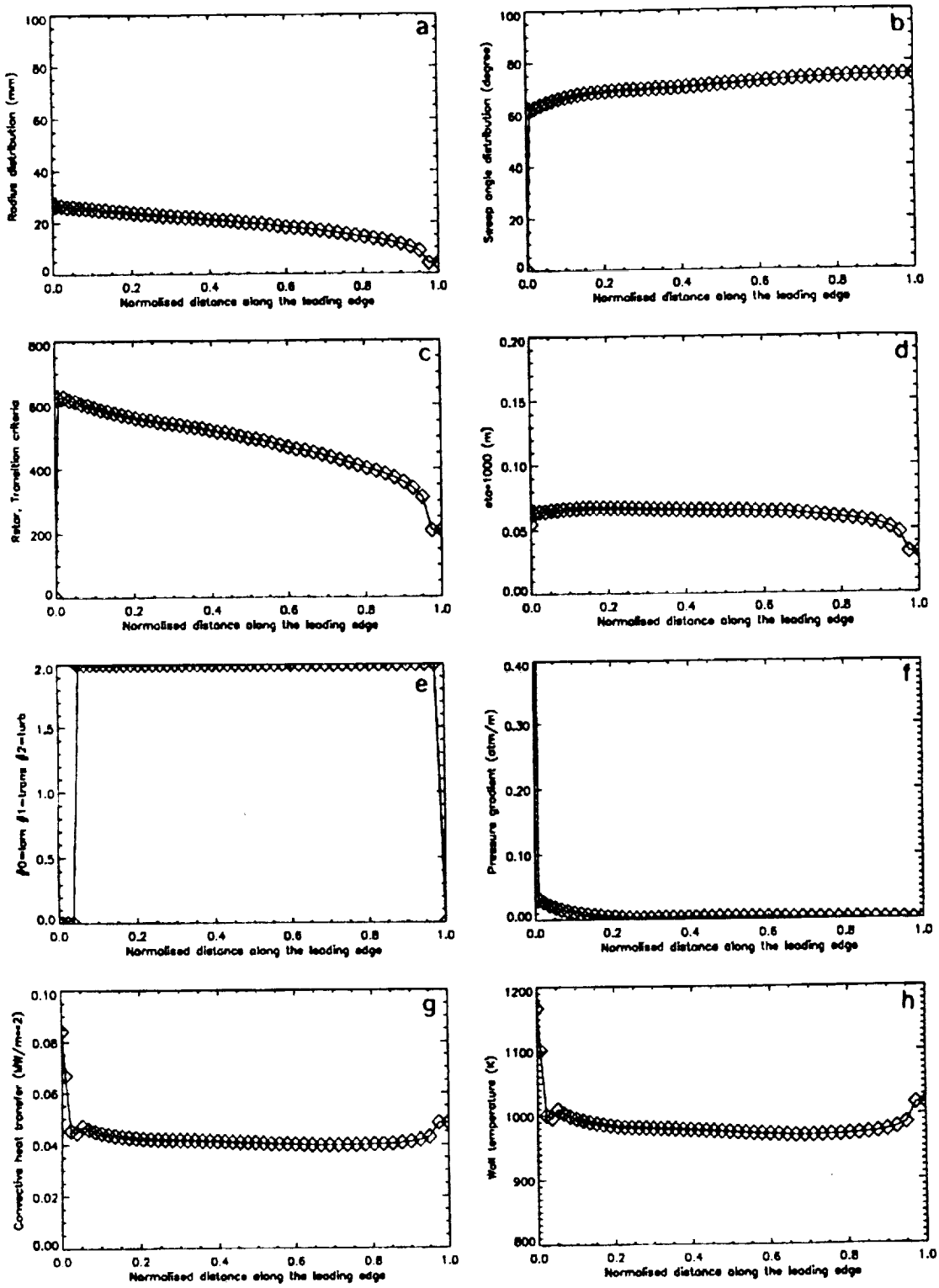

Figure 29 Leading edge results, L/D optimized, $M_\infty = 5$, $Q_\infty = 1.0$ atm.

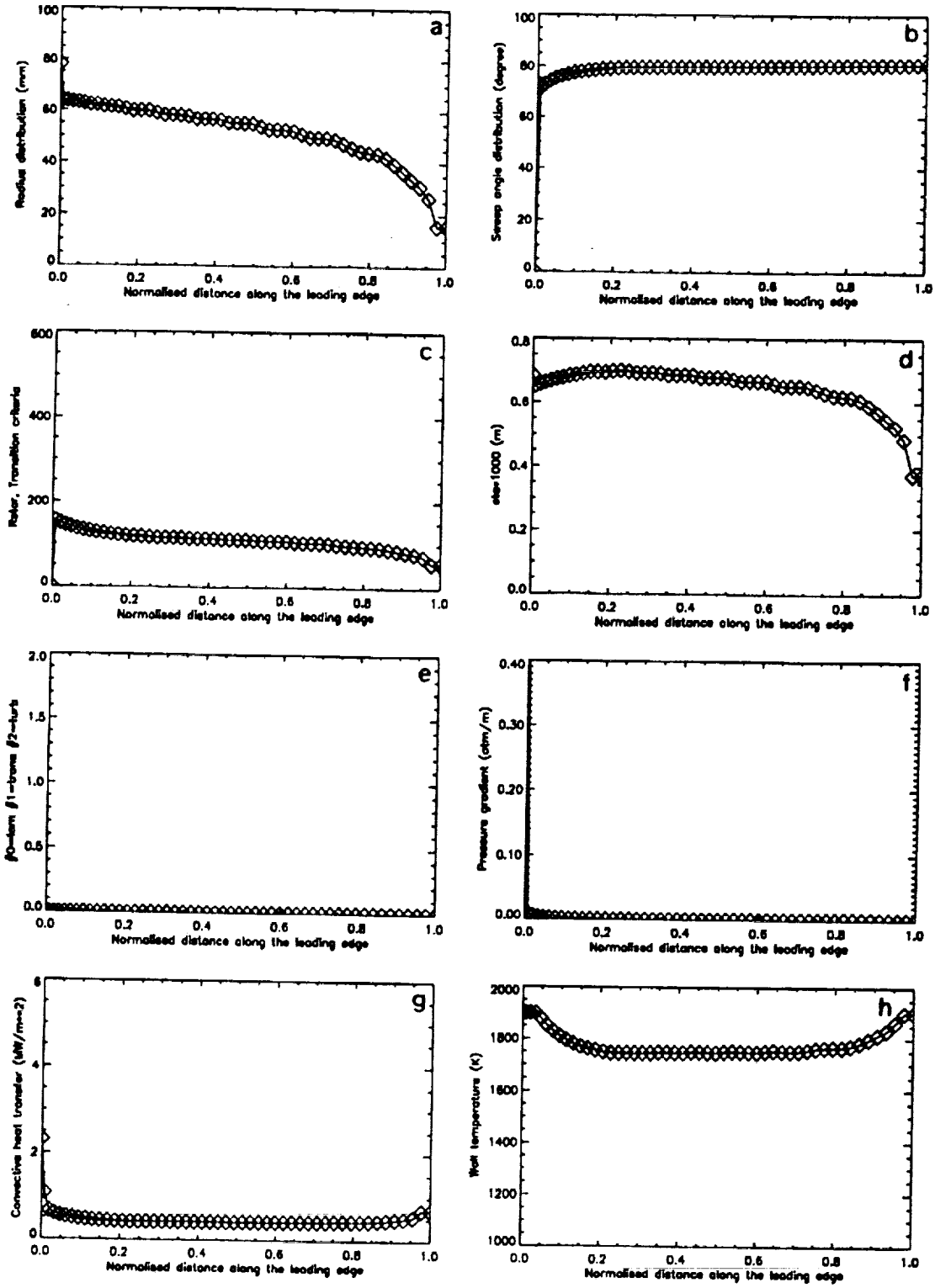

Figure 30 Leading edge results, L/D optimized, $M_\infty = 10$, $Q_\infty = 0.2$ atm.

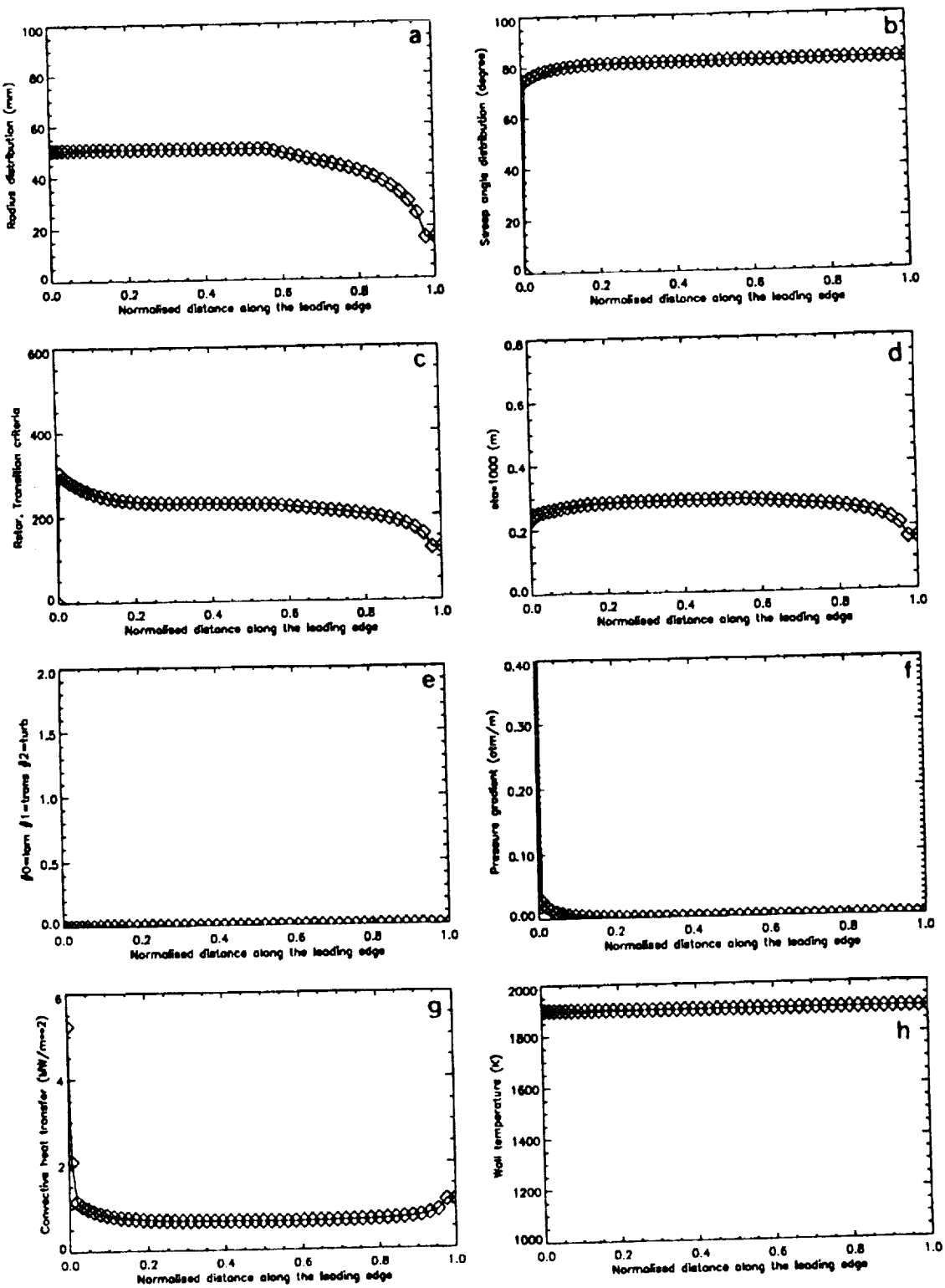

Figure 31 Leading edge results, L/D optimized, $M_\infty = 10.$ $Q_\infty = 1.0$ $atm.$

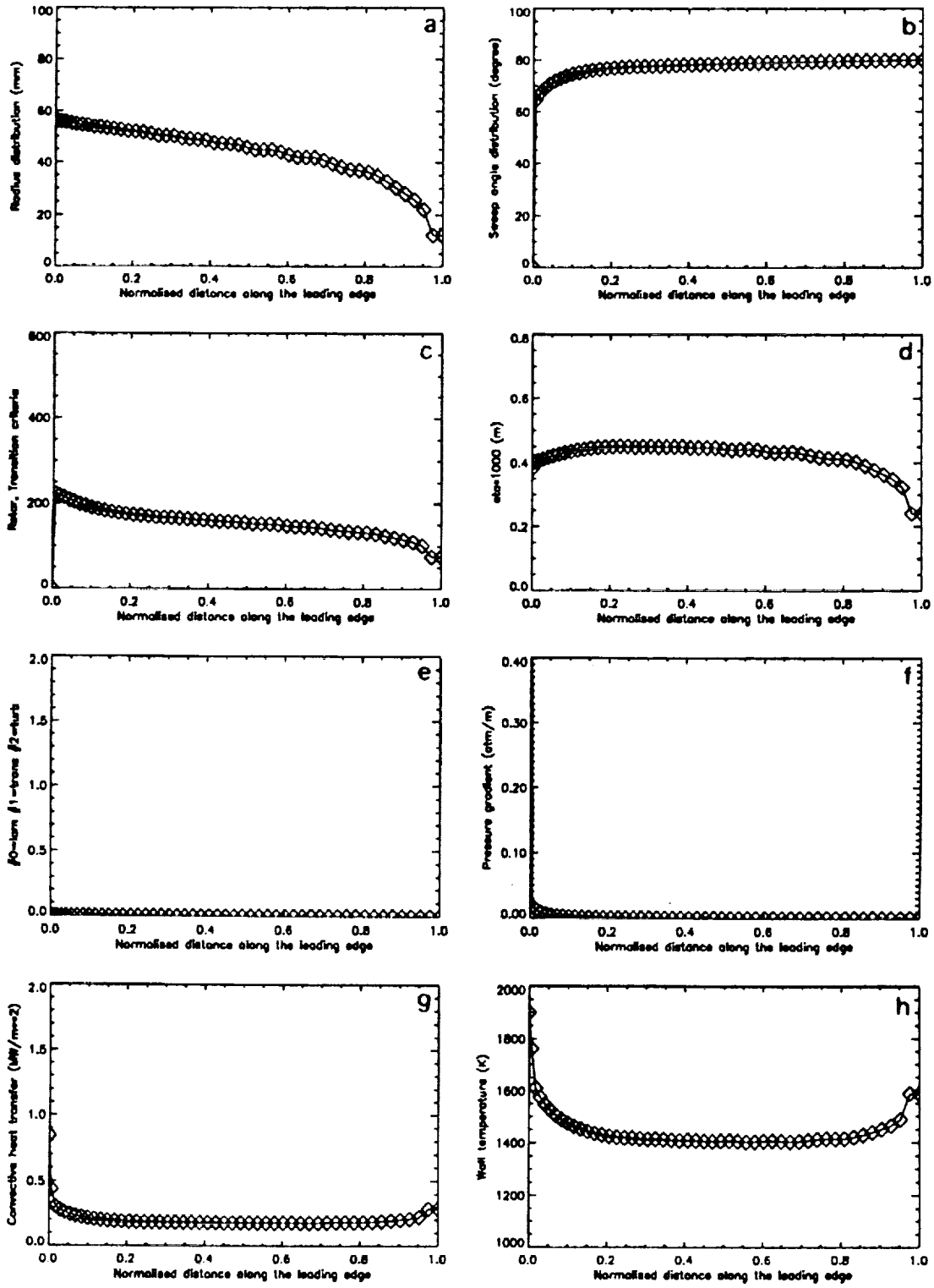

Figure 32 Leading edge results, L/D optimized, $M_\infty = 15$, $Q_\infty = 0.2$ atm.

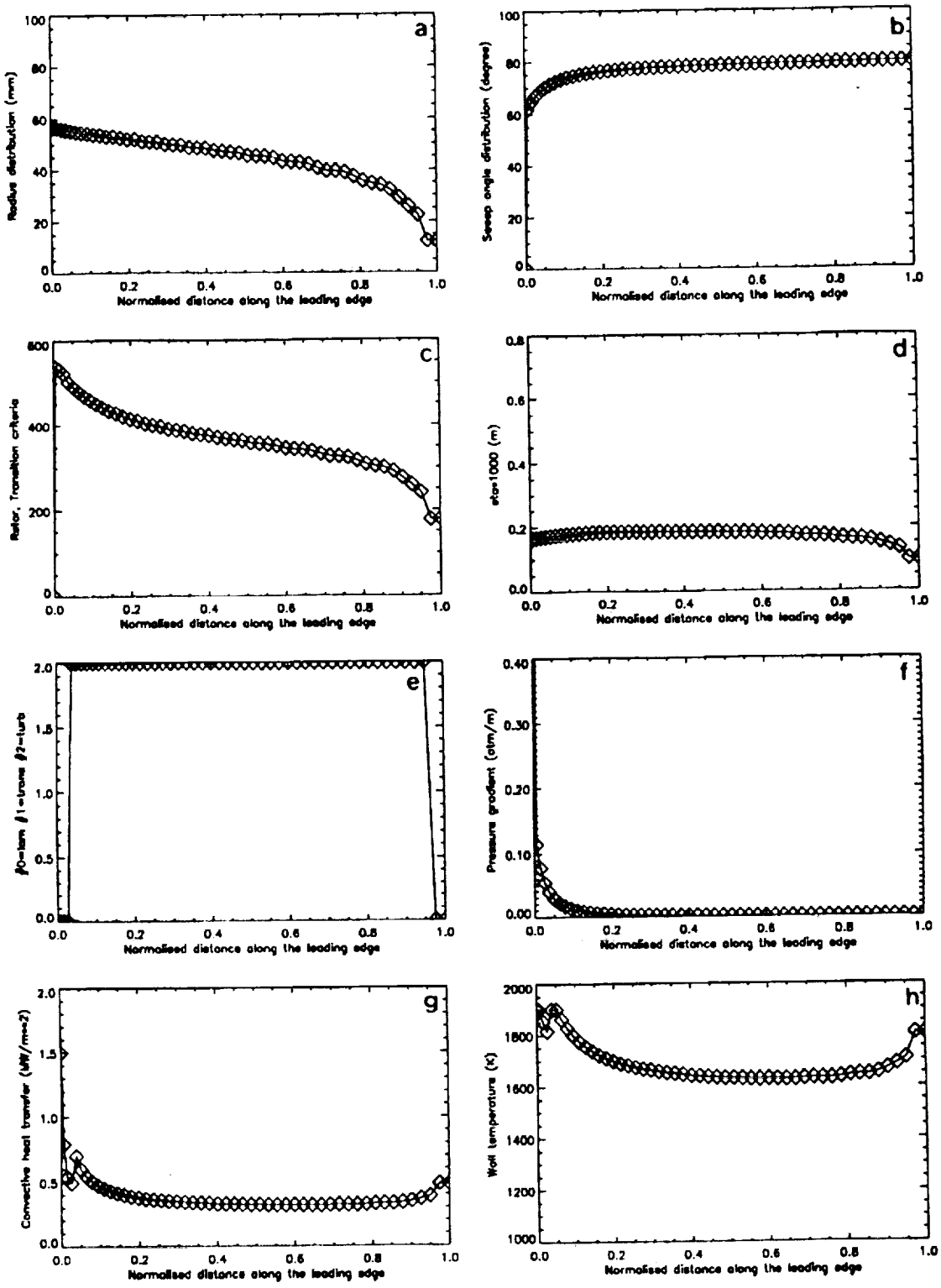

Figure 33 Leading edge results, L/D optimized, $M_\infty = 15$, $Q_\infty = 1.0$ atm.

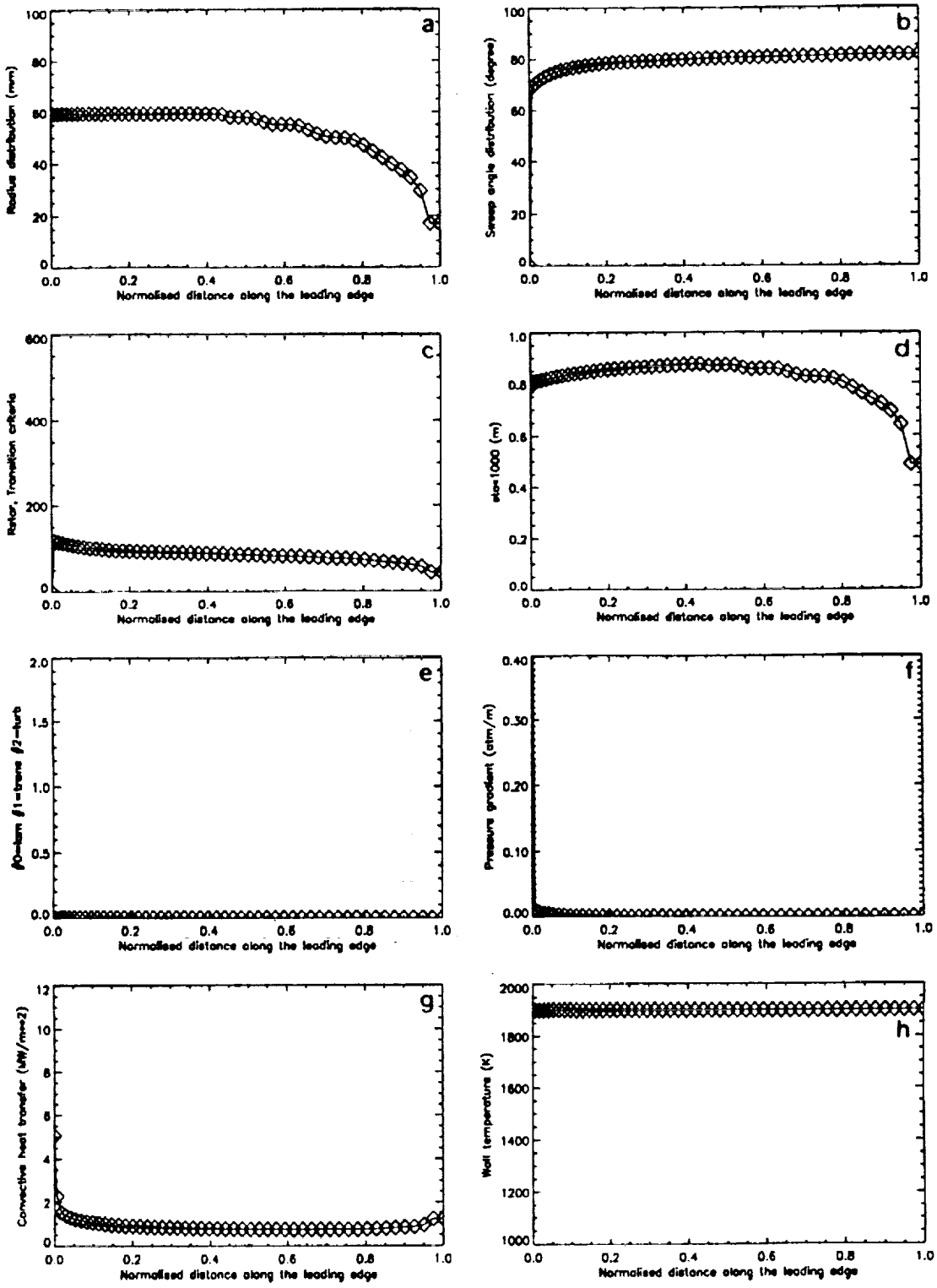

Figure 34 Leading edge results, L/D optimized, $M_{\infty} = 20$, $Q_{\infty} = 0.2$ atm.

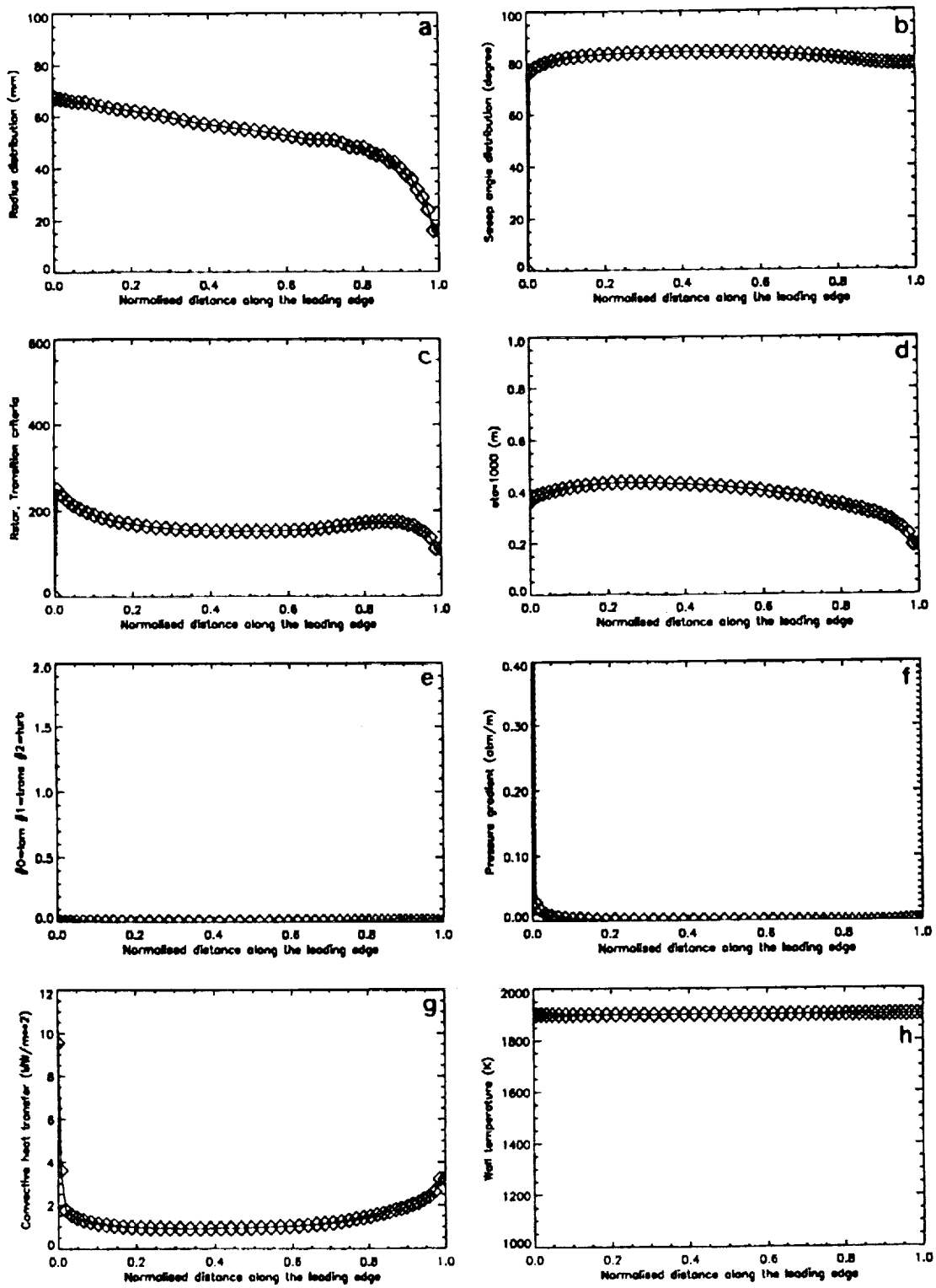

Figure 35 Leading edge results, L/D optimized, $M_\infty = 20$, $Q_\infty = 1.0$ atm.

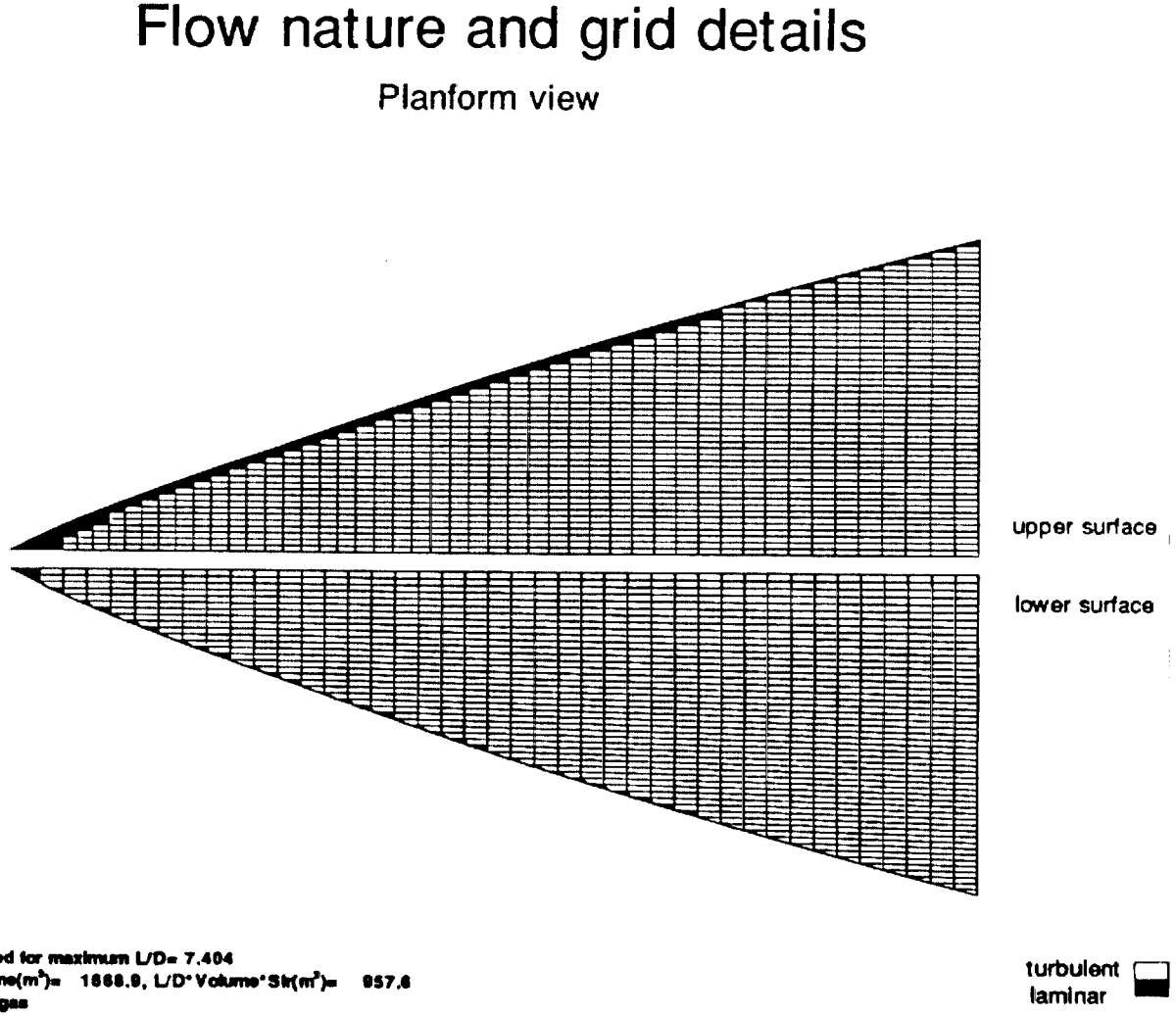

Figure 36 Transition front, $M_\infty = 5$, $Q_\infty = 0.2$ *atm*.

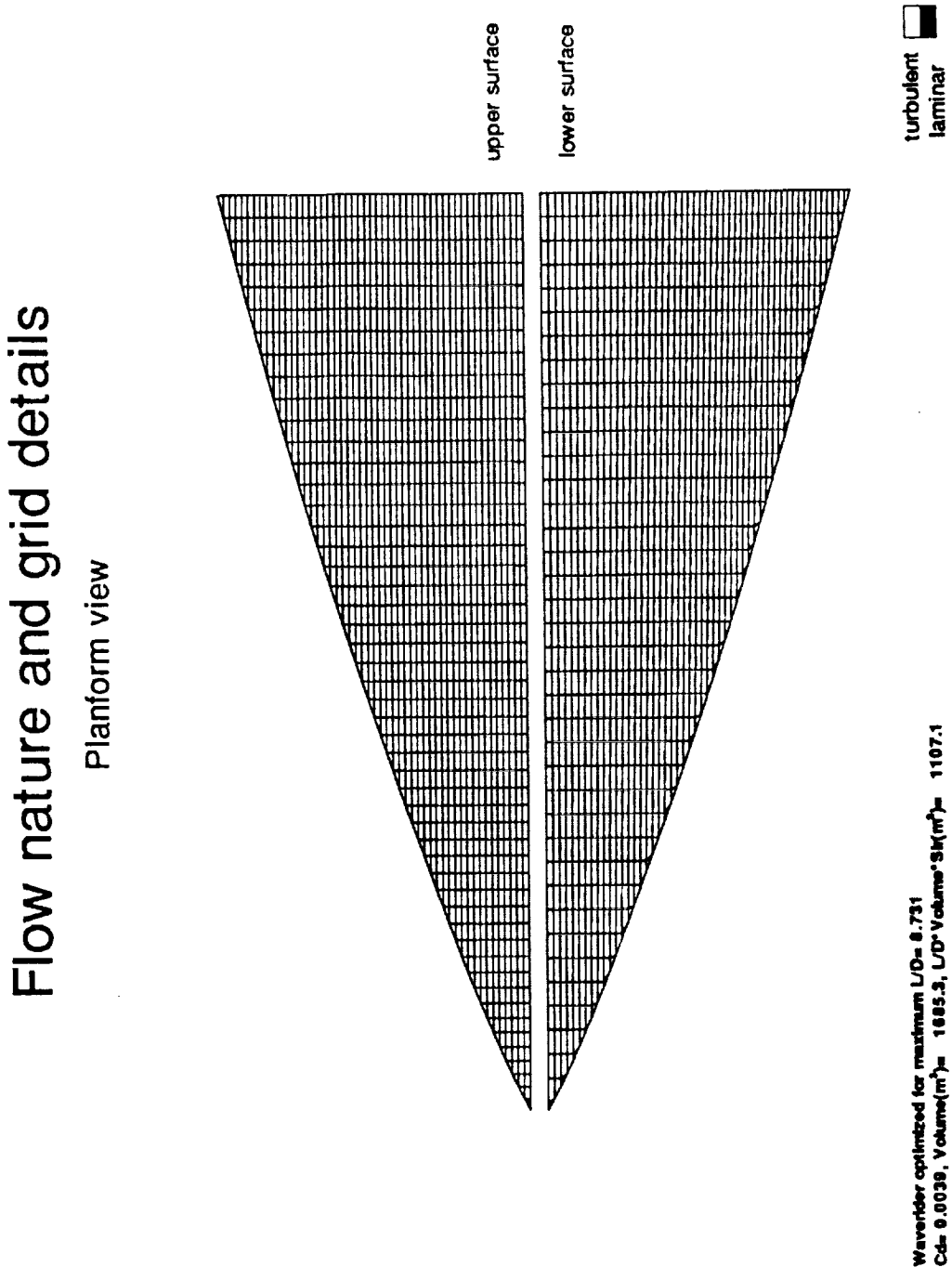

Figure 37 Transition front, $M_\infty = 5$, $Q_\infty = 1.0$ atm.

C-2

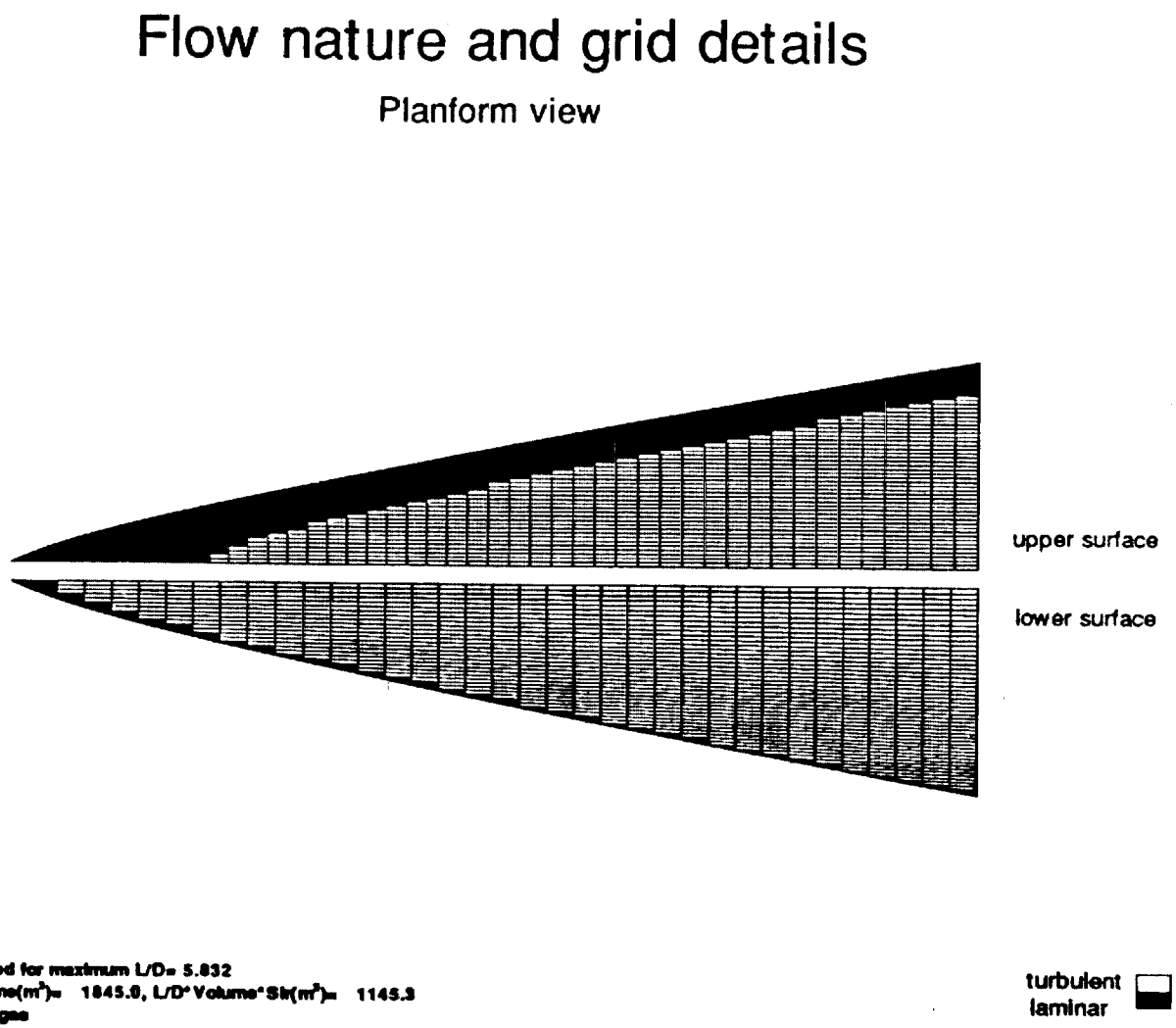

Figure 38 Transition front, $M_\infty = 10$, $Q_\infty = 0.2$ *atm*.

Figure 39 Transition front, $M_\infty = 10, \quad Q_\infty = 1.0 \quad atm.$

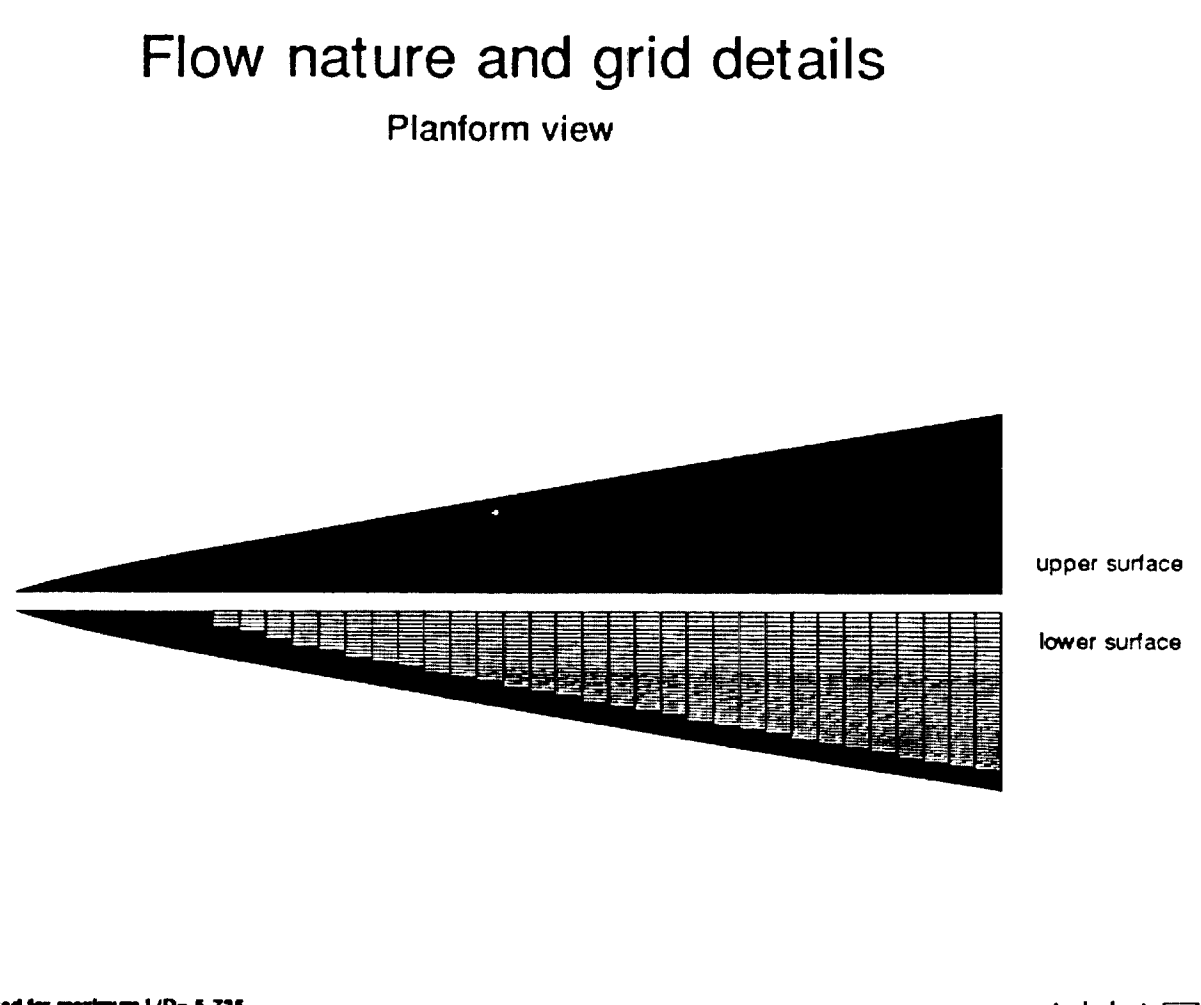

Figure 40 Transition front, $M_\infty = 15$, $Q_\infty = 0.2$ *atm*.

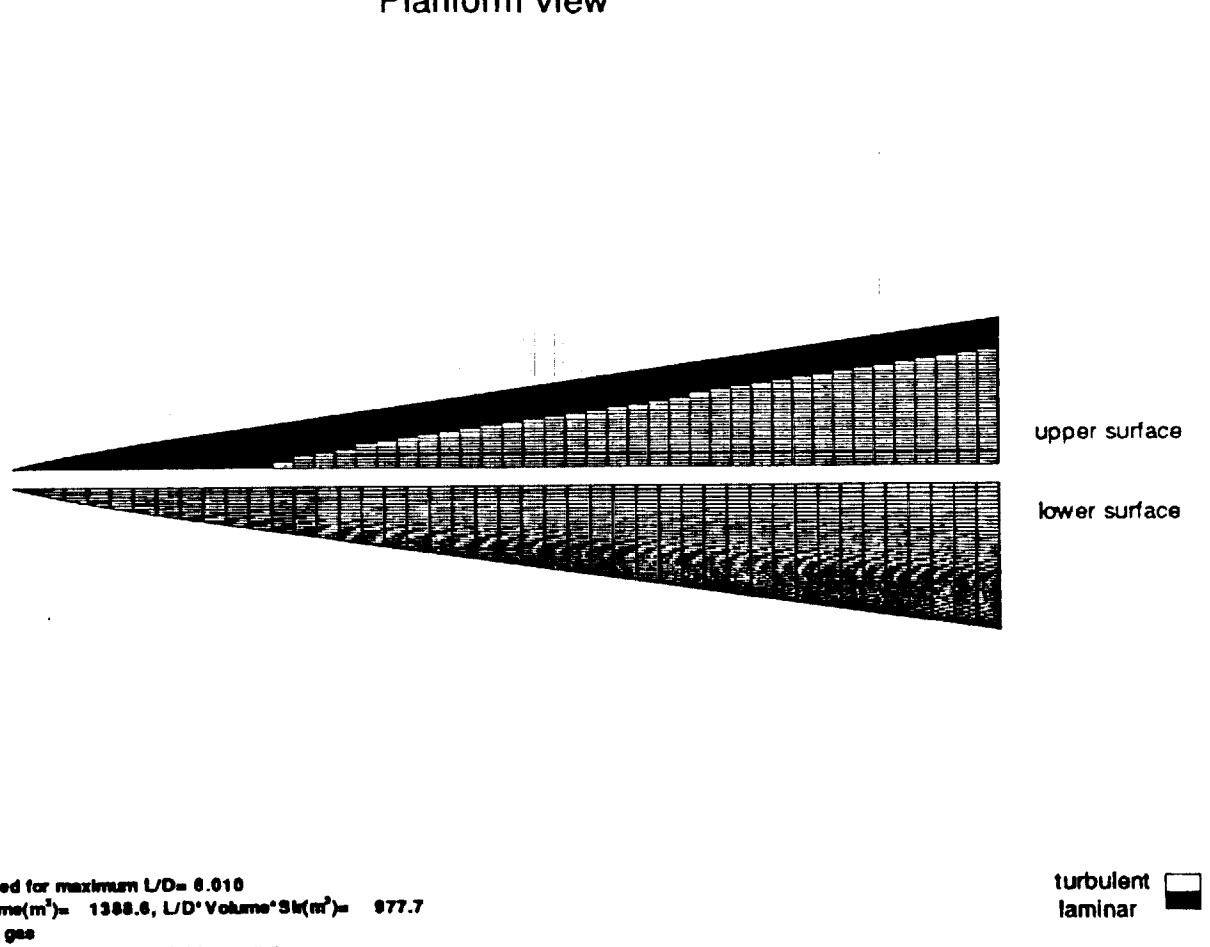

Figure 41 Transition front, $M_\infty = 15$, $Q_\infty = 1.0$ atm.

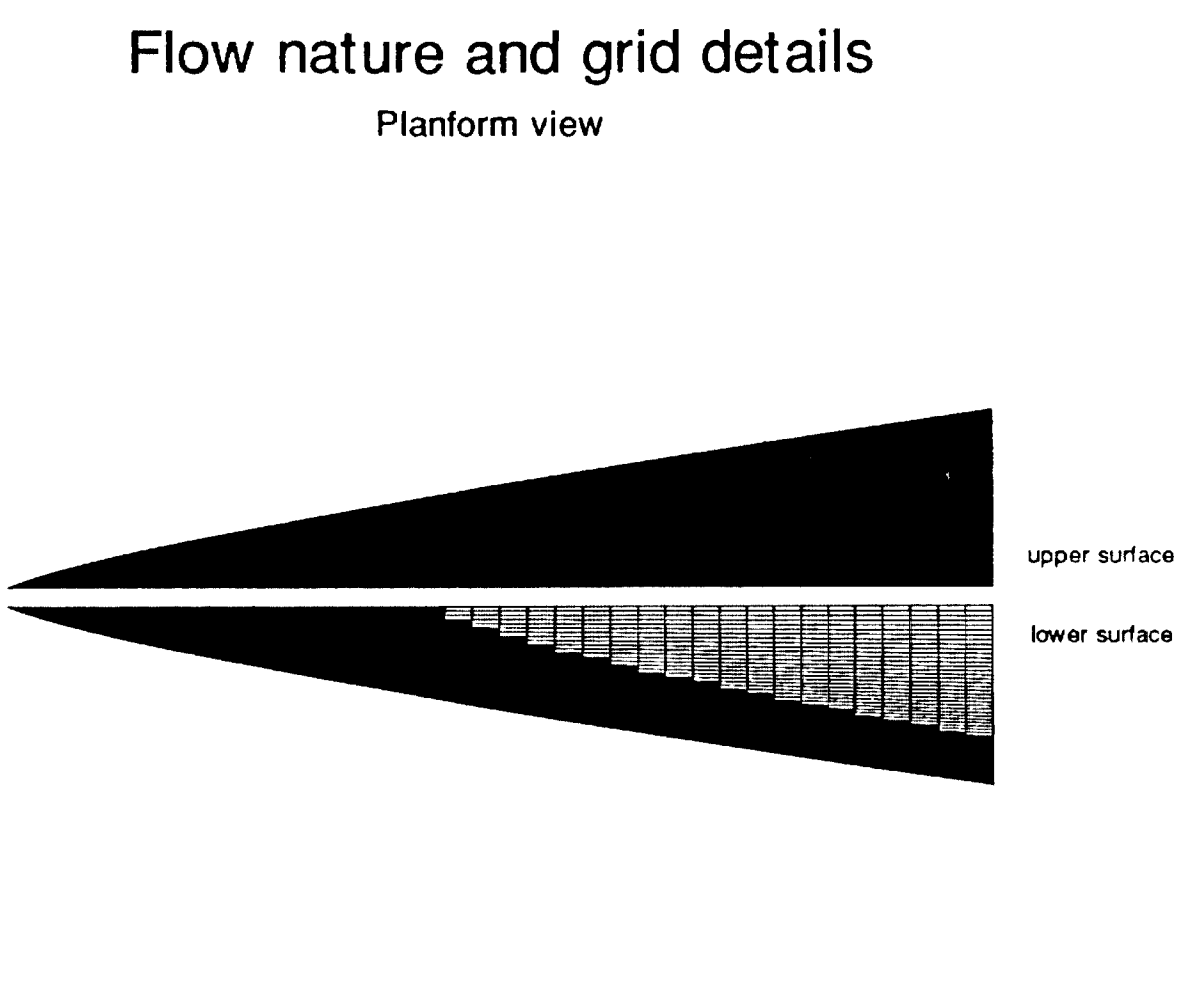

Figure 42 Transition front, $M_\infty = 20$, $Q_\infty = 0.2$ atm.

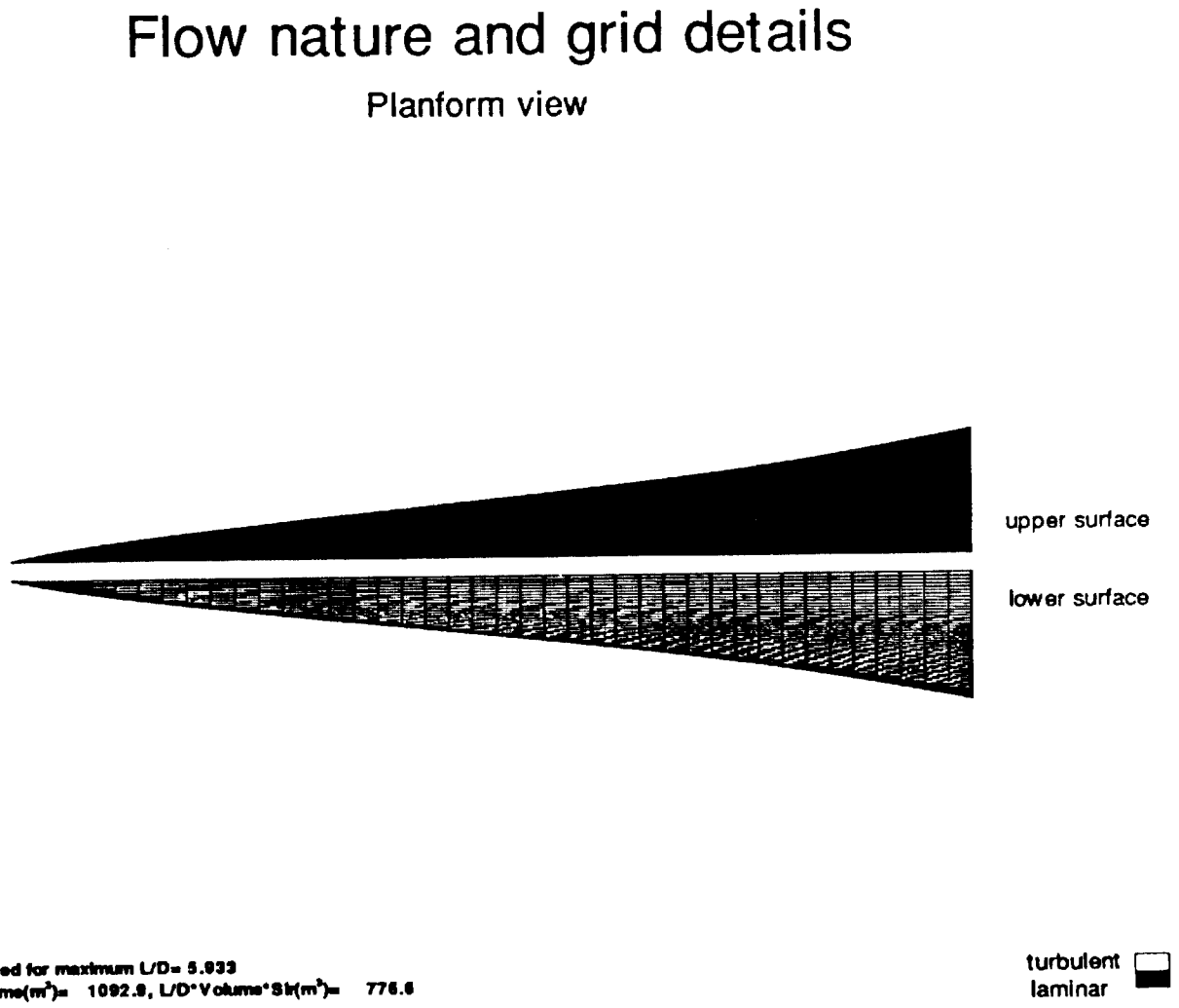

Figure 43 Transition front, $M_\infty = 20$, $Q_\infty = 1.0$ atm.

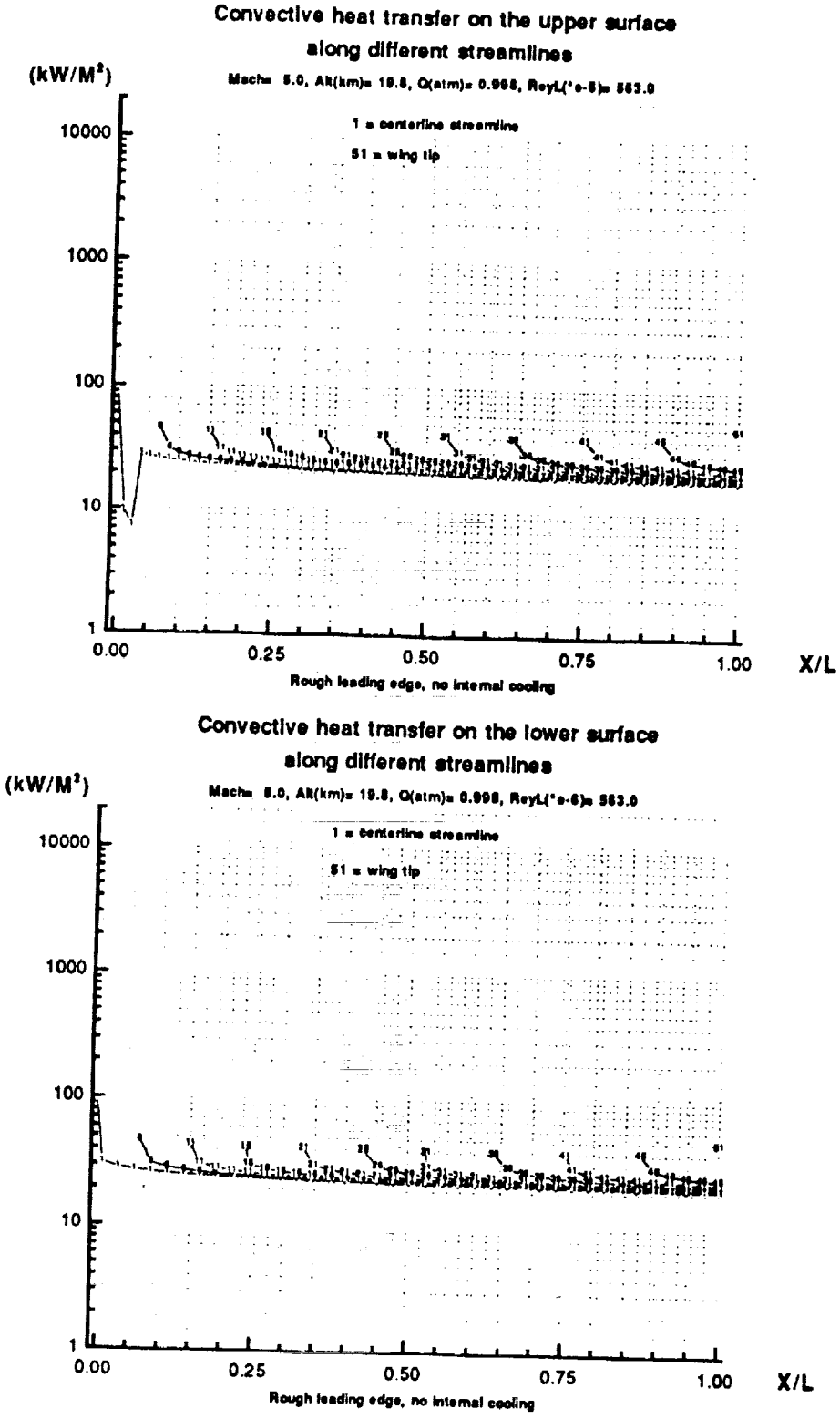

Figure 44 Convective heat transfer on the upper and lower surface along different streamlines, $M_\infty = 5$, $Q_\infty = 1.0$ atm.

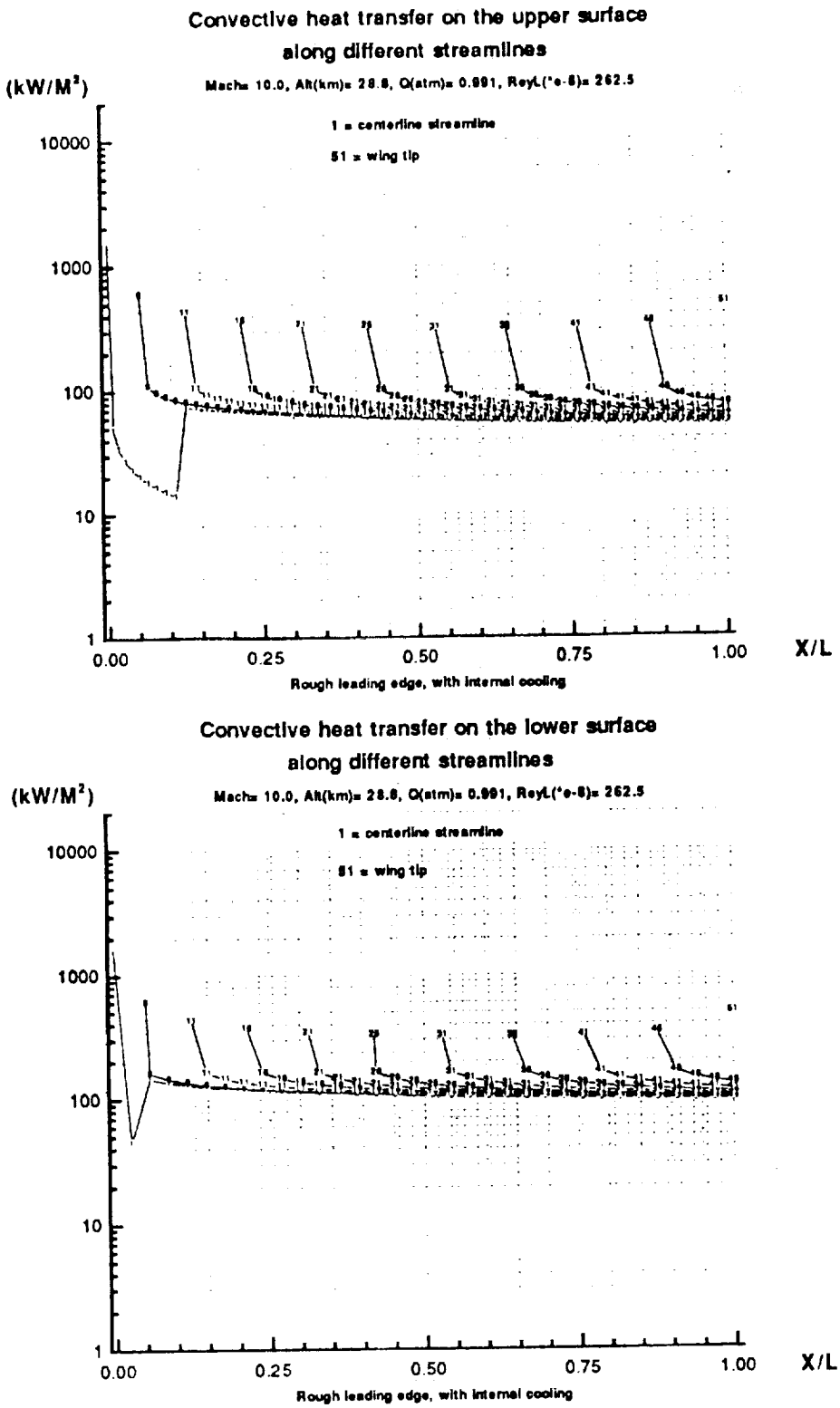

Figure 45 Convective heat transfer on the upper and lower surface along different streamlines, $M_\infty = 10$, $Q_\infty = 1.0$ atm.

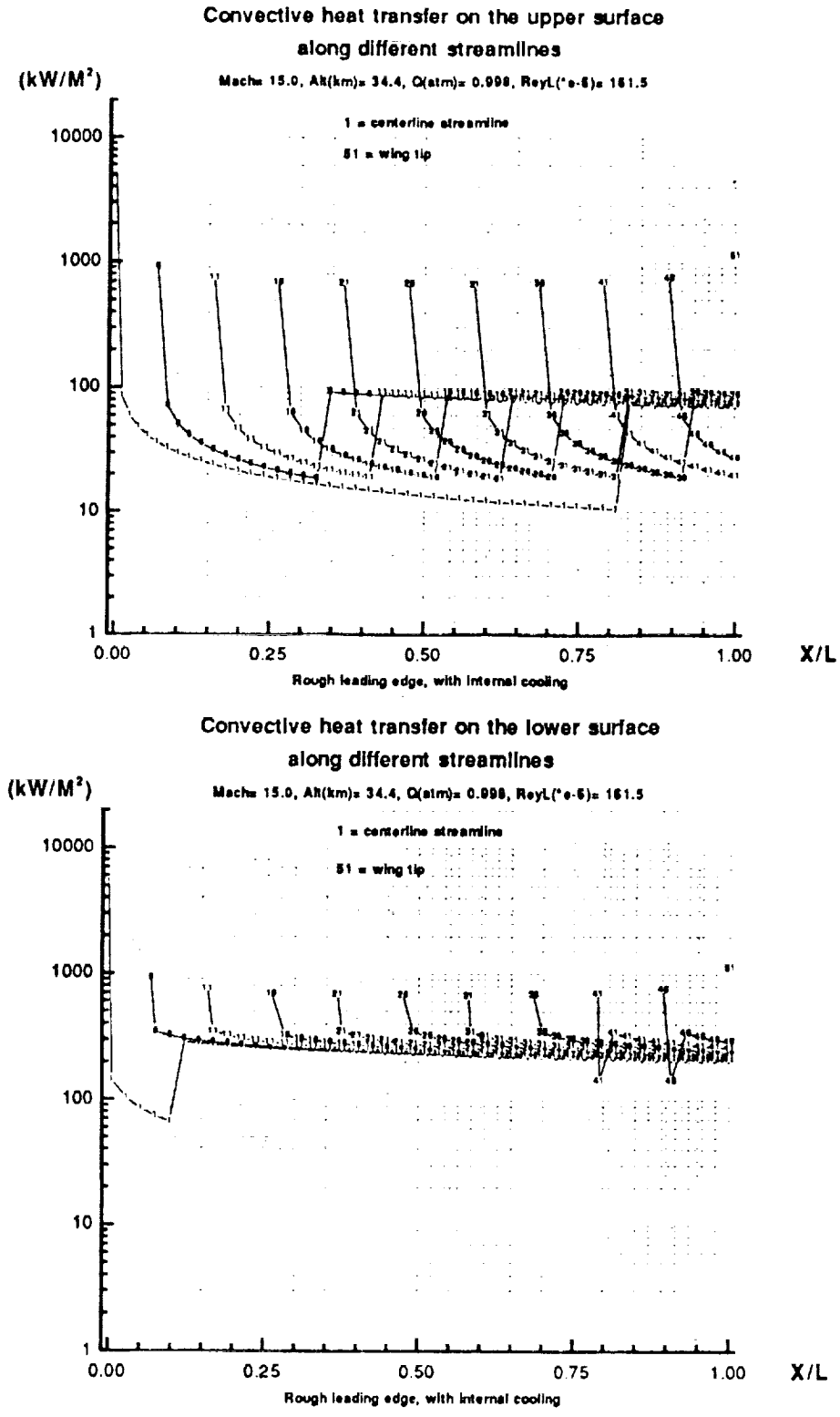

Figure 46 Convective heat transfer on the upper and lower surface along different streamlines, $M_\infty = 15$, $Q_\infty = 1.0$ atm.

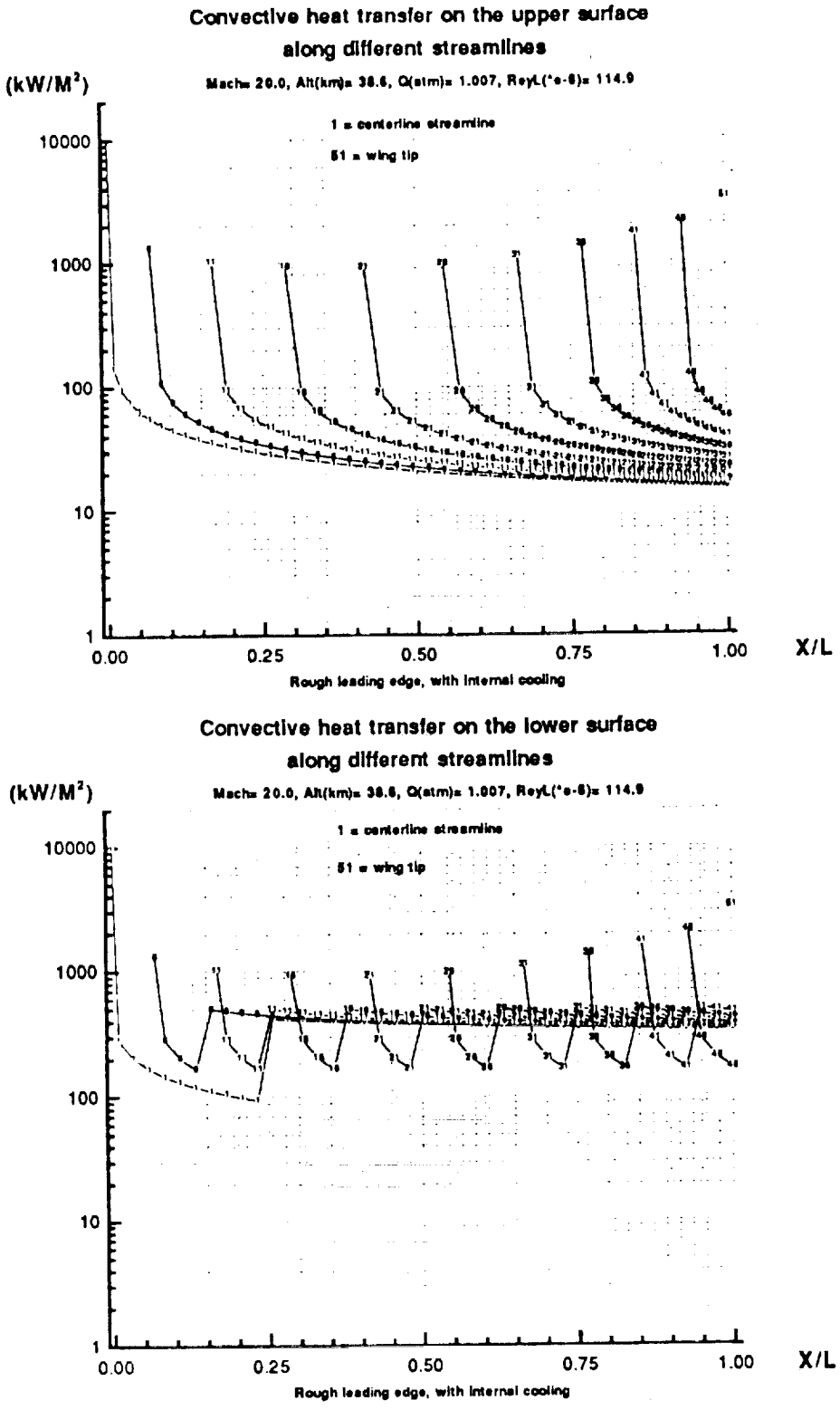

Figure 47 Convective heat transfer on the upper and lower surface along different streamlines, $M_\infty = 20$, $Q_\infty = 1.0$ atm.

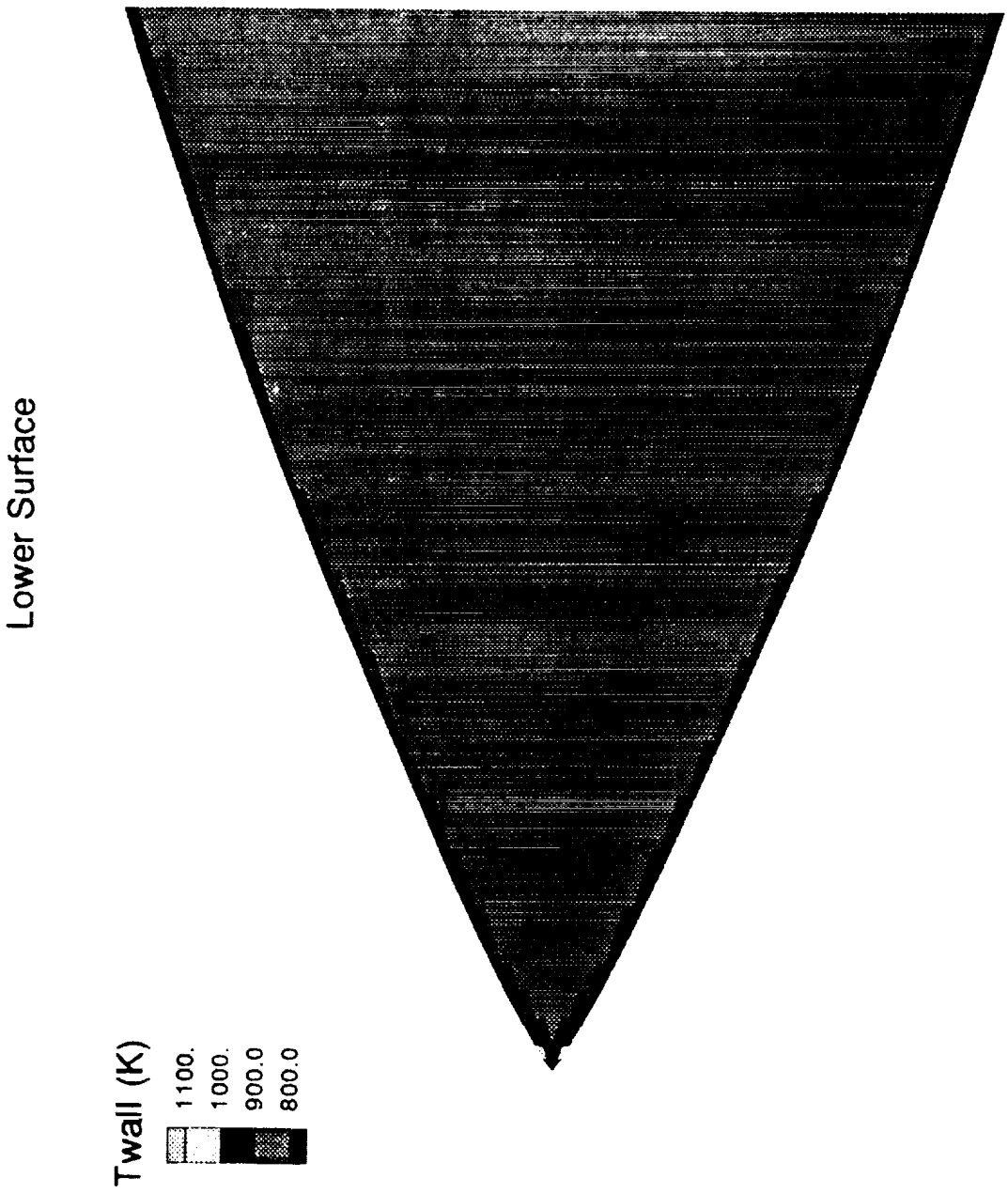

Figure 48 Wall temperature distribution on the lower surface, $M_\infty = 5$, $Q_\infty = 1.0$ *atm*.

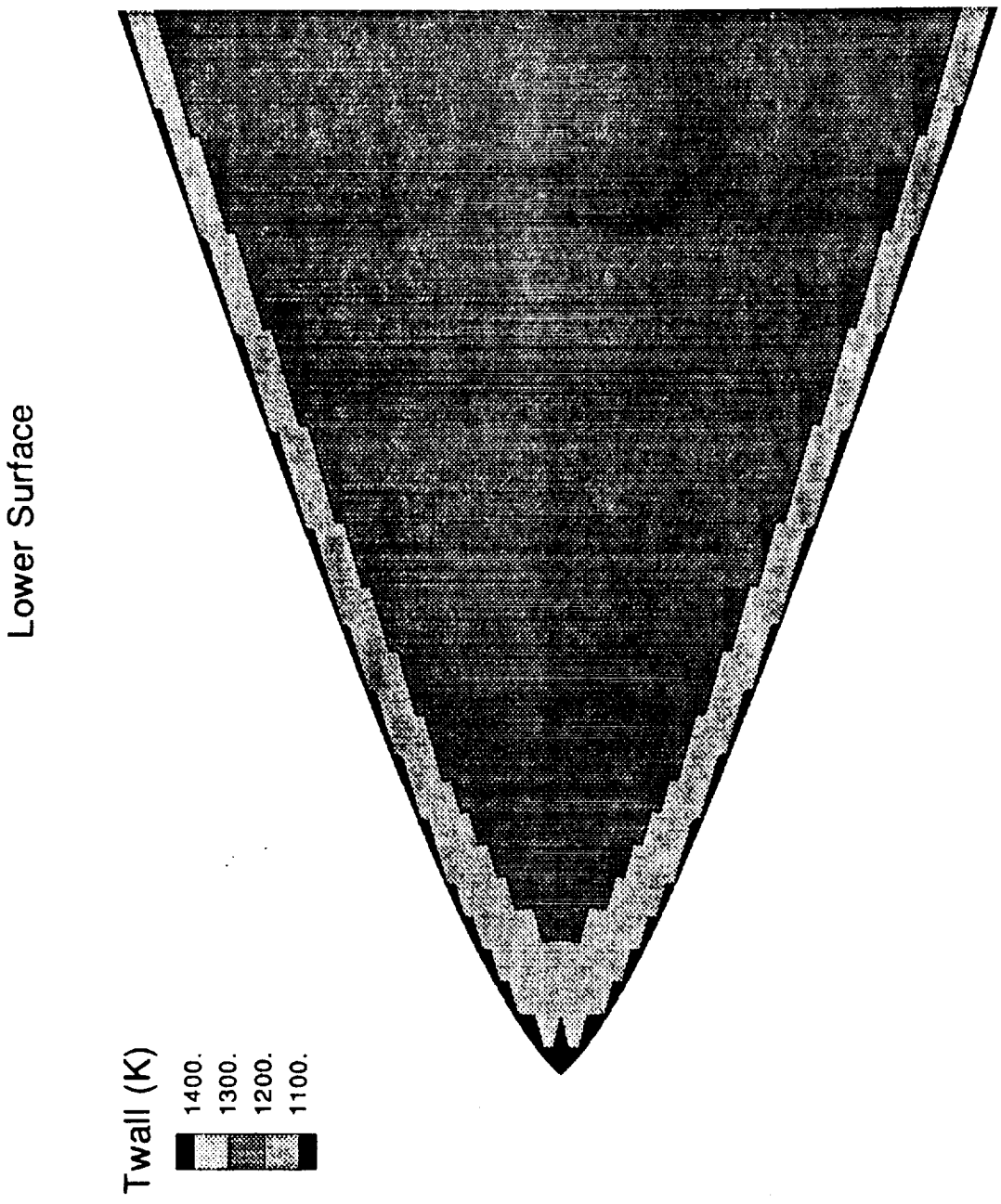

Figure 49 Wall temperature distribution on the lower surface, $M_\infty = 10$, $Q_\infty = 1.0$ *atm*.

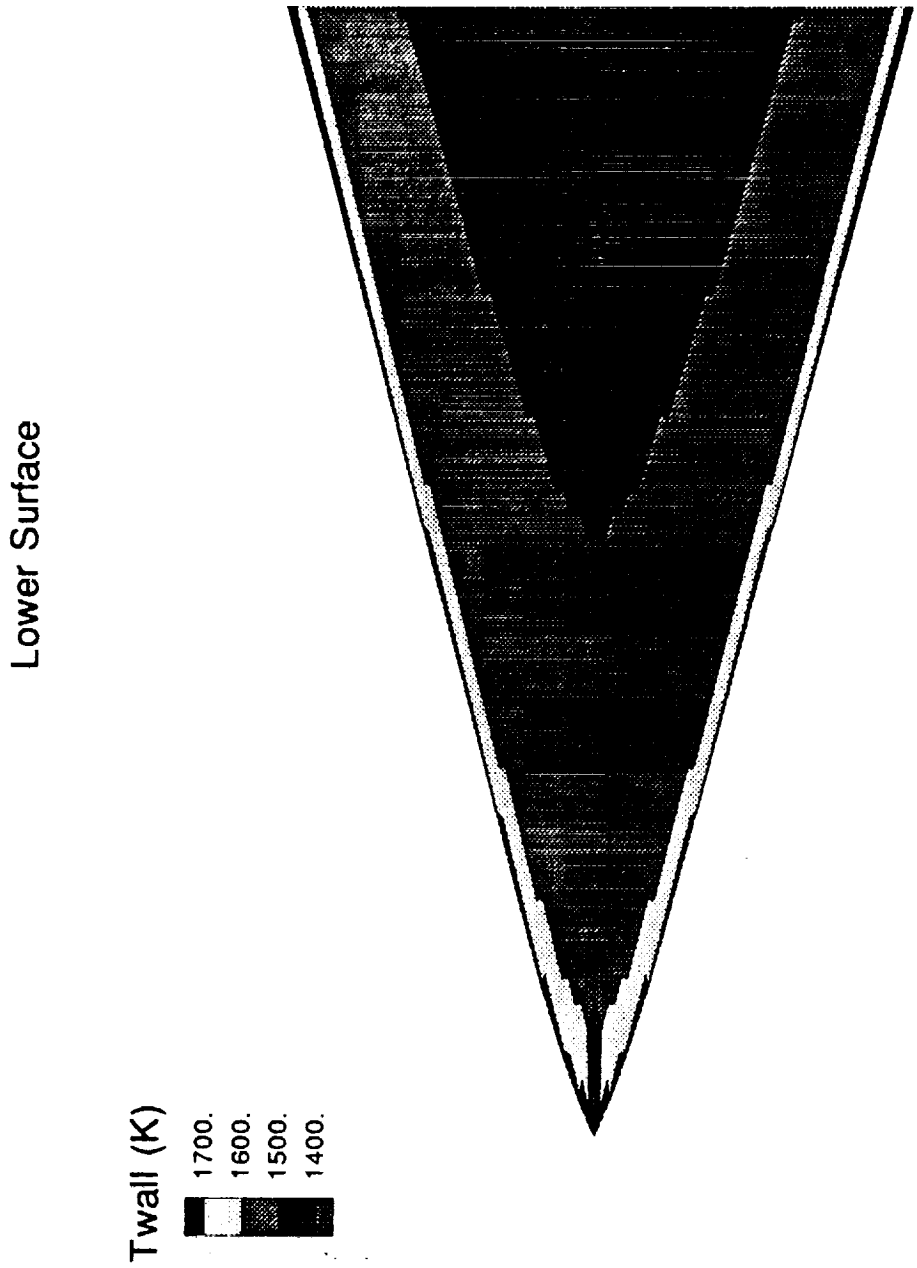

Figure 50 Wall temperature distribution on the lower surface, $M_\infty = 15$, $Q_\infty = 1.0$ *atm*.

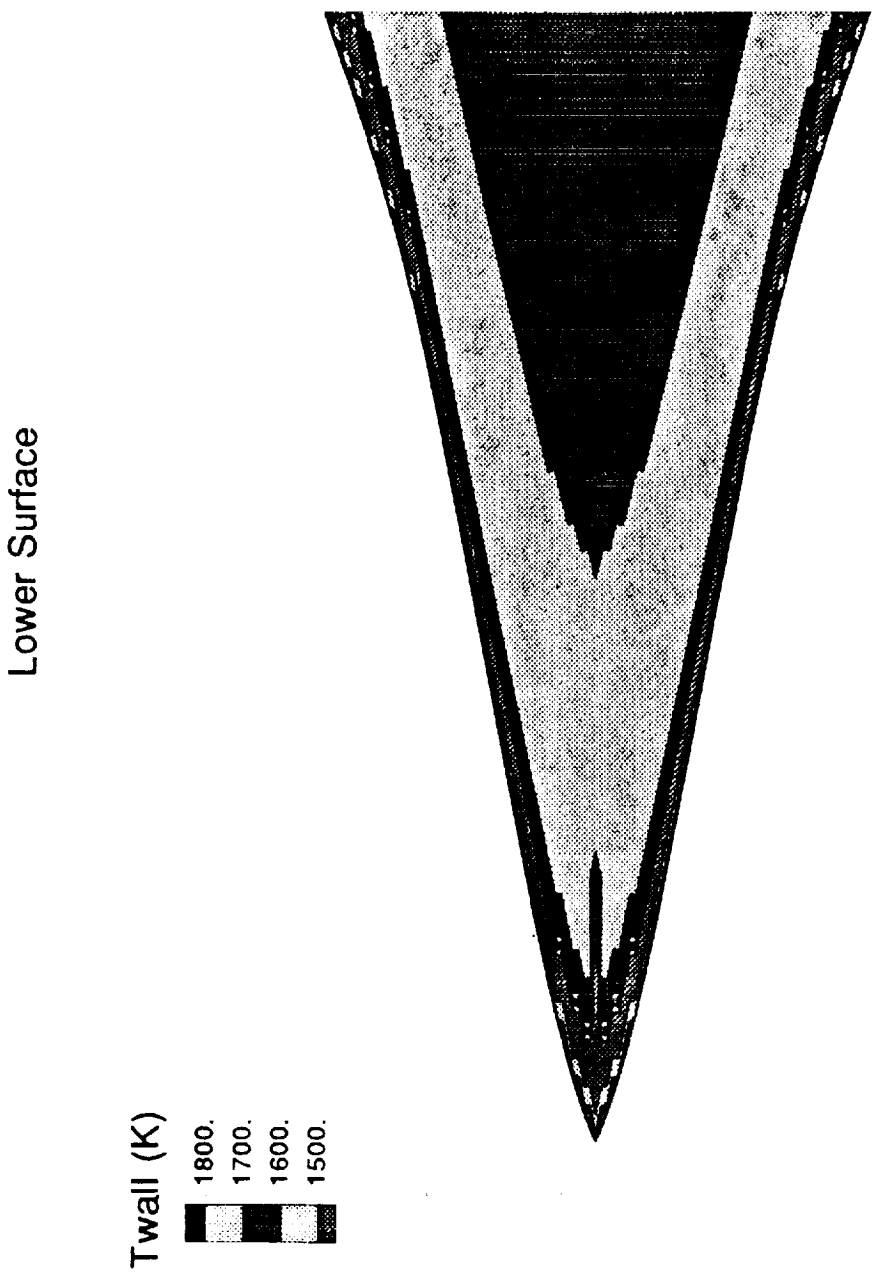

Figure 51 Wall temperature distribution on the lower surface, $M_\infty = 20$, $Q_\infty = 1.0$ atm.

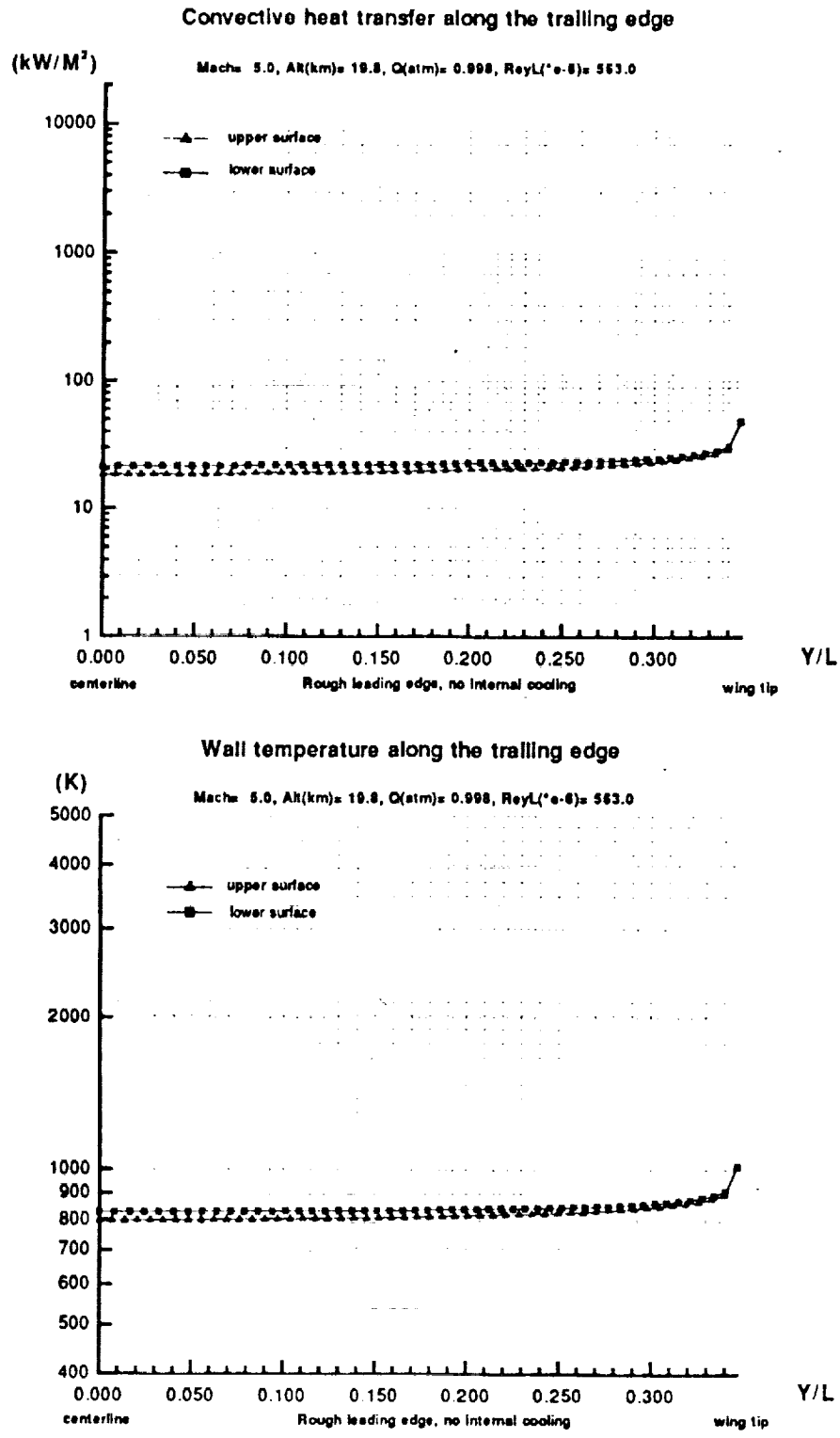

Figure 52 Convective heat transfer and wall temperature along the trailing edge of the upper and lower surface, $M_\infty = 5$, $Q_\infty = 1.0$ atm.

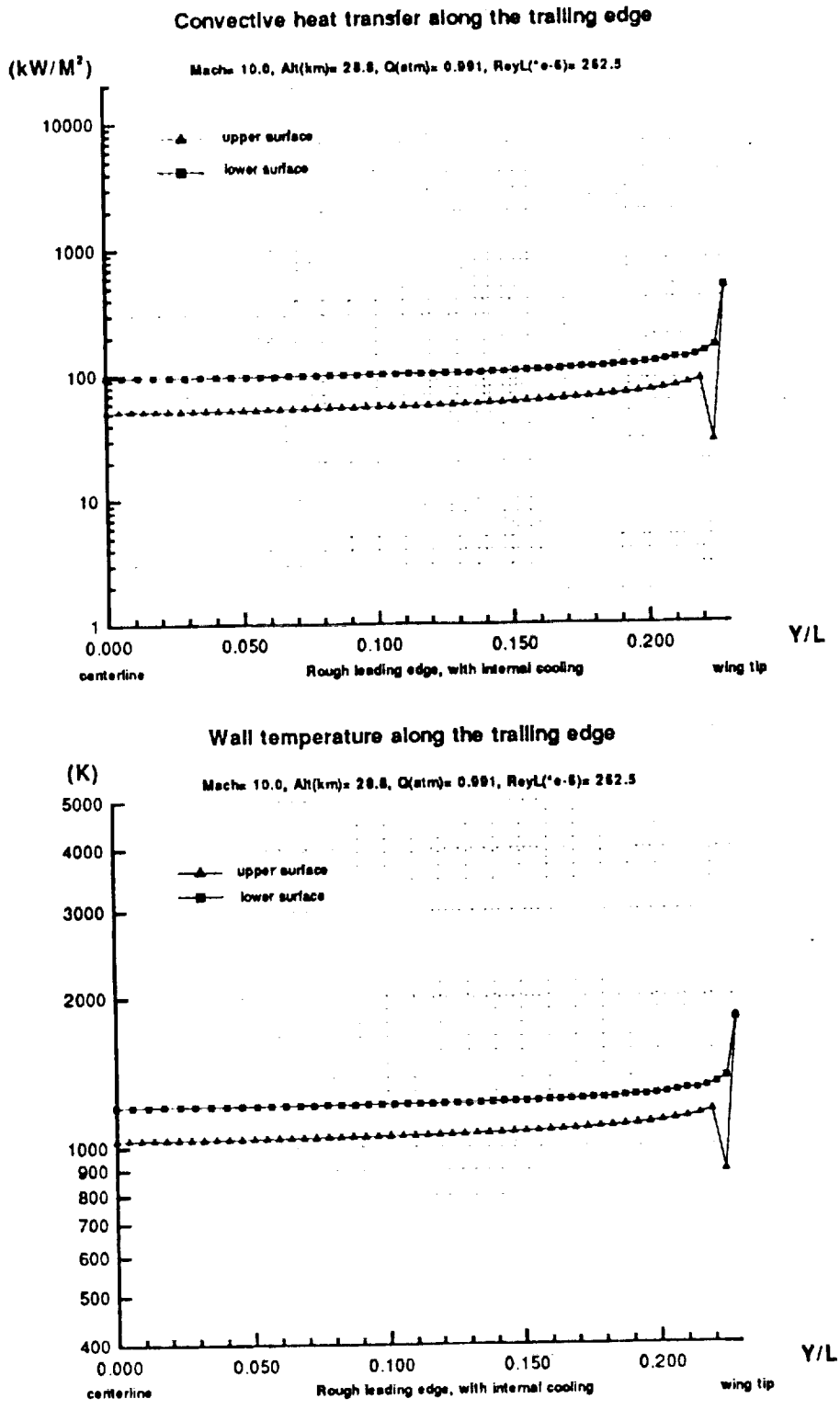

Figure 53 Convective heat transfer and wall temperature along the trailing edge of the upper and lower surface, $M_\infty = 10$, $Q_\infty = 1.0$ atm.

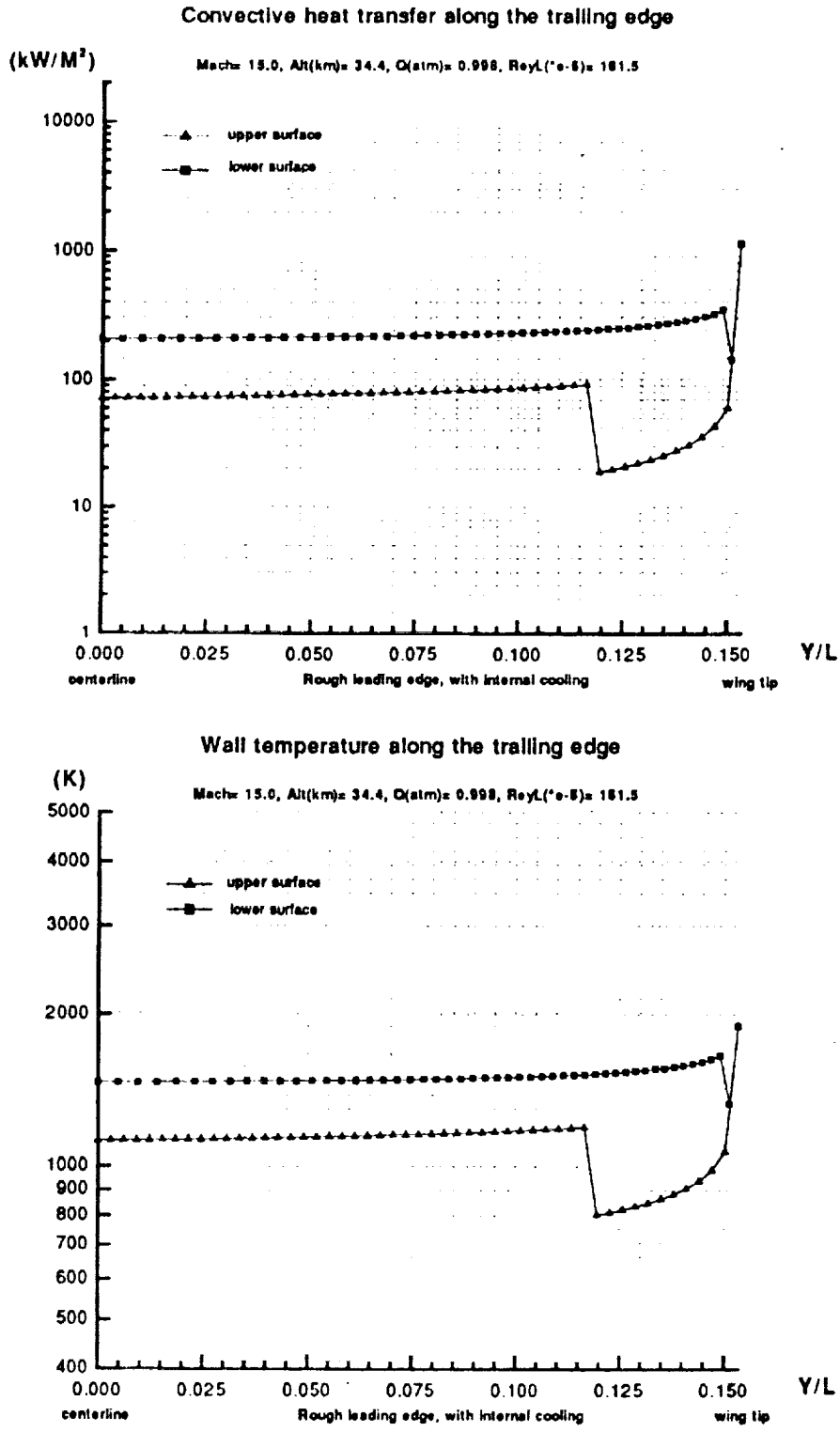

Figure 54 Convective heat transfer and wall temperature along the trailing edge of the upper and lower surface, $M_\infty = 15$, $Q_\infty = 1.0$ atm.

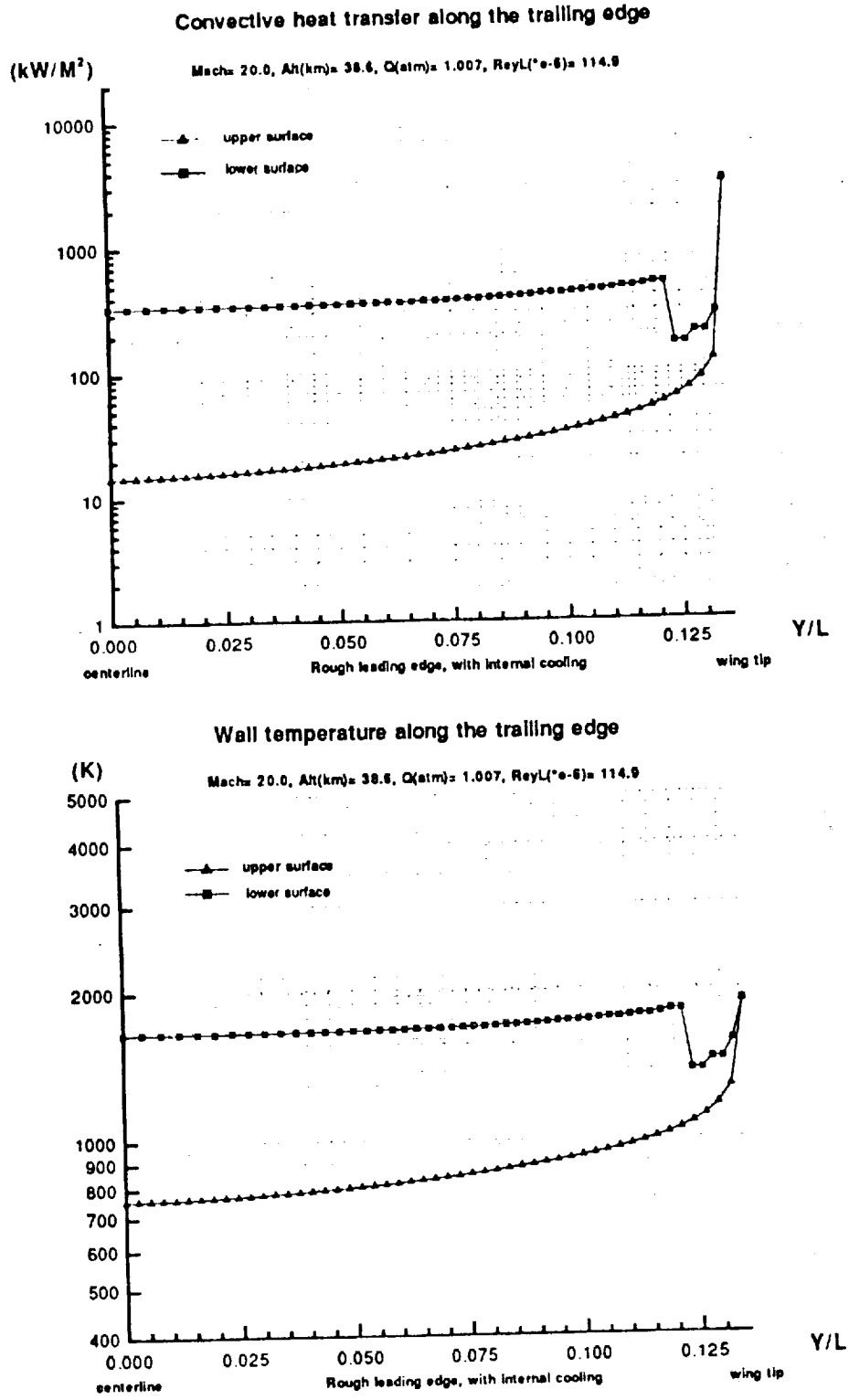

Figure 55 Convective heat transfer and wall temperature along the trailing edge of the upper and lower surface, $M_\infty = 20$, $Q_\infty = 1.0$ atm.

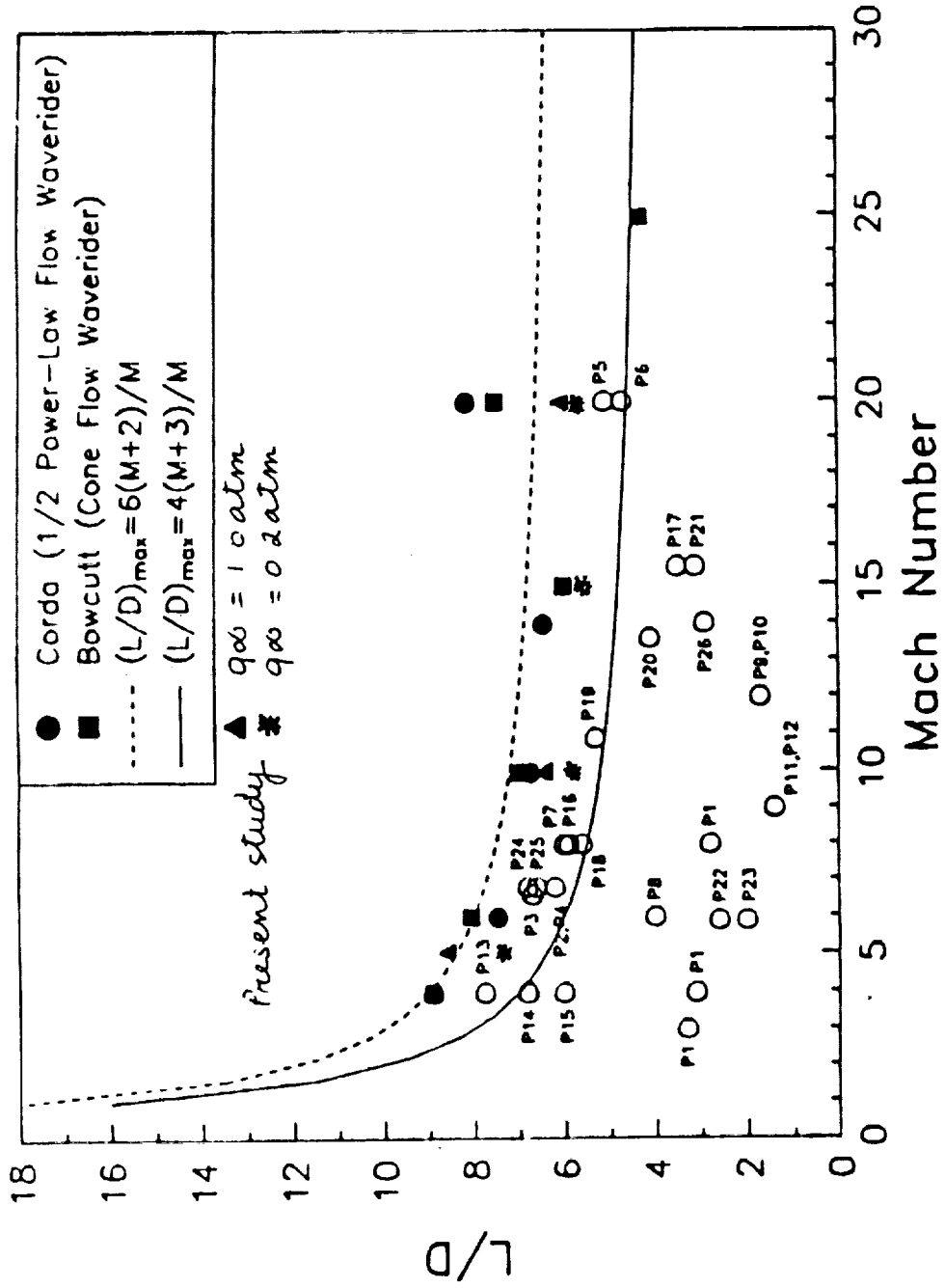

Figure 56 Waveriders performance comparison

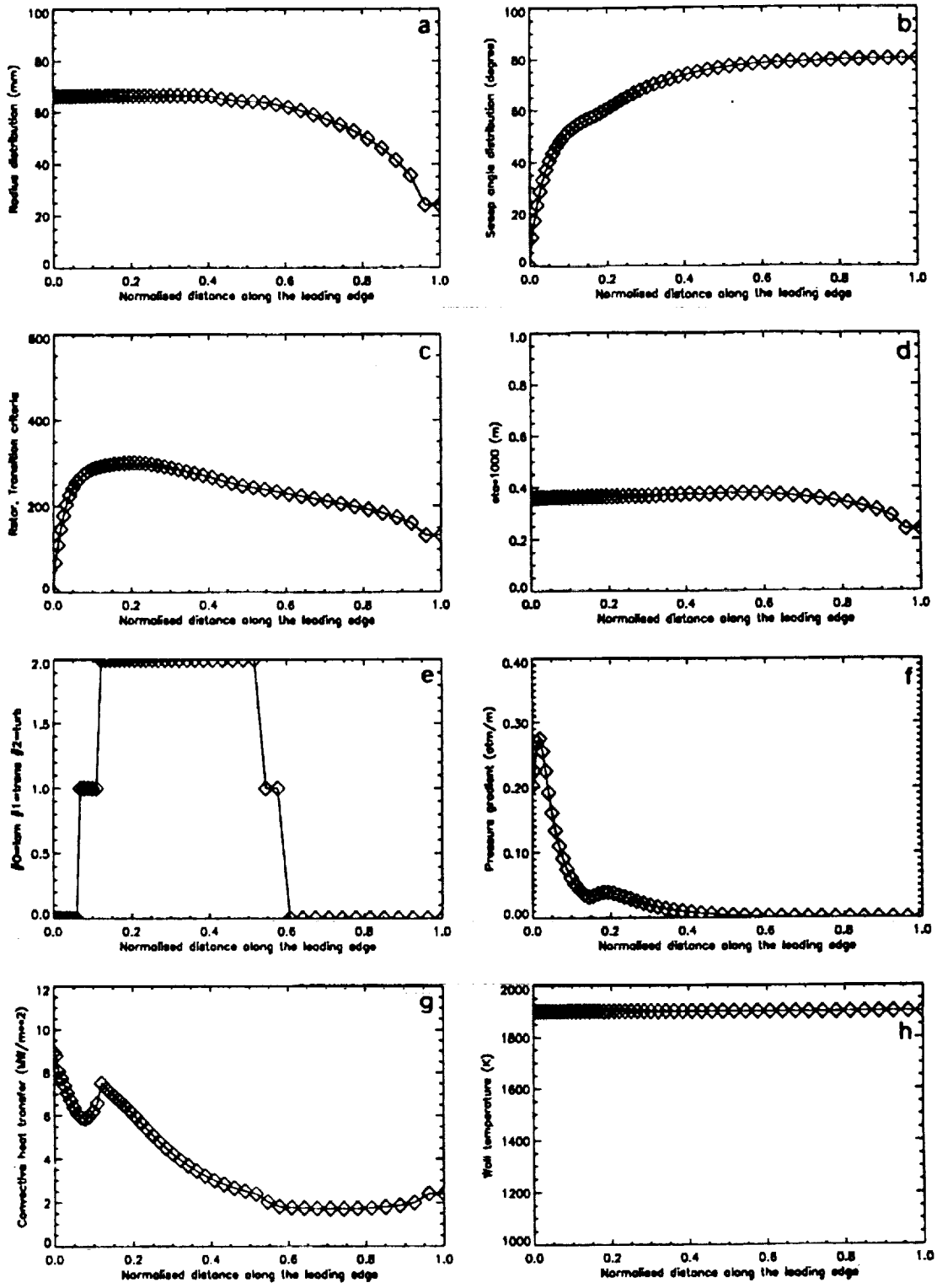

Figure 57 Leading edge results, Volume optimized, $M_\infty = 20$, $Q_\infty = 1.0$ *atm*.

Figure 58 Transition front, Volume optimized, $M_\infty = 20$, $Q_\infty = 1.0$ atm.

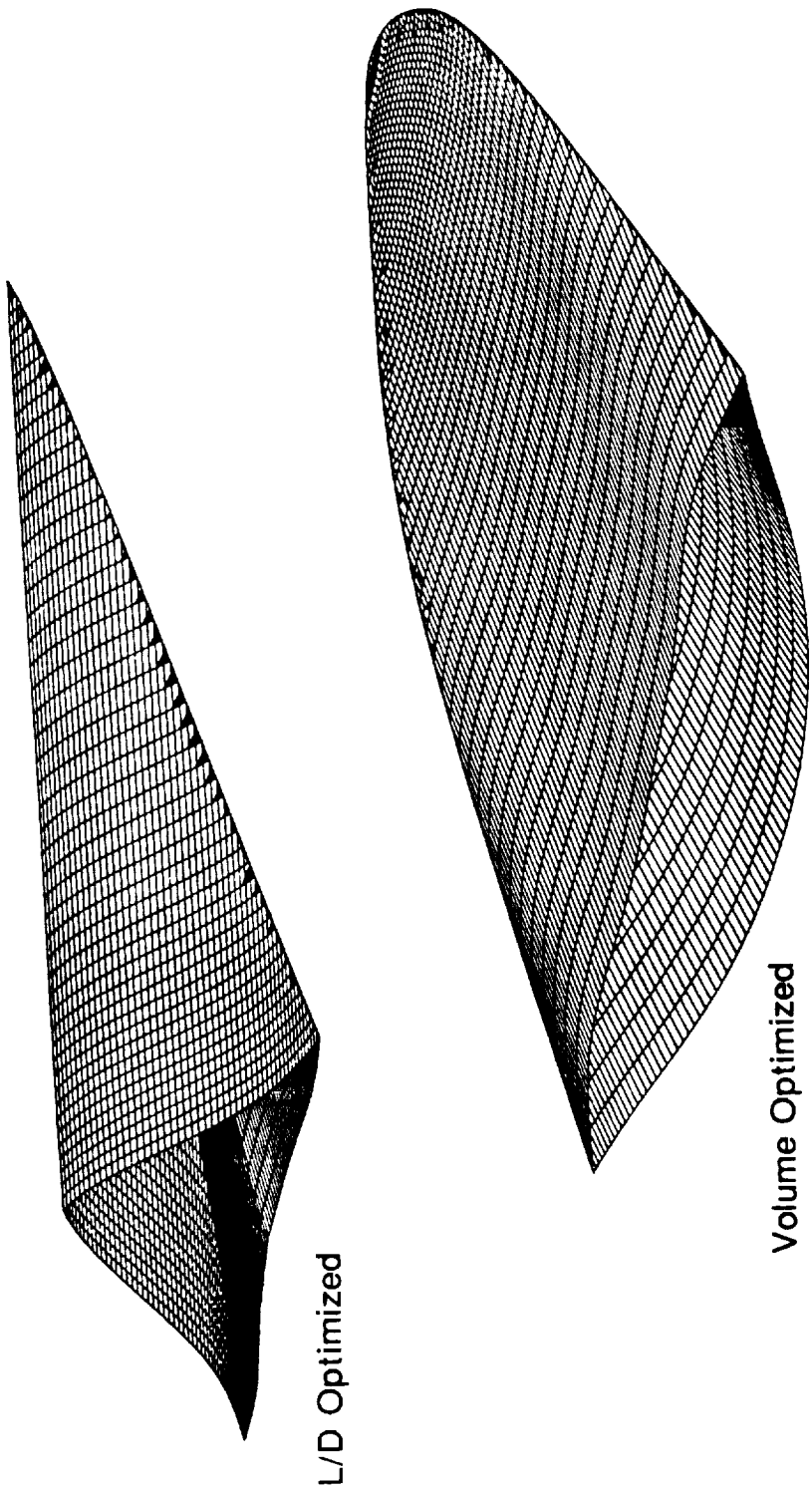

Figure 59 Waverider optimized for L/D Vs Waverider optimized for Volume, $M_\infty = 20, \quad Q_\infty = 1.0 \quad atm.$

Appendix C Constraints on waverider construction and simplex optimization

The following section was almost entirely copied from McLaughlin[4]. We have simply added here the set of new constraints which are now imposed in the modified version of the code.

Certain constraints must be enforced in order to create valid waveriders, and to have control over the optimization procedure. Each constraint is stated and discussed in the following sections.

Recall that the leading edge curve projected in the x-y (fig.2) plane is the initial parameter that needs to be specified in order to create a single waverider. Past experience in generating waveriders, gained by Bowcutt and Corda, has shown that there are a number of restrictions that need to be placed on the geometry of each leading edge in order to insure that a valid waverider is constructed. The reasons for some of these constraints are relatively obvious, while others are somewhat subtle.

Original constraints set by Bowcutt, Corda, McLaughlin :

Constraints on the leading edge shapes:

1. The second leading edge point away from the centerline cannot be on the line of symmetry. — If this were to occur, the resulting waverider would have a sharp spike on the upper surface which is undesirable. In addition, two streamlines would lie in the same flow plane. This, too should be avoided because problems will arise in the integration of the waverider volume and surface areas.
2. All leading edge points must lie within the shock wave. — Since the flowfield is not defined outside of the shock wave, the streamlines emanating from these points would have to be traced as freestream streamlines, resulting in extra surfaces.

More importantly, the shock wave would not be attached to the leading edge, which violates the basic waverider premise.

3. The radial distance to each of the leading edge points from the centerline to the shock wave must continually increase. — In some cases, a violation of this occurrence will cause the waverider's upper and lower surfaces to cross over each other. This is obviously an unrealistic result.
4. The polar angle to each of the leading edge points from the centerline to the shock wave must continually increase. — A violation of this occurrence also causes the waverider's upper and lower surfaces to cross each other.

A completely different set of constraints are placed on the entire vehicle geometry for the optimization procedure. For each of these cases, even though a valid leading edge is created, the resulting waverider may exceed other limits imposed by the user. The user imposed limits provide a control mechanism over the optimization procedure. The simplex is never allowed to move beyond these bounds, and therefore some control is gained over which local minimum is found by the optimization procedure. All of the constraints listed below have the option of being made inactive. This is sometimes done since it is occasionally necessary to relax some of the constraints to allow the optimization procedure to continue operating properly.

Constraints on the Vehicle Geometry:

1. Minimum Slenderness Ratio — The user can adjust this constraint to limit the lower bound of the slenderness ratio of the vehicle. Any vehicle that has a slenderness below this minimum is discarded by the optimization procedure.
2. Box Size — The user can set both the upper and lower bounds on the box size of the vehicle. The box size is defined as the semi-span to length ratio of the vehicle. This constraint can be imposed to keep the waverider planform narrow, or it can be relaxed to allow the waverider to have a wide planform. The suggested values

for these parameters are BOXMAX=0.4 and BOXMIN=0.1. These are the values that are used for most of the applications in the present study. Any vehicles outside of these bounds are discarded by the optimization procedure.

3. Volume — The user can also impose limits on the minimum and maximum volume of the waveriders. The minimum limit allows the user to insure that none of the waveriders fall below a given limit. This is useful when optimizing for maximum L/D since no waverider will be considered if it has a volume below this minimum. The maximum limit is useful when relaxing either the slenderness ratio or box size constraints. This keeps the waveriders from getting drastically out of proportion in some of these cases.

New set of constraints defined in the present study :

Constraints on the Vehicle:

1. Minimum radius : When cooling is needed, the value of the minimum radius is set to 10 mm. When cooling is not needed the minimum radius is set to 1 mm. Note that in both cases, the minimum radius needed to avoid low density effects on the heat transfer is also calculated. Therefore, the code will always consider the maximum value of these minimum radius as the final constraint on the radius distribution.
2. Planform shape : In order to avoid unrealistic shapes, the waverider will be rejected if the sweep angle distribution presents a local minimum.
3. Maximum wall temperature : If the maximum temperature is exceeded, when cooling is not pre-required, the waverider will be rejected. If cooling is pre-required and the maximum wall temperature is exceeded, the program will check that the cooling requirement is within the possibility of the active cooling device. If not, the waverider is rejected.

Appendix D References

1. Hypersonic technology for military application. National Academy Press, 1989.
2. Bowcutt, Kevin, "Optimization of Hypersonic Waveriders Derived from Cone Flows — Including Viscous Effects", Dissertation for Ph.D. Degree at the University of Maryland, 1986.
3. Corda, Stephen, "Viscous Optimized Hypersonic Waveriders Designed From Flows Over Cones and Minimum Drag Bodies", Dissertation for Ph.D. Degree at the University of Maryland, 1989.
4. McLaughlin, Thomas, "Viscous Optimized Hypersonic Waveriders for Chemical Equilibrium Flow", Thesis for M.S. Degree at the University of Maryland, 1990.
5. O'Neill, Mary Kae, "Optimized Scramjet Engine Integration on a Waverider Airframe", Dissertation for Ph.D. Degree at the University of Maryland, 1992.
6. Takashima, Naruhisa, "Navier-Stokes Calculations of Optimized Waveriders", Thesis for M.S. Degree at the University of Maryland, 1991.
7. Anderson, John D., Jr., Modern Compressible Flow, New York, McGraw-Hill Book Co., 1990.
8. Anderson, John D., Jr., Hypersonics and High Temperature Gas Dynamics, New York, McGraw-Hill Book Co., 1989.
9. Tannehill, J.C., Mugge, P.H., "Improved Curve Fits for the Thermodynamic Properties of equilibrium Air Suitable for Numerical Computation Using Time-Dependent or Shock-Capturing Methods", NASA CR-2470, Washington, D.C., October 1974.
10. Nelder, J.A., Mead,R., "A Simplex Method for Function Minimization", Computer Journal, Vol. 7, January 1965, pp. 308–313.

11. Poll, D.I.A., "Transition Description and Prediction in Three-Dimensional Flows", Special Course on Stability and Transition of Laminar Flow, AGARD Report 709, March 1984.

12. Poll, D.I.A., "Transition in the Infinite Swept Attachment Line Boundary Layer", The Aeronautical Quarterly, Vol. 30, pp 607–628, November 1979.

13. Poll, D.I.A., "The Development of Intermittent Turbulence on a Swept Attachment Line Including the Effects of Compressibility", The Aeronautical Quarterly, Vol. 34, pp 1 —23, February 1983.

14. Creel, T. R. and al ., "Transition on Swept Leading Edge at Mach 3.5", Journal of Aircraft, Vol. 24, No. 10, pp 710 — 717, October 1987

15. Sheetz, Norman, "Ballistics Range Boundary Layer Transition Measurements on Cones at Hypersonic Speeds", Viscous Drag Reduction, Wells, !968.

16. Malik, Mujeeb, "Prediction and Control of Transition in Supersonic and Hypersonic Boundary Layers", AIAA Journal, Vol. 27, No. 11, November 1989.

17. Tauber, Michael, "A Review of High-Speed, Convective, Heat-Transfer Computation Methods", NASA TP 2914, 1989.

18. Hamilton, Harris, "Approximate Method of Calculating Heating Rates at General Three-Dimensional Stagnation Points During Atmospheric Entry", NASA TM 84850.

19. Press, W. H., Flannery, B.P., Teukolsky, S.A., Vetterling, W.T., "Numerical Recipes", Cambridge University Press, 1990.

20. Glass, D., Camarda, C., "Results of Preliminary Design Studies of Carbon-Carbon/Refractory-Metal Heat-Pipe Wing Leading Edge", NASP TM 1071, 1989

21. Anderson, John D., Jr., Introduction to Flight, New York, McGraw-Hill Book Co., 1990.

22. Zurigat, Y. and al., "Effect of Pressure Gradient on the Stability Limit of Compressible Boundary Layers, AIAA 90–1451.

23. Malik, Mujeeb, Anderson, John D., Jr., University of Maryland, College Park, Maryland, private communication, 1991.

24. Anderson, John D., Jr., Lewis, M., Kothari, A.P., Corda, S., "Hypersonic Waveriders for Planetary Atmospheres", Journal of Spacecraft and Rockets, Vol. 28, No. 4, July-Aug. 1991, pp. 401–410.

REPORT DOCUMENTATION PAGE

Form Approved
OMB No. 0704-0188

1. AGENCY USE ONLY (Leave blank)	2. REPORT DATE	3. REPORT TYPE AND DATES COVERED
	March 1992	Contractor Report

4. TITLE AND SUBTITLE
Heat Transfer Characteristics of Hypersonic Waveriders with an Emphasis on the Leading Edge Effects

5. FUNDING NUMBERS
G NAG1-1192
WU 505-59-40-10

6. AUTHOR(S)
Denis O. Vanmol and John D. Anderson, Jr.

7. PERFORMING ORGANIZATION NAME(S) AND ADDRESS(ES)
University of Maryland
Department of Aerospace Engineering
College Park, Maryland 20742

8. PERFORMING ORGANIZATION REPORT NUMBER
UM-AERO 91-42

9. SPONSORING/MONITORING AGENCY NAME(S) AND ADDRESS(ES)
National Aeronautics and Space Administration
Langley Research Center
Hampton, VA 23665-5225

10. SPONSORING/MONITORING AGENCY REPORT NUMBER
NASA CR-189586

11. SUPPLEMENTARY NOTES The information presented in this report was offered by Denis O. Vanmol as a thesis in partial fulfillment of the requirements for the Degree of Master of Science, University of Maryland, College Park, Maryland, 1991.
Langley Technical Monitor: Lawrence D. Huebner

12a. DISTRIBUTION/AVAILABILITY STATEMENT
Unclassified - Unlimited

Subject Category 02

12b. DISTRIBUTION CODE

13. ABSTRACT (Maximum 200 words)

The heat transfer characteristics in surface radiative equilibrium and the aerodynamic performance of blunted hypersonic waveriders are studied along two constant dynamic pressure trajectories for four different Mach numbers.
In terms of performance, the inviscid leading edge drag was found to be a small (4 to 8 percent) but non-negligible fraction of the inviscid drag of the vehicle. Although the viscous drag at the leading edge can be neglected, the presence of the leading edge will influence the transition pattern of the upper and lower surfaces and therefore affect the viscous drag of the entire vehicle.
Finally, for an application similar to the NASP, the present study demonstrates that the waverider remains a valuable concept at high Mach number if a state-of-the-art active cooling device is used along the leading edge. At low Mach number (≤ 5), the study shows that surface radiative cooling might be sufficient. In all cases, radiative cooling is sufficient for the upper and low surfaces of the vehicle if ceramic composites is used as thermal protection.

14. SUBJECT TERMS		15. NUMBER OF PAGES
hypersonic waverider	surface coding requirements	125
analysis and design	blunted leading edge	16. PRICE CODE
aerodynamic performance	heat transfer	A06
	transition prediction	

17. SECURITY CLASSIFICATION OF REPORT	18. SECURITY CLASSIFICATION OF THIS PAGE	19. SECURITY CLASSIFICATION OF ABSTRACT	20. LIMITATION OF ABSTRACT
Unclassified	Unclassified		